Università degli studi Milano – Bicocca

The Big Blue Bump–Accretion Disk connection in Type 1 Active Galactic Nuclei: a new way to estimate the black hole mass

Dissertation submitted for the degree of:
Philosophiæ Doctor

Presented by:
Giorgio Calderone

Supervisors:
Prof. Monica Colpi
Prof. Gabriele Ghisellini

March 20th, 2013

"The applause for the Big Bang
was heard only fifteen billion years
after the explosion"
J. Gaarder

"La scelta di un disco
è come uno strip–tease dell'anima"
S. Piazzese

"What is mind?
No matter!
What is matter?
Never mind!"
The Simpsons

Abstract

Active Galactic Nuclei (AGN) are among the most powerful sources of energy in the Universe. The "central engine" is likely a super massive ($M \gtrsim 10^6 M_\odot$) black hole accreting matter from the nuclei of host galaxies. In order to study the AGN demography, formation, evolution, accretion physics and galaxy feedback processes we need a reliable method to estimate the black hole mass. The most reliable ones (direct methods) can be applied only to a few tens of nearby AGNs, strongly limiting the possibility to perform statistical studies on large samples and high redshift sources. The issue of black hole mass estimation on large samples of Type 1 AGN is addressed using an indirect (hence less reliable) procedure: the Single Epoch Virial (SEV) method.

In this thesis I discuss the assumptions, biases and possible systematic errors affecting the SEV estimates, and propose a completely independent method to estimate the Type 1 AGN black hole mass. The method is based on the assumption that accretion occur through a standard Shakura & Sunyaev (1973) accretion disk. The calibration is performed by studying the statistical relationships between the broad–band spectral features of Type 1 AGN and the optical emission line luminosities.

I apply the method to a sample of 23 radio–loud narrow–line Seyfert 1 galaxies, for which the SEV masses were suspected to be strongly biased. The resulting black hole mass estimates are significantly greater than SEV ones. I discuss the reliability of these estimates, and the consequence on the physical interpretation of the class of narrow–line Seyfert 1 galaxies in the framework of the AGN unified model.

Contents

Chapter 1

Active Galactic Nuclei

1.1 Introduction

Active Galactic Nuclei (AGNs)[1] are among the most powerful sources of energy in the Universe. The energy output in the form of electromagnetic radiation is being emitted at a rate of $\log(L/\mathrm{erg\ s^{-1}}) \sim 44$–$48$, roughly 10^{11}–10^{14} $L_{\odot}$. Despite the high luminosity, the central regions of AGNs are considerably compact, being unresolved at the milli arcsecond scale even when considering the closest ones. On the other hand some AGNs show giant structures (radio lobes, §1.2.3) with sizes of the order of a few Mpc.

AGNs lie in the nucleus of galaxies of any morphological type, with the most luminous ones being preferentially found in early type galaxies. About 1% of all the observed galaxies host an AGN. For the closest sources it is possible to observe both the AGN and the host galaxy (Fig. 1.5, left and middle panel), while for the farthest ones the AGN radiation outshine the starlight from the host galaxy, and appear as a point–like source (Fig. 1.5, right panel). Due to their high luminosity AGNs can be observed at high redshifts[2] therefore they are useful probes to explore the farthest regions of the Universe.

The spectrum of AGNs extend over several orders of magnitude in frequency, ranging from IR wavelengths to X–rays. About 10% of AGNs are also strong radio emitters and, occasionally, γ–ray emitters. The great majority of AGNs show strong emission lines at optical wavelengths, although there are

[1] A list of commonly used acronyms is given at page 158.

[2] The farthest AGN is currently ULAS J1120+0641, at $z \sim 7.085$ (Mortlock et al., 2011).

cases in which lines are very weak, or even in absorption.

AGNs show significant flux variability at all wavelengths, both in the continuum and the emission line luminosities. The involved timescales range from a few months (at radio wavelengths), to a few days (at optical wavelengths, X–ray). In some cases X–ray variability timescales of the order of one hour has been observed (Aharonian et al., 2007).

1.2 Phenomenology & taxonomy

The AGN classification has been historically based on either optical or radio wavelength properties, and the taxonomy became quite complex as new observational features were discovered. The unification model developed in the '90s (§1.3) allowed for a considerable simplification of the picture, by explaining the different observational features as being fundamentally due to the orientation of the source with respect to the line of sight.

The electromagnetic spectrum emitted from AGNs spans several orders of magnitude in frequency. The continuum in the various bands is usually described in terms of power laws: $F_\nu \propto \nu^{\alpha_\nu}$. The spectral index α_ν is always < 0.5, with typical values ~ -1 from IR to far UV wavelengths. This implies that the emitted energy per decade (or logarithmic frequency interval) is roughly constant over these bands. This also reflects into a roughly constant Spectral Energy Distribution (SED) in a $\log \nu L_\nu$ vs. $\log \nu$ plot (Fig. 1.1, 1.7). The optical/UV continuum of AGN show a significant *ultraviolet excess* with respect to quiescent galaxies. This provides a simple way to identify AGNs in optical/UV surveys.

At (rest frame) optical/UV wavelengths the spectra of the great majority of AGN show several emission lines superposed to the continuum (Fig. 1.2). The lines are classified according to their widths. The (Doppler) broadening is measured in terms of Full Width at Half Maximum (FWHM) of the line. The "narrow line" set, with velocities in the range $\sim 10^2$–10^3 km s^{-1}, is being emitted by ions undergoing both *permitted* (i.e. electric dipole) and *forbidden* energy transitions. The line emitting material is located in the so–called Narrow Line Region (NLR), extending from a few pc, to about 1 kpc from the central engine. The "broad line" set, with velocities in the range $\sim 10^3$–10^4 km s^{-1}, results from permitted transitions only. The luminosities of these lines "reverberates" following the variations in the continuum luminosity

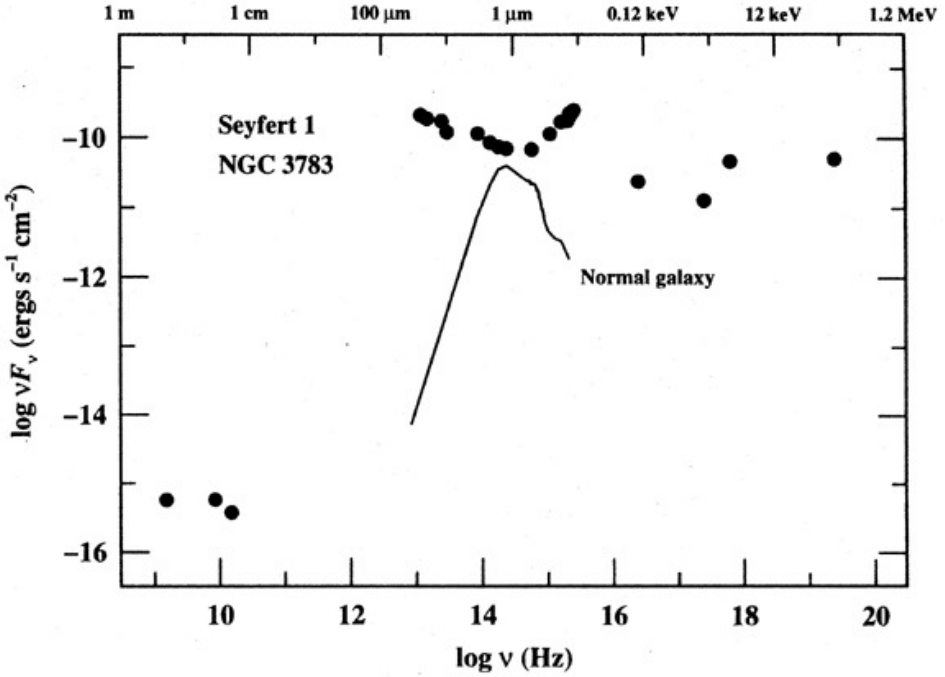

Fig. 1.1: The broad–band SED of NGC 3783 (Alloin et al., 1995) as compared with the template of a quiescent (non–active) galaxy (Elvis et al., 1994).

with time lags of the order of a few days, up to a month (Peterson, 1993). Hence, these lines are emitted in a so–called Broad Line Region (BLR) located a few Light days (1 ld $\sim 2.6 \times 10^{15}$ cm $\sim 10^{-3}$ pc) (ld) from the central engine. The lack of forbidden "broad" lines is due to the higher electron density (with respect to the NLR) which causes metastable energetic levels to be collisionally de–excited (Osterbrock and Ferland, 2006).

1.2.1 Seyfert galaxies

The *Seyfert* galaxies are characterized by high nuclear surface brightness, a point–like core and strong emission lines in optical spectrum. Almost all these sources are hosted in spiral galaxies and their radio emission is typically weak with respect to the emission in optical wavebands, i.e. they are either *radio–undetected* or *radio–quiet* (§1.2.5).

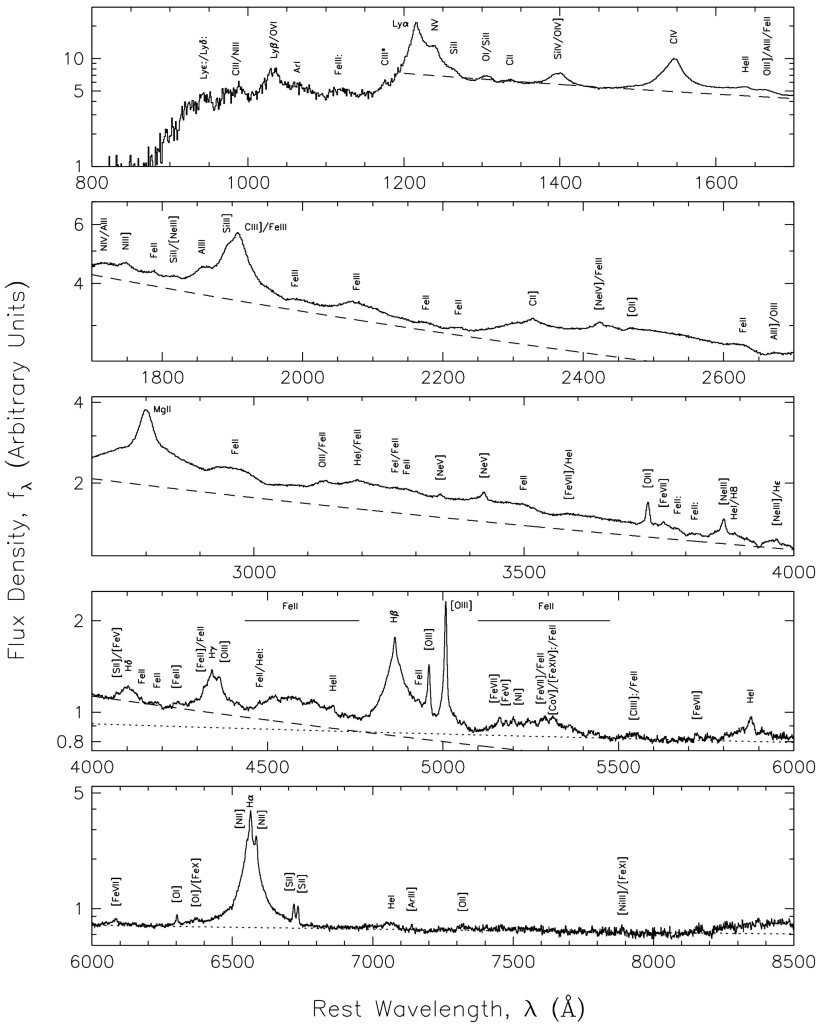

Fig. 1.2: Median composite spectrum of $\sim$ 2200 AGN observed by SDSS in the redshift range $z = 0.044$–4.789 (Vanden Berk et al., 2001). Emission lines are labeled with the corresponding ion. The dashed and dotted lines identify the underlying continuum.

1.2.2 Type 1 vs. Type 2 AGN

The Seyfert galaxies are classified according to the presence of "broad lines" in their optical spectrum (Khachikian and Weedman, 1974). In Seyfert 1 (Sy1) galaxies the emission from both the BLR and the NLR emission are present. Seyfert 2 (Sy2) galaxies, on the other hand, show only the emission from the NLR, while the BLR spectral signature is missing. Fig. 1.3 shows a comparison between the spectra of a Seyfert 1 (bottom, NGC 3516) and a

Seyfert 2 galaxy (top Mrk 1066).

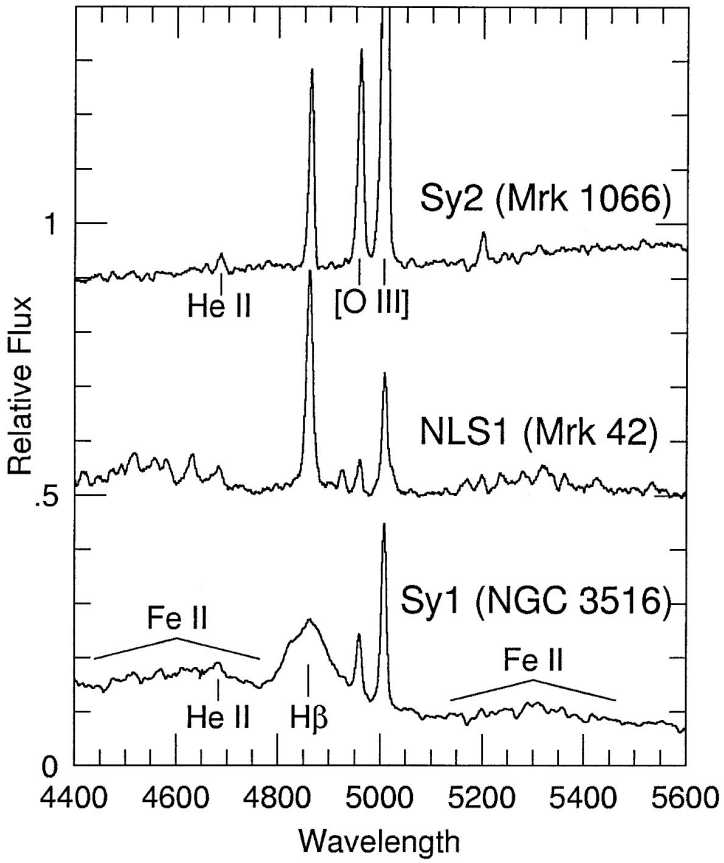

Fig. 1.3: Comparison between the spectra of a Type 1 (bottom, NGC 3516) and a Type 2 AGN (top Mrk 1066). The spectrum in the middle (Mrk 42) belongs to the class of NLS1 sources, to be discussed in Chap. 3. (Pogge, 2000).

A similar classification applies also to the sources discussed in the following paragraphs, hence I will generally refer to *Type 1* and *Type 2* AGN.

1.2.3 Radio galaxies

The AGNs with strong radio emission and extended (i.e. resolved) emission regions are the *radio galaxies*. These sources show similar spectral properties at optical wavelengths as the Seyferts described in §1.2.1, but significantly higher flux at radio wavelengths. The counterparts of Seyfert 1 and Seyfert 2 sources are the Broad Line Radio galaxies (BLRGs) and Narrow Line Radio galaxies (NLRGs) respectively. The radio emission arises in two morphologi-

cally and spatially distinct components: the *compact* region and the *extended* region. The former is unresolved at the milliarcsecond scale and the spectral index is $\alpha_\nu > -0.5$. The latter has a double "lobe"–shaped morphology, and may extends to linear scales of the order of a few $\sim$ Mpc (Fig. 1.4). The spectral index is typically $\alpha_\nu \sim -0.7$. Emission from both the compact and extended region is most likely synchrotron radiation from a population of relativistic particles being ejected from the central engine. Such collimated outflows are called *jets*.

A further morphological classification is based on the distance between the regions of highest surface brightness and the nucleus. By comparing this distance with the total extent of the radio–emitting region, Fanaroff and Riley (1974) defined two subclasses of radio galaxies: sources in which the highest surface brightness regions lie relatively close to the nucleus belong to the first class (FR–I); sources in which the brightest regions lie faraway from the nucleus belong to the second class (FR–II). An example for both classes is shown in Fig. 1.4. Interestingly, this morphological classification corre-

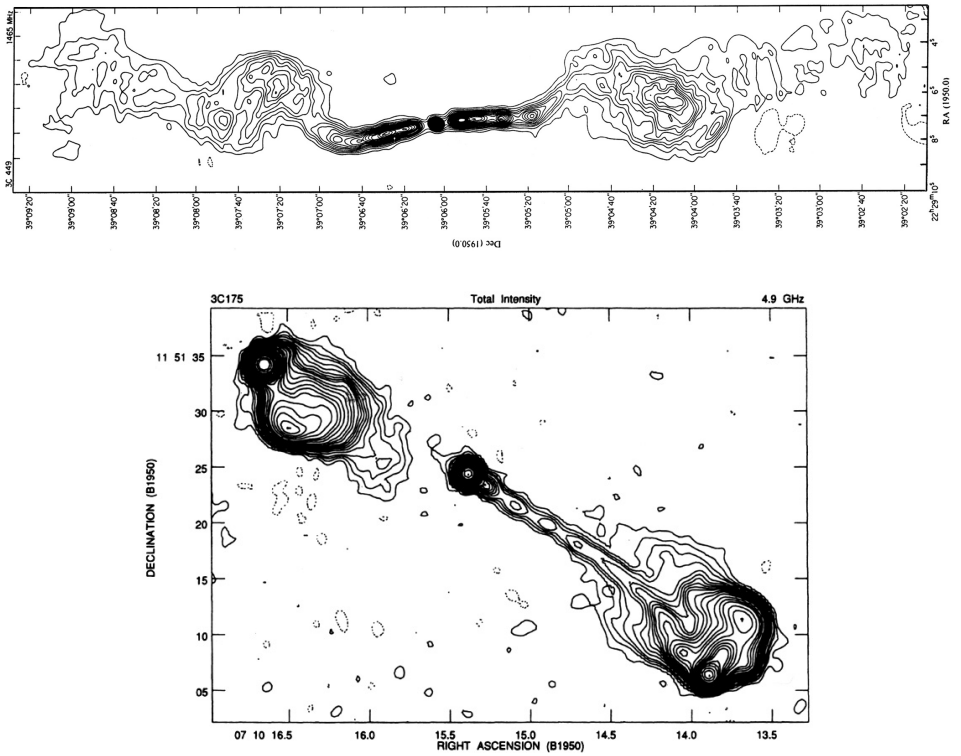

Fig. 1.4: VLA Radio maps of the FR–I source 3C 449 (1.5 GHz, top) and of the FR–II source 3C 175 (4.9 GHz, bottom). Data from NED.

sponds to a separation in total radio luminosity at 178 MHz: FR–I sources are systematically dimmer than FR–II sources. The luminosity threshold is $L_{\mathrm{I-II}}(178\ \mathrm{MHz}) \sim 10^{25}$ W Hz^{-1} sr^{-1}. A similar separation is observed at optical wavelengths (Owen and White, 1991).

In contrast to Seyferts, which are typically found in spiral hosts, radio galaxies are frequently found in giant elliptical galaxies.

1.2.4 QSO and Quasars

Historically, the term AGN was used to denote nearby sources for which the host galaxy could be directly observed, i.e. the Seyferts and the radio galaxies. At greater distances, however, the host galaxy is no longer detectable, either because the AGN itself is significantly brighter than the galaxy, or because its angular extension can not be resolved. These sources show a point–like appearance at optical wavelengths (Fig. 1.5), hence they were called Quasi–stellar object (QSO) or Quasi–stellar radio source (Quasar), depending on their radio luminosity.

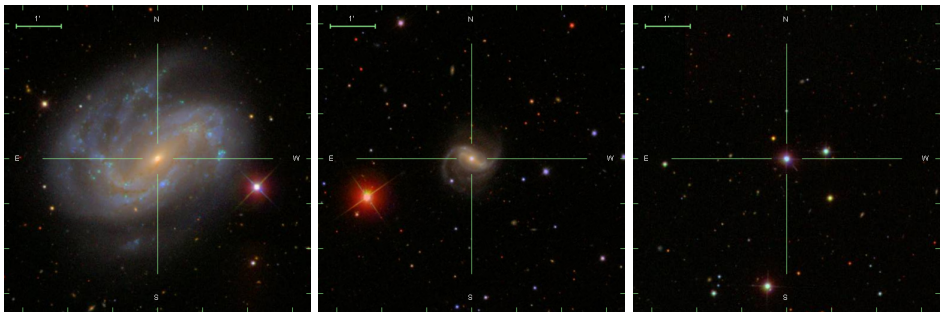

Fig. 1.5: Comparison of apparent size of AGN host galaxies at different redshifts. Left: NGC 4051 ($z = 0.0023$). Middle: Mrk 79 ($z = 0.022$). Right: 3C 273 ($z = 0.16$). All images are from SDSS, the scale is 0.8″/pixel.

The spectral features of both QSOs and Quasars (excluding blazars, §1.2.6) such as emission lines, continuum slopes, variability, etc..., are rather similar to those of nearby AGNs. In particular, the broad band SED of QSOs is quite similar to those of AGNs, once the host galaxy component of the latter is properly taken into account. The SED of both AGN and QSO can be roughly described in terms of three components (Fig. 1.7): the IR bump, between ~ 1 mm and ~ 1 μm or $\log(\nu/\mathrm{Hz}) \sim 11.5$–$14.5$; the Big Blue Bump (BBB), between ~ 1 μm and ~ 3 nm, or $\log(\nu/\mathrm{Hz}) \sim 14.5$–$17$; and the X–ray compo-

nent which consists of a powerlaw with index $\alpha_\nu \sim -1$ in the range 0.1–10 keV, and a bump at $\sim$ 30 keV. This scheme roughly describes the SED of both AGNs and QSOs over at least 5 orders of magnitude in bolometric luminosity (Sanders et al., 1989; Elvis et al., 1994; Richards et al., 2006, , see also Chap. 4). Hence, the widely accepted picture is that both nearby AGNs and distant QSOs and quasars are actually similar sources (§1.4), differing only in overall luminosity and distance. The conventionally adopted threshold to distinguish an AGN from a QSO is expressed using the absolute magnitude in the B band: $M_B = -23$ (Schmidt and Green, 1983). However, the terms AGN, QSO and Quasars are often used interchangeably. In this work I will use the term AGN to encompass all classes of active nuclei.

1.2.5 Radio–loudness of AGN

The greatest majority of AGNs are undetected at radio wavelengths at the milli–Jy level. Among the radio detected ones the relative dominance of radio emission with respect to luminosity in other wavebands is commonly expressed using the Radio–loudness parameter ($R_{\rm loud}$), i.e. the ratio of total observed flux density at 5 GHz (6 cm) to the optical flux density at 4400Å (Kellermann et al., 1989). The $R_{\rm loud}$ parameter (Fig. 1.6) show a bimodal distribution with a separation value of RL $\sim$ 10. The sources with $R_{\rm loud}$ < 10 are classified as Radio–quiet sources (RQs), those with $R_{\rm loud} > 10$ are Radio–loud sources (RLs). The RL sources are $\sim$ 10%–20% of all the AGNs, although this fraction is suspected to be dependent on redshift and absolute luminosity (Jiang et al., 2007).

The AGN emission at radio wavelengths is likely connected to synchrotron emission from matter being emanated from the nucleus in the form of jets. In the most extreme cases the motion is relativistic, and associated effects (such as superluminal motion) are observed when the jet is closely aligned to the line of sight (§1.2.6).

1.2.6 Blazars

An important subclass of RL–AGNs are the *Blazars*. These sources are characterized by fast and strong variability (with timescales $\lesssim$ 1 day), high polarization (up to a few percent), superluminal motion, non–thermal continuum, high radio–loudness ($R_{\rm loud} \gtrsim 100$), and strong γ–ray emission. The emission

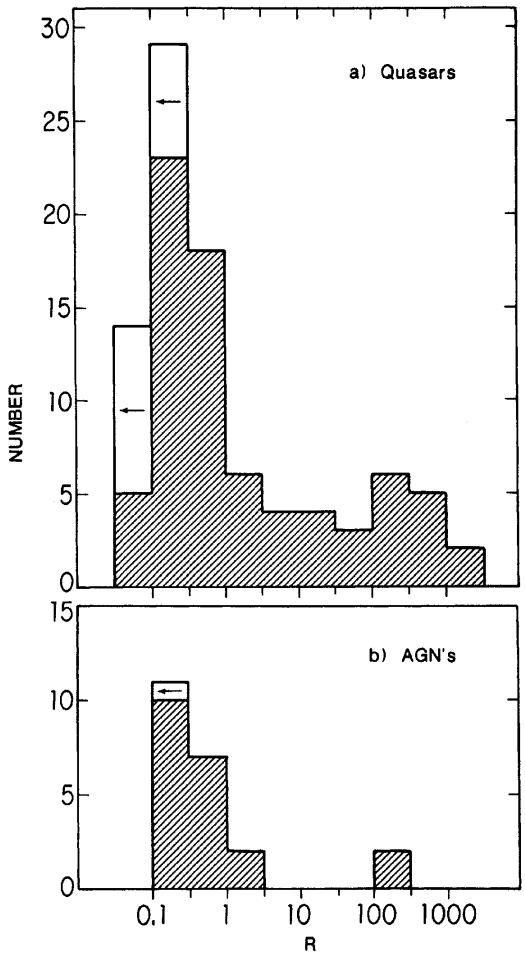

Fig. 1.6: Distribution of $R_{\rm loud}$ parameter (the ratio of total observed flux density at 5 GHz (6 cm) to the optical flux density at 4400Å, Kellermann et al. 1989.)

lines superposed to the continuum can be either strong or almost absent (EW $<$ 5 Å). In the former case the sources are classified as Optically Violent Variable sources (OVVs) at optical wavelengths, and as Flat Spectrum Radio Quasar (FSRQ)at radio wavelengths (the radio spectrum appear "flat" in the νL_ν representation, with $\alpha_\nu \sim 0$). In the latter case the sources are classified as BL Lacertæ–like sources (BL Lacs), after the prototype source of the class.

The broad–band SED of the most powerful blazars (Fig. 1.7) is characterized by the two broad humps, the first occurring between the IR and X–ray waveband, the second occurring at γ–rays. The FSRQ sources typically have a greater luminosity than BL Lac sources. Furthermore, the average SED of

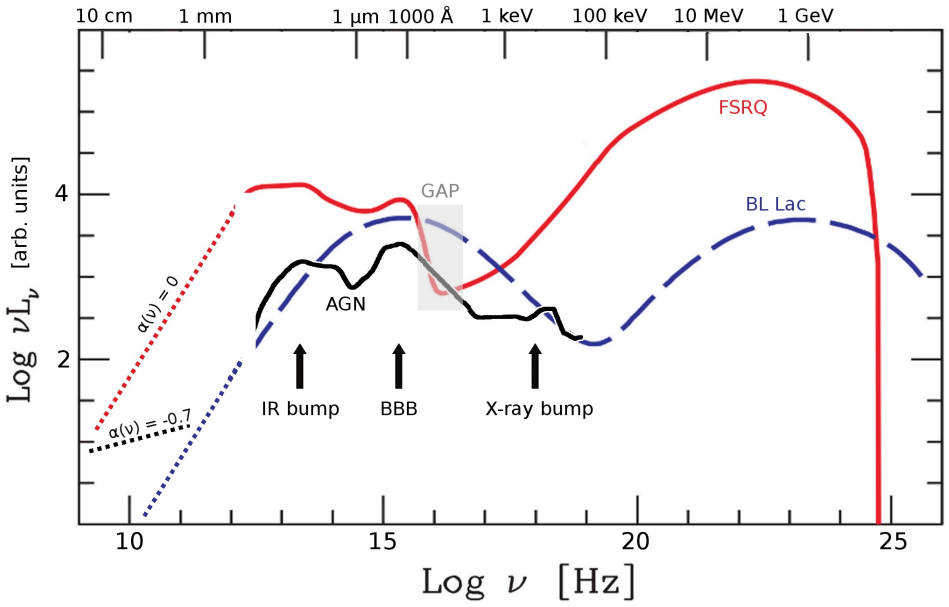

Fig. 1.7: Comparison of average SED of Type 1 AGN (black, Elvis et al. 1994), FSRQ (red) and BL Lac (blue, Ghisellini et al. 2010). The black arrows show the location of the IR bump, BBB and X–ray bump in Type 1 AGN. The two broad humps characterizing the broad–band SED of blazars are clearly visible in the average SEDs. The dotted lines show the typical spectral slopes at radio wavelengths for blazars ($\alpha_\nu \sim 0$) and RL–AGN ($\alpha_\nu \sim -0.7$). The grey area show the frequency range inside which the absorption by neutral hydrogen in our Galaxy hampers our observation capabilities. The purpose of this plot is to compare the shape of the SEDs of non–beamed AGNs and blazars, not their average luminosities.

FSRQ (red line in Fig. §1.7) show a few similarities with the SEDs of both RL and RQ Type 1AGN: namely, the BBB and the IR bump. These feature are not visible in the BL Lac average SED.

The observation of superluminal motion (e.g. in 3C 273, Pearson et al. 1981) with apparent velocities up to $\sim 10\ c$ implies that the relativistic Γ factor for the bulk motion in the most powerful jets are ~ 10. Further relativistic effects are therefore to be expected, especially in those cases in which the jet direction lie close to the line of sight. As an example, the relativistic flux amplification with $\Gamma = 10$ and $\theta \lesssim 10^\circ$ is of the order of $\gtrsim 10^3$. The jet contribution to the overall observed SED would therefore be greatly enhanced, and may overwhelm the emission from an underlying "canonical" AGN.

The peak frequency of the first hump in blazar SEDs is anti–correlated

with its luminosity, hence the SED of blazars are arranged in a sequence which shifts to lower frequencies as the luminosity increases (Fig. 1.8, Donato et al. 2001). Along the sequence the FSRQ sources (with strong optical

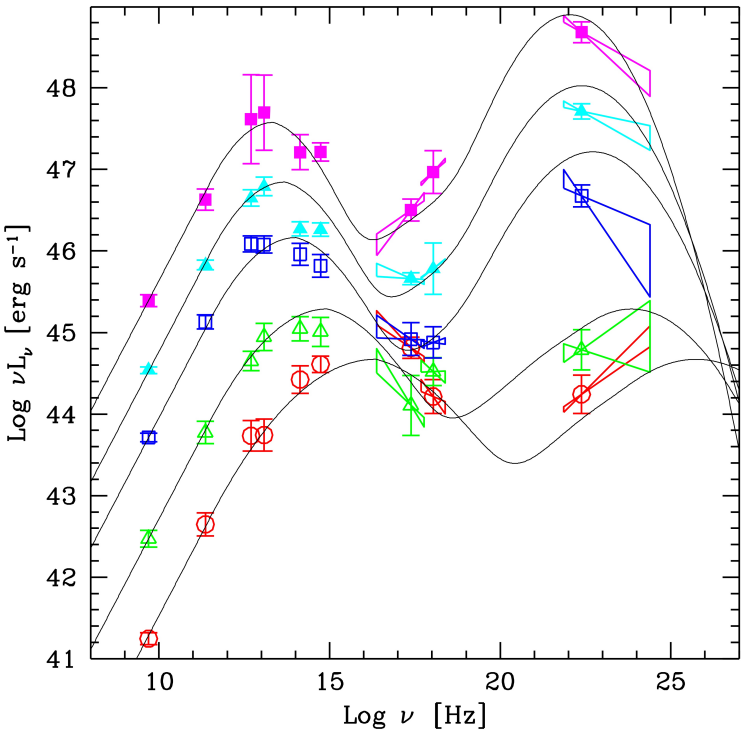

Fig. 1.8: The blazar sequence (Donato et al., 2001).

emission lines) are typically brighter than BL Lac sources (with weak or absent optical emission lines),

1.3 Unification

Several observations show that AGN emission show some degree of anisotropy. The most striking evidence is given by the observation of jets in radio–loud sources, being directed towards opposite direction from the central nucleus (Fig. 1.4) and hence breaking a spherical symmetry. The bulk motion in (at least the most powerful) jets is likely relativistic, hence it is reasonable to expect that the observational properties of a source whose jet direction lies close to the line of sight would be influenced by relativistic effects.

A further evidence for the AGN anisotropy is given by the narrow–band

([O III] λ5007) imaging observations of sharp, triangle shaped, emission regions in several Type 2 AGNs (Fig. 1.9, Pogge 1989; Tadhunter and Tsvetanov 1989). This suggests that the matter surrounding the central engine is being

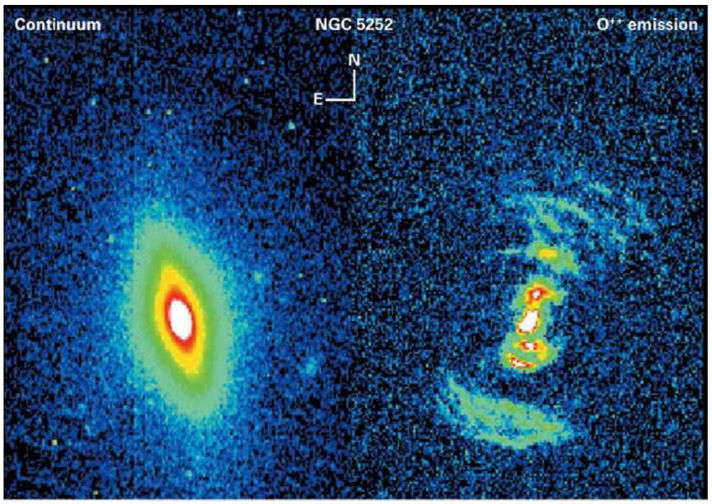

Fig. 1.9: Ionization cones in NGC 5252 (Tadhunter and Tsvetanov, 1989).

ionized only if it lie within a so–called *cone of ionization*, while matter outside the cone is shielded by some intervening medium. The presence of such obscuring medium implies that similar sources viewed at different angles will show different observational properties.

These ideas are at the basis of the unification models, in which the different properties of AGN classes are postulated to be due to orientation effects on otherwise similar sources. Thorough reviews on the unification models are given in Antonucci (1993); Urry and Padovani (1995). The models proceed in a twofold path, by unifying Type 1/Type 2 sources (§1.3.1) and radio galaxies/blazars (§1.3.2).

1.3.1 Type 1/Type 2 unification

The key assumption in the Type 1/Type 2 AGN unification model, is the presence of a toroidal shaped obscuring medium ($N_{\rm H} \gtrsim 10^{21}$ cm^{-2}) surrounding the central engine (the *torus*), and extending from $\sim$ 1 pc (Fig. 1.10, Krolik and Begelman 1988) up to at least a few times 100 pc. The covering factor, i.e. the solid angle subtended by the torus as seen from the central engine normalized by 4π, is of the order of $\sim$ 0.6 (Calderone et al., 2012c). In this

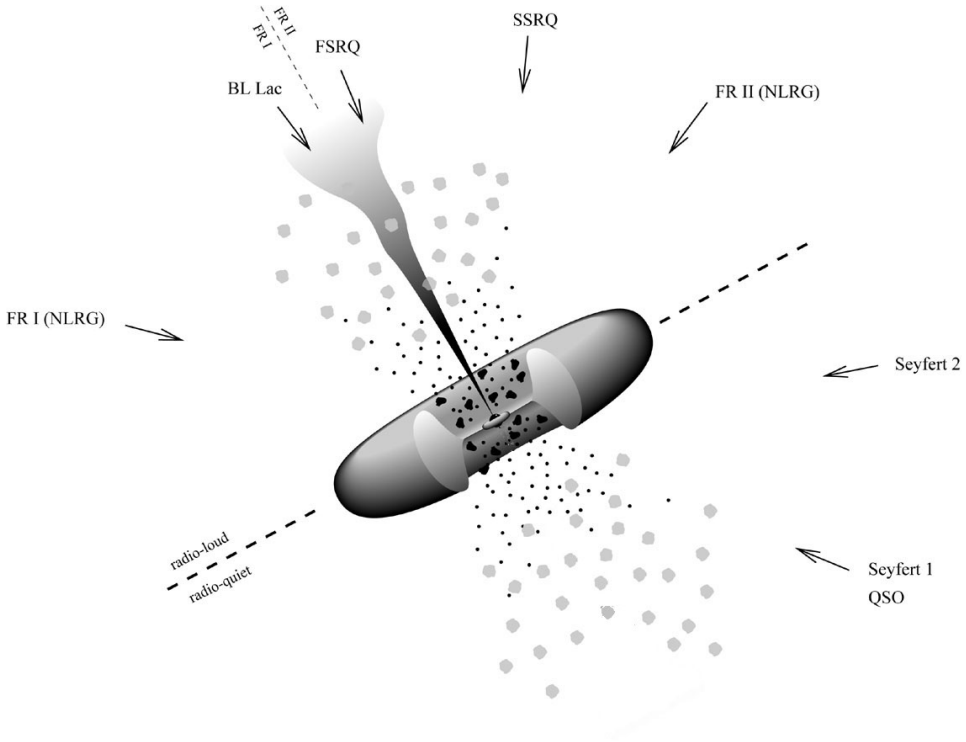

Fig. 1.10: Cartoon of the AGN unification model.

picture, the line–emitting material in the BLR (§2.2) is located at a distance of 10^{16}–10^{17} cm (or $\sim$ 2–30 ld, §2.4) from the central engine, i.e. well within the torus. The NLR is located at significantly greater distances ($\gtrsim$ 1 kpc), and the emission is likely isotropic since self–absorption is negligible due to the very low densities (10^{3}–10^{4} cm^{-3}). Emission from the NLR is thus expected to be detected by any observer, regardless of the viewing angle. On the contrary, emission from the BLR can be observed only if the line of sight does not intercept the torus. This simple scenario depicts both Type 1 and Type 2 AGN as similar sources, but observed at different orientations: if the angle between the torus symmetry axis and the line of sight is sufficiently small ($\alpha \lesssim 40°$) then both the BLR and the central engine can be directly observed and the source will be classified as a Type 1 source. If the angle is greater the source will be classified as a Type 2 source. The same considerations apply both to radio–quiet and radio–loud sources, provided the source is not a blazar (i.e. the jet direction and the line of sight are separated by at least a few degrees).

The Type 1/Type 2 unification model is supported by several observational evidences:

- it simply explains the occurring of the ionization cones (§1.3, Fig. 1.9);
- the free electrons in the NLR of Type 2 sources act as a natural "mirror" by which we can observe the Thomson scattered (and hence polarized) radiation coming from the hidden BLR. Indeed, The spectro–polarimetric observations of (at least some) Type 2 sources show the presence of broad lines (Fig. 1.11, Antonucci and Miller 1985; Miller et al. 1991).

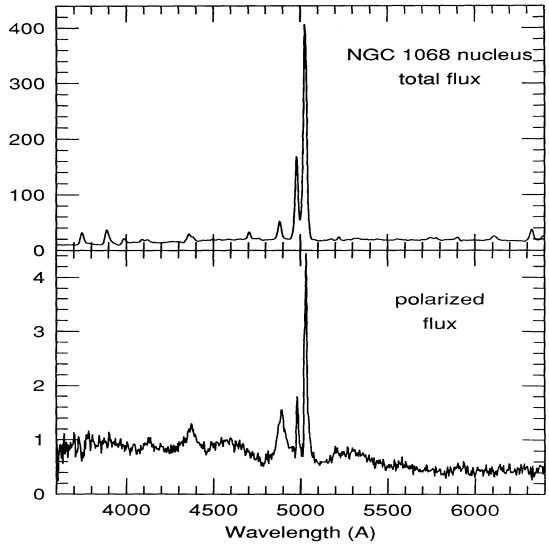

Fig. 1.11: Spectropolarimetric observation of NGC 1068 (Miller et al., 1991).

- a plausible (and efficient) way to absorb all the radiation from the central engine and the BLR is by means of dust. If the torus is dusty and emits thermal radiation it may be observable in broad–band SEDs. The maximum temperature of the dust is the sublimation temperature, i.e. $\sim$ 1500 K. A thermal component with such a temperature is indeed observed in almost all Type 1 AGNs: the so–called *IR bump* (Sanders et al., 1989).
- a similar feature is observed in Type 2 AGN, although with lower temperatures ($\sim$ 500 K). Fig. 1.12 shows the average Type 1 and Type 2 broad–band SED for comparison.

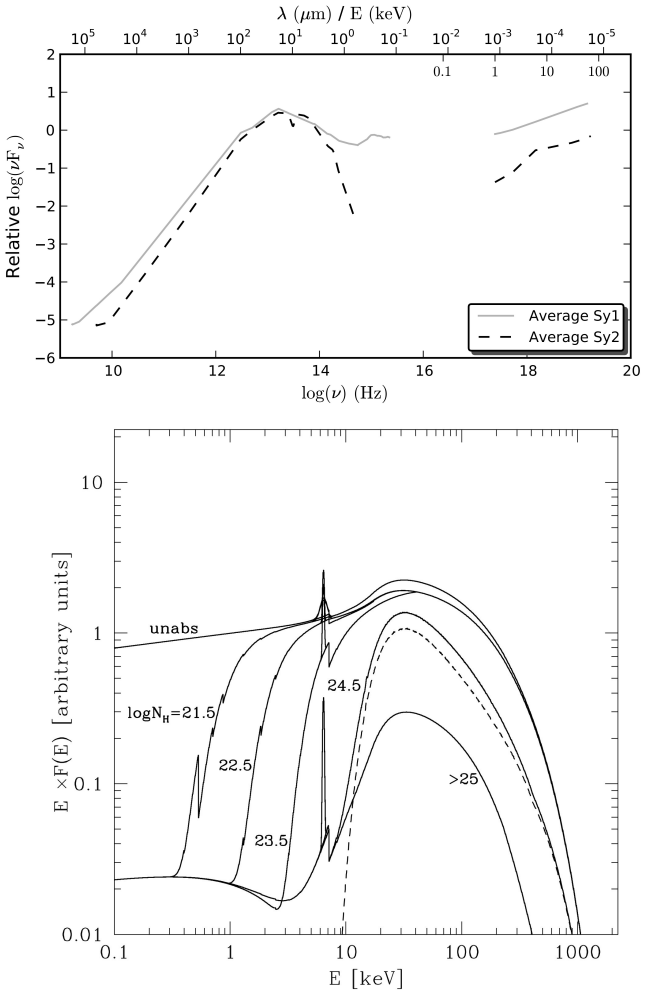

Fig. 1.12: Top: Comparison of Type 1 and Type 2 average opt./IR SED (Prieto, 2012). Bottom: comparison of AGN X–ray spectra for different amount of absorption (Gilli et al., 2007).

- Observations with the Wide Field and Planetary Camera 2 (WFPC2) on board the Hubble Space Telescope (HST) has revealed a toroidal–shaped structure around the nucleus of NGC 4261, with a maximum linear extent of at least $\sim$ 800 ly. (Fig. 1.13)

1.3.2 Radio galaxies/Blazars unification

The radio maps of radio galaxies (e.g. Fig. 1.4) clearly show the presence of outflows (or *jets*) from the nuclei. For the closest AGNs (e.g. in the ra-

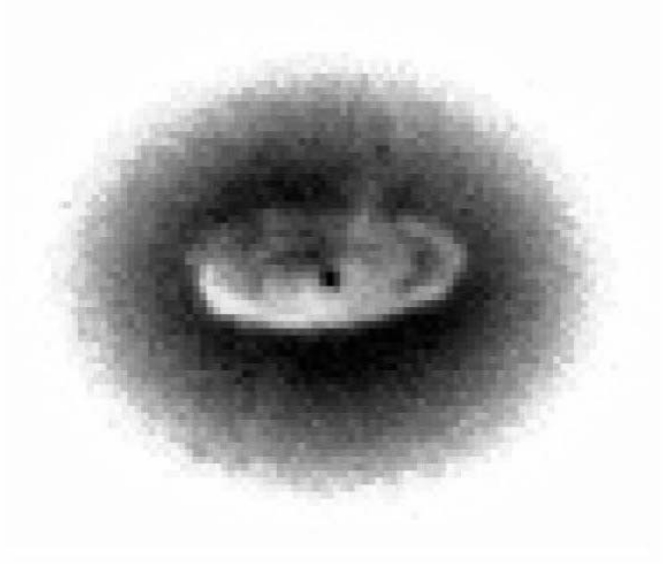

Fig. 1.13: HST/WFPC2 observations of the obscuring torus in NGC 4261. The linear extent of the whole structure is $\sim$ 800 ly (Jaffe et al., 1993).

dio galaxy M 87) the jet can also be observed at optical wavelengths. As discussed in §1.2.6 the relativistic beaming may significantly alter the observational properties of these sources when the jet direction lie close to the line of sight (Blandford and Rees, 1978; Barthel, 1989). Following this idea Urry et al. (1991); Padovani and Urry (1992) have compared the luminosity functions and space densities of both radio galaxies and blazars. By appropriately taking into account the transformation of luminosity functions due to relativistic beaming they have shown that the populations of un–beamed (radio galaxies) and beamed (blazars) sources are compatible. In particular the FR–I sources turns out to be the parent population of BL Lac, while the FR–II sources are the parent population of FSRQ sources. The resulting γ factor are of the order of $\Gamma \sim 10$. A radio–loud source appears beamed if the angle between the line of sight and the jet

1.4 The central engine

The power released as electromagnetic radiation by an AGN can be as large as $\log(L/\mathrm{erg\ s^{-1}}) \sim 48$ (roughly $10^{15}\ L_{\odot}$). The compactness of the active region, and the rapid variability allow to infer that the emission region size must be significantly smaller than 1 pc, i.e. at least five orders of magnitude

smaller than the size of the host galaxy. Hence, the AGN "central engine" must be very efficient in producing huge amount of energy in a very small volume. The process likely responsible for the release of energy is accretion onto a black hole (Hoyle and Fowler, 1963; Salpeter, 1964; Rees, 1984). The efficiency of conversion of accreting mass into radiation (η) is defined as follows:

$$L = \eta \dot{M} c^2 \tag{1.1}$$

The maximum theoretical is expected to be in the range $\eta \sim 0.03$–0.3 (depending on the black hole spin, Thorne 1974). For comparison the efficiency of the pp–chain nuclear reaction is $\eta_{pp} \sim 0.007$.

The AGN electromagnetic radiation carries both energy and momentum away from the central engine. The resulting radiation pressure on surrounding matter contrasts the gravity. By assuming spherically symmetric accretion and considering only the Thomson scattering, the luminosity at which the two forces balance scales linearly with the black hole mass M:

$$L_{\rm Edd} = \frac{4\pi G M m_{\rm p} c}{\sigma_{\rm T}} \sim 1.3 \times 10^{47} \left(\frac{M}{10^9 M_\odot}\right) \text{ erg s}^{-1} \tag{1.2}$$

where $m_{\rm p}$ is the proton mass and $\sigma_{\rm T}$ is the Thomson scattering cross section. This *Eddington limit* is an order of magnitude estimate of the maximum luminosity expected for accretion onto a black hole of a given mass. The *Eddington ratio* ℓ:

$$\ell = \frac{L}{L_{\rm Edd}} \tag{1.3}$$

is thus expected to be $\ell < 1$. Hence, for an AGN luminosity of 10^{44} erg s^{-1}, the corresponding black hole mass must be $M \gtrsim 10^6\ M_\odot$. The black holes powering AGNs are therefore classified as Super Massive Black Hole (SMBH).

The supply of accreting matter is provided by the host galaxy. The gas and stars in the galaxy have a specific angular momentum which is of the order of $l \sim 10^{29}$ cm^2 s^{-1}, while that of a particle in the Innermost Stable Circular Orbit (ISCO) of a $10^9\ M_\odot$ black hole is $l \lesssim 10^{25}$ cm^2 s^{-1}. Hence, in order to accrete onto the black hole the matter must loose almost all its angular momentum, possibly through some kind of viscous process triggered by the increased density as the matter approaches the black hole. If the viscous time scale is longer than the cooling time scale the matter will settle into the lowest energy orbit compatible to a given angular momentum, i.e.

a circular orbit. This results in the formation of a viscous *accretion disk*, a device through which the angular momentum is transported outwards while matter flows inward. Viscosity implies that the disk heats up and converts a sizeable fraction of the accreting rest mass energy into electromagnetic radiation. Accretion disks are believed to be the central engines of AGNs (Pringle, 1981; Rees, 1984).

Considerable efforts have been devoted to the development of accretion disk models (Frank et al., 2002). Among the many models, the most appealing one is the Shakura and Sunyaev (1973) Accretion Disk model (AD) since it allows a direct connection between observational and physical properties. This connection, as well as the possible issues and limitations of the model, will be discussed thoroughly in §6.2.

1.5 Super massive black holes

As discussed in §1.4 a SMBH is required in order to power an AGN. Also, there is compelling evidence that SMBHs are hosted in the nucleus of quiescent galaxies. Observational evidences are given both by studies on individual sources, e.g. the Milky Way (Gillessen et al., 2009; Genzel et al., 2010) and nearby galaxies (Kormendy and Richstone, 1995), and by statistical arguments (the Sołtan argument, Soltan 1982; Merritt and Ferrarese 2001). These black holes may have been "active" in the past, and represent now a population of "dead" quasars (Lynden-Bell, 1969). Possibly, also the Milky Way may have undergone an active phase in the past, as suggested by the recent detection of γ–rays from two "bubble"–shaped regions emanating from the Galaxy center (Su et al., 2010).

The history of the formation of the SMBHs is still unclear. Feeding of material from the host galaxy is possibly the most common supply, although it may not be the only one. By assuming constant values for both the radiative efficiency η and the Eddington ratio ℓ we can estimate the e–folding time for black hole mass increments (the *Salpeter time*):

$$\tau_{\rm S} = \frac{\eta}{(1-\eta)\ell}\, 4.5 \times 10^8 {\rm yr}. \tag{1.4}$$

i.e. the black hole increases its mass by a factor ~ 2.7 over a characteristic timescale of $\sim 10^8$ years. On smaller timescales the mass is not expected

to be significantly greater than that of the *seed*, upon which the black hole has grown. The recent detection of quasars with mass of the order of $M \sim 10^9 M_\odot$ at redshifts $\gtrsim 6$ ($\sim 10^9$ years after the Big Bang, e.g. Mortlock et al. 2011) implies that these black hole have not had time to accrete significantly, and their mass is not significantly greater than the mass of their seeds. This raises the question on how these super massive seeds have formed in such a short time. Possible solutions are accretion with very low radiative efficiency and/or structure merging (see Volonteri 2010 for a review).

The SMBH formation and activity influences the evolution of the host galaxies they live in. Several empirical relationships have been identified among host galaxy properties (such as stellar velocity dispersion in the bulge, bulge luminosity, bulge mass) and the SMBH mass (Kormendy and Richstone, 1995; Ferrarese and Ford, 2005). Despite the very different spatial scales involved, the AGN and the host galaxy affect each other through a *feedback* mechanism likely involving AGN radiation and jets on one side, and fuel supply on the other (Fabian, 2012).

A closely related topic is the evolution of SMBH. The spectroscopic average quantities related to AGNs such as spectral slopes, line equivalent widths, metallicity, etc..., does not show evidence for evolution with redshift (Telfer et al., 2002; Steffen et al., 2006; Juarez et al., 2009; Young et al., 2009; Chaudhary et al., 2010). However, there is now compelling evidence that the AGN population evolve over cosmic epochs. The peaks of the AGN luminosity functions (in luminosity bins) show a clear dependence on redshift: the AGN were more luminous in the past rather than in the local Universe. The peak of the AGN luminosity being at $z \sim$ 2–3 (Hopkins et al., 2007; Croom et al., 2009; Merloni and Heinz, 2012). These studies, coupled with black hole mass estimation methods, allow to explore the evolution of the distribution of super massive black holes.

Finally, SMBH offer a valuable opportunity to explore the geometry of spacetime in the presence of a strong gravitational field. General relativistic effects such as light bending and gravitational redshift influences the radiation on th path from the place of emission to the observer. An important example is the broad, skewed profile of the iron line observed in many AGN (Fabian and Miniutti, 2005).

All the topics discussed in this section are based on estimates of the black hole mass (M), the radiative efficiency (η) and Eddington ratio (ℓ). The

reliability of the estimation method directly affect the reliability of studies on SMBH seeds, AGN formation, evolution and relationships with host galaxy. Therefore it is necessary to consider all the involved biases and uncertainties in black hole mass estimates. Furthermore, it is important to search for new methods, in order cross–check the results and improve their reliability.

1.6 Black hole mass estimation methods

The black hole mass estimation methods for AGNs are strongly dependent on the corresponding ones used for quiescent galaxies, hence I will briefly review both of them. Thorough reviews are given in Kormendy and Richstone (1995); Ferrarese and Ford (2005).

The methods to estimate the SMBH mass in galaxies (both active and quiescent) are classified as either *direct* or *indirect*. The *direct* methods (§1.6.1) rely on direct sampling of observables in the region where the gravitational potential of the SMBH dominates over that of the surrounding stars. An estimate of the linear size of the *sphere of influence* ($R_{\rm h}$) of the SMBH is obtained by requiring the gravitational potential of the black hole to equal that of the surrounding stars. The latter can be constrained by the stellar velocity dispersion σ_*^2 in the bulge, i.e. where the stars dynamic is not dominated by the SMBH gravitational field. The radius of the SMBH sphere of influence is:

$$\begin{aligned} R_{\rm h} \sim \frac{GM}{\sigma_*^2} \quad &\sim 100 \left(\frac{M}{10^9 M_\odot}\right) \left(\frac{200 \text{ km s}^{-1}}{\sigma_*}\right)^2 \text{ pc} \\ &\sim 2 \times 10^6 \left(\frac{200 \text{ km s}^{-1}}{\sigma_*}\right)^2 R_{\rm g} \end{aligned} \tag{1.5}$$

where $R_{\rm g}$ is the gravitational radius of the black hole. Beyond this radius the influence of the gravitational potential of the SMBH quickly vanishes. The angular resolution required to probe the sphere of influence is:

$$\Delta\theta \sim 0.1'' \left(\frac{M}{10^9 M_\odot}\right) \left(\frac{200 \text{ km s}^{-1}}{\sigma_*}\right)^2 \left(\frac{200 \text{ Mpc}}{D}\right) \tag{1.6}$$

Hence, even by using the highest resolution currently available[3] we can

[3] HST: 0.05″ at 6000Å

estimate the SMBH black hole mass with direct methods only for galaxies in the local Universe. For farther galaxies we must resort to the so–called *indirect methods* (§1.6.2).

1.6.1 Direct methods

By an astrometric monitoring of the motion of individual stars within the sphere of influence of a SMBH it is possible to probe its gravitational potential, and estimate its mass. Such an observational campaign has been realized to study the black hole in the center of our own Galaxy (Gillessen et al., 2009). The position of 28 stars has been tracked for ∼16 years. The observed stellar orbits are all compatible with a single point mass of $M = (4.3 \pm 0.4) \times 10^6 M_\odot$, coincident with the position of the Sgr A* radio source (Fig. 1.14, left panel). In particular the star S2[4], at a distance from the black hole at the pericenter of ∼ 125 AU, has completed a full revolution since the beginning of the observational campaign (Fig. 1.14, right panel). Since this method requires resolving the motion of individual stars it

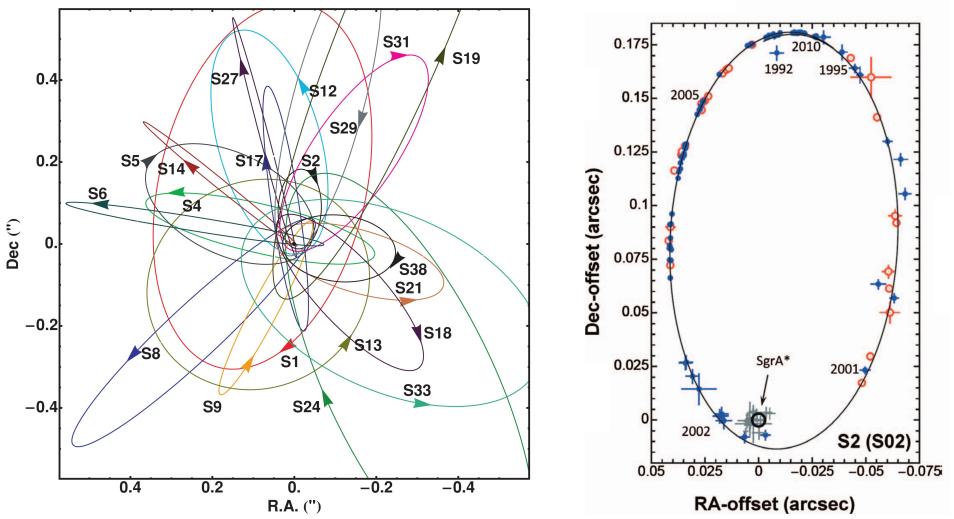

Fig. 1.14: Stellar orbits in the neighborhood (∼ 1 arcsec) of the SMBH in the Milky Way (Gillessen et al., 2009). Right: details of the orbit of the star S2.

currently can be employed only for the SMBH in our own Galaxy.

Another possibility to trace the motion of matter in the gravitational

[4]An animation of the motion of the star S2 around the SMBH in the Milky Way can be found at the site: http://blackholes.stardate.org/research/milky-way-dark-heart.php.

potential of a SMBH is by means of Very Long Baseline Interferometry (VLBI) observations, because of their higher angular resolution with respect to IR/optical. However, the radio emission from stars is negligible at radio wavelengths. The "test particles" in these cases are the clouds emitting H_2O megamaser radiation at a rest frame wavelength of 1.35 cm. In order to produce a powerful enough megamasers the clouds must be arranged in a disk–like geometry observed almost edge–on. These requirements are met for Type 2 nearby AGNs. By means of spatially resolved spectroscopy it is possible to build a rotation curve for the circumnuclear disk. Wherever the rotation curve is Keplerian, i.e. $V \propto R^{-1/2}$, a SMBH mass estimate is obtained. The prototype of megamasing Type 2 AGN is NGC 4258 (Miyoshi et al., 1995). Several more megamasing sources have been discovered, although a Keplerian rotation curve is observed only on a few of them (13/151,[5] see Kuo et al. 2011 and references therein). The involved masses are of the order of $\sim 10^7\ M_\odot$, while the scales probed are in the range 0.1–0.5 pc, i.e. slightly smaller than the typical radii of the sphere of influence. The uncertainties on the SMBH mass are $\lesssim 5\%$.

The most generic methods for SMBH mass estimation galaxies are the *dynamical methods*, based on either stellar or gas kinematics. The tracers are the stellar absorption lines in the former case, the gas emission lines in the latter. In both cases the observables are the average velocity and velocity dispersion of the matter within the sphere of influence of the SMBH. By adopting an appropriate prescription for the mass to light ratio, the gravitational potential of the stars is derived from the surface brightness profile. The SMBH mass is estimated by requiring the sum of gravitational potential due to the SMBH and the stars to be compatible with the kinematic observables. Currently, these methods have been applied on a few tens of sources (Ferrarese and Ford, 2005; Hu, 2008; McConnell et al., 2012). Target galaxies are typically quiescent galaxies since the light from an AGN would easily overwhelm the stellar light within the sphere of influence of the SMBH. There are however a few cases of very nearby AGNs for which a dynamical mass estimate is available (e.g. for NGC 4151, Onken et al. 2007, see also Table 1 in Hu 2008). The dynamical SMBH mass estimates are in the range 10^7–$10^9\ M_\odot$, and the typical errors are in the range 10–50%.

The aforementioned mass estimation methods can be applied only to

[5] https://safe.nrao.edu/wiki/bin/view/Main/MegamaserCosmologyProject

nearby, predominantly quiescent, galaxies. Currently, the only *direct* method to estimate the SMBH mass of a (not necessarily nearby) Type 1 AGN is by means of the Reverberation Mapping (RM) virial method (to be discussed in §2.4). Basically, the sphere of influence is temporally (rather than spatially) resolved through the analysis of the time lags between the light curves of the AGN continuum and the broad emission lines. This provides an estimate of a characteristic size of the BLR. The characteristic velocity of the clouds in the BLR is estimated through the width of the broad emission lines. Finally, the SMBH mass is estimated by assuming a virialized motion of the BLR clouds Eq. 2.1. Although the RM is formally a *direct* method, its calibration is provided by the indirect methods discussed in §1.6.2.

1.6.2 Indirect methods

By comparing the dynamical SMBH mass estimates discussed above with observational properties of the hosting galaxy bulge several empirical correlations have been discovered:

- M–$L_{\rm bulge}$ relation (Kormendy and Richstone, 1995);
- M–$M_{\rm bulge}$ relation (Magorrian et al., 1998);
- M–σ_* relation (Ferrarese and Merritt, 2000; Gebhardt et al., 2000);

The latter has been found to be less scattered than the M–$L_{\rm bulge}$ relation (Fig. 1.15), also it relies on a directly observable parameter (σ_* the stellar velocity dispersion in the bulge of the host galaxy) hence it is preferable to the M–$M_{\rm bulge}$ relation. The M–σ_* relation can be expressed as:

$$\log\left(\frac{M}{M_\odot}\right) = \alpha + \beta \log\left(\frac{\sigma_*}{200\ \mathrm{km\ s^{-1}}}\right) \tag{1.7}$$

where the constants α is of the order of 8. The two groups involved in the discovery of the relation found significantly different values for the β parameter: 4.8 ± 0.5 (Ferrarese and Merritt, 2000) and 3.75 ± 0.3 (Gebhardt et al., 2000). This raised a great debate about the actual values of the β parameter, the discrepancies being possibly due to systematic differences in the adopted values of σ_* (e.g. Tremaine et al. 2002). Considerable attention has been devoted also to the determination of the intrinsic scatter of the M–σ_* relation, i.e. the uncertainty in the resulting value of M once the

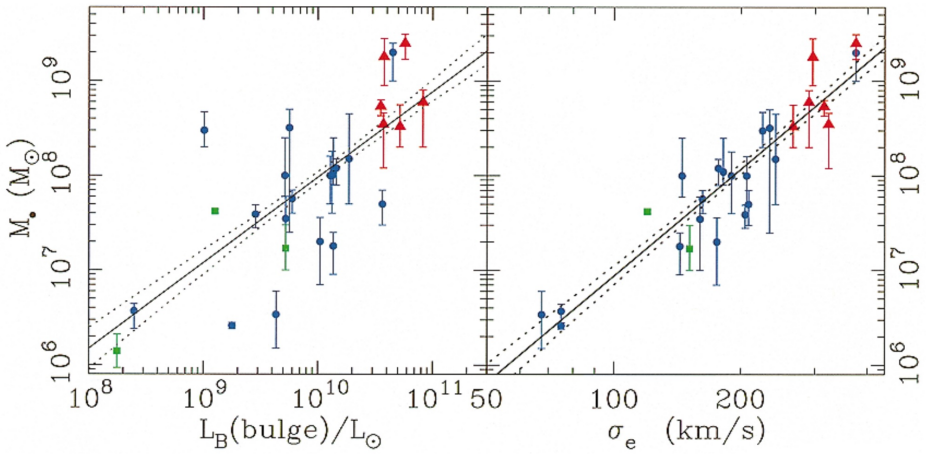

Fig. 1.15: Comparison of the M–$M_{\rm bulge}$ (left) and M–σ_* (right) relations (Gebhardt et al., 2000).

effect of the uncertainties on the parameters α, β and the measure σ_* has been removed. Early estimates for the intrinsic scatter constrained its value to be $\lesssim 0.3$ dex (Tremaine et al. 2002). However, this estimate is strongly influenced by our capability to correctly estimate the statistical uncertainties on both the dynamical SMBH mass and σ_* estimates. The calibration of the M–σ_* relation has been revisited as new and updated dynamical masses became available. Recent calibrations are:

- $\alpha = 8.12 \pm 0.08$, $\beta = 4.24 \pm 0.41$, intrinsic scatter 0.44 ± 0.06 dex, based on a sample of 49 sources (Gültekin et al., 2009);
- $\alpha = 8.13 \pm 0.05$, $\beta = 5.13 \pm 0.34$, intrinsic scatter $0.32\ (+0.06, -0.04)$ dex, based on a sample of 64 sources (Graham et al., 2011);

The total scatter (intrinsic + measurement errors) in both papers cited above is in the range 0.4–0.5 dex, and has increased since the first works on the M–σ_* relation as the analyzed sample increased in size. These calibrations are based on the largest available sample of reliable SMBH mass estimates. However, there is mounting evidence that subsamples selected according to host morphology (e.g. "elliptical only", "barred" or "non–barred") may define tighter M–σ_* relations, with total scatter $\lesssim 0.4$ dex (Hu, 2008; Graham et al., 2011). Furthermore, the relation based on the subsamples of "barred" galaxies appear to lie ~ 0.45 dex below the relations based on "non–barred"

hosts. The offset is comparable with the total scatter, and the two populations appear to follow different M–σ_* relations. This may have consequences on the calibration of the M–σ_* relation (especially on the βparameter) when the whole sample is considered (Graham et al., 2011).

The importance of the aforementioned *scaling relations* is twofold: (i) they shows that the evolution of the SMBH and of the host galaxies are somehow related, despite the ample difference in involved spatial scales (§1.5); (ii) they allow to estimate the SMBH mass by using "proxy" observables ($L_{\rm bulge}$, σ_*). The latter point is a very important one, since it allow to estimate the SMBH without the need to employ the very sophisticated and resolution demanding dynamical methods discussed above. The distance of the galaxy is no longer an issue, since the sphere of influence does not need to be resolved. However, there are still controversies about the calibration of the scaling relations. The accuracy of the SMBH estimate is not expected to be smaller than ~ 0.4 dex (i.e. the total scatter in the observed M–σ_* relation). Also, there are a few examples of dynamically SMBH masses estimates significantly different than predicted by the scaling relations (McConnell et al., 2011; van den Bosch et al., 2012). Finally the sources which build up the M–σ_* relation may just be the upper envelope of a wider distribution comprising galaxies with "small" SMBH mass and/or "large" bulge velocity dispersion. These sources would be missed by dynamical mass studies since their spheres of influence would not be resolved (see Eq. 1.6), hence the angular resolution limit produces a selection effect. On the other hand sources with "large" SMBH mass and "small" bulge velocity dispersion do hardly exists, at least in the local Universe ($\lesssim 200$ Mpc). Hence the M–σ_* relation is likely a *real* upper envelope. Batcheldor (2010) simulated a sample of galaxies with the same values of σ_* and distances as the sources in the M–σ_* relation, but random SMBH masses, and reject: (i) those sources for which the sphere of influence would not be resolved and (ii) those sources which lie significantly above the observed M–σ_* relation. The calibration parameters $\alpha \sim 8$ and $\beta \sim 4$ are recovered. However, as discussed in Gültekin et al. (2011), the probability that the angular resolution selection effect plays a role in determining the M–σ_* relation is rather low, at least for the subsample of early type galaxies.

The scaling relations described above have been discovered and calibrated on samples of quiescent galaxies, since the direct SMBH mass esti-

mation methods can not be applied on AGNs. Also, there are difficulties in estimating the stellar velocity dispersion in AGN, because of the faintness of starlight as compared to the AGN emission. There are however observational evidences suggesting that the bulge properties of (at least the low luminosity) AGNs are similar to the ones in quiescent galaxies (Nelson and Whittle, 1995, 1996). In particular, the broadening of the [O III] λ5007 appear to correlate with the stellar velocity dispersion, although with considerable scatter (Boroson, 2003; Bonning et al., 2005; Greene and Ho, 2005). By assuming that the same M–σ_* relation holds for both quiescent and active galaxies, the [O III] λ5007 width (used as a proxy for σ_*) provides an order of magnitude estimate for the SMBH mass of almost all kinds of AGNs.

Another SMBH mass estimation method suitable for Type 1 AGN is the Single Epoch Virial method (SEV) method, to be discussed in §2.6. It relies on assumption that the same M–σ_* relation holds for both quiescent and active galaxies, and on the scaling relation among luminosity and characteristic size of the BLR (§2.6), discovered by means of RM studies (§2.4). The major advantage of the SEV method is that it requires a single spectroscopic observation in order to be applied (as opposed to the many observations required by RM), hence it can be easily applied on large samples. The SMBH mass estimates span the range 10^6–10^{10}, and the claimed uncertainty is ~ 0.5 dex. However, as discussed in §2.7 there are a number of issues related to the reliability of the SEV method.

1.7 Motivation and outline of this work

The major shortcoming of the aforementioned mass estimation methods is that they operate on different class of sources. Among the *direct* (i.e. reliable) methods the stellar/gas dynamical ones require the sphere of influence to be resolved, hence they can only be applied to a few tens of nearby (predominantly quiescent) galaxies. The megamaser rotation curve and RM virial require either specific geometrical conditions or very long observing campaigns, hence they can be applied to a few tens of (Type 2 and Type 1 respectively) AGNs. Therefore it is not possible to reliably cross check the mass estimates of a single SMBH with different methods. However, as discussed in §1.5, reliable SMBH mass estimates on large samples are crucial for the investigation of important issues such as SMBH formation, evolution

and relationships with host galaxies.

In order to estimate the SMBH mass on large samples we are forced to use the M–σ relation (for quiescent galaxies) and the SEV method (for Type 1 AGNs, §2.6). However, both these methods are based on a number of assumptions, and their reliability is subjected to a number of issues which can be only addressed by comparison with independent mass estimates. In particular, the SEV method may be biased by systematic uncertainties (§2.6), e.g. in the case of mass estimation on the class of NLS1 sources (§3.2).

The aim of this thesis is to discuss the assumptions, biases and possible systematic errors affecting the SEV estimates (Chap. 2), with particular emphasis on the case of NLS1 sources (Chap. 3), and propose a completely independent method to estimate the Type 1 AGN black hole mass. In order to achieve this goal I will review the IR/optical/UV properties of the SED of Type 1 AGNs, and show that it can be interpreted as the superposition of two components, namely the accretion disk and the torus (Chap. 4, 5). The SMBH mass estimation method (Chap. 6) is based on the assumption that accretion occurs through a standard Shakura and Sunyaev (1973) accretion disk model. The calibration is performed by studying the statistical relationships between the broad–band spectral features of Type 1 AGN and the optical emission line luminosities. I apply the method to a sample of 23 radio–loud NLS1 galaxies (Chap. 7), for which the SEV masses are suspected to be biased. The resulting black hole mass estimates are significantly greater than SEV ones. I discuss the reliability of these estimates, and the consequence on the physical interpretation of the class of NLS1 galaxies in the framework of the AGN unified model.

Throughout this work, I assume a ΛCDM cosmology with $H_0 = 71$ km s^{-1} Mpc^{-1}, $\Omega_m = 0.27$, $\Omega_\Lambda = 0.73$.

Chapter 2

Single Epoch Virial mass estimates

2.1 Introduction

The Single Epoch Virial method (SEV) is an indirect method for SMBH mass estimation. Its main advantage is the easy applicability on large samples of spectroscopically observed Type 1 AGNs. The mass estimates, however, are less reliable than those provided with the direct methods discussed in §1.6. The knowledge of the involved biases and uncertainties is important in order to use the SEV estimates as a basis for further research. In this chapter I will discuss in detail the assumptions, applicability, uncertainties and possible biases related to the SEV black hole mass estimates.

The very basic observation on which the SEV method relies is that the broadening of observed BLR emission lines is not caused by thermal motion. Rather, it must be due to a bulk motion of the gas clouds in the vicinity of the black hole (§2.2). Under the assumptions that the motion of the line emitting material is virialized the line width is thus a proxy to the orbital velocity V (§2.3). The characteristic distance R of the emitting material from the black hole is estimated by means of scaling relations between R and either the continuum luminosity or line luminosity (§2.6). Finally, the black hole mass is estimated using the virial relation:

$$M = \frac{V^2 R}{G} \tag{2.1}$$

2.2 The Broad Line Region (BLR)

The SEV method relies on spectroscopic analysis of the broad emission lines, hence I will give a brief description of the current physical interpretation of the BLR (Peterson, 1997; Osterbrock and Ferland, 2006).

The BLR is the physical region inside which the "broad" emission lines (FWHM $>$ 1000 km s^{-1}) are generated. The electron density in this region is sufficiently high ($n_{\rm e} \sim 10^{11}$ cm^{-3}) so that all metastable levels of the ions are collisionally de–excited, and no forbidden lines is generated.

The relative line intensities is similar to those of the H II regions in spiral galaxies, hence the temperature is expected to be of the order of $\sim 10^4$ K. However, line widths are significantly broader, with FWHM values in the range 10^3–10^4 km s^{-1}. A thermal broadening of $\sim$ 5000 km s^{-1} would require a temperature of the order of $\sim 10^9$ K. Hence, the line broadening is a consequence of the bulk motion of the emitting material, and the broad line widths are a proxy to the characteristic velocity V.

The emission of a given line occurs when the emitting gas is in the corresponding *photoionization equilibrium*, i.e. when the amount of ionizing photons is in balance with the rate of recombination. The former is related to the spatial density of ionizing photon at the considered distance. The latter is related to the particle density. The ratio of these quantities is expressed by means of the *ionization parameter*:

$$U = \frac{Q_{\rm ion}}{4\pi R^2 n_{\rm e} c} \qquad Q_{\rm ion} = \int_{h\nu > E_{\rm ion}} \frac{L(\nu)}{h\nu} d\nu \tag{2.2}$$

where $Q_{\rm ion}$ is the number of ionizing photons emitted by the central engine and $n_{\rm e}$ is the electron density. Thus, the condition for line emission translates into a condition for U, whose values depend on the considered ion transition. Emission lines of high ionization (higher $E_{\rm ion}$, lower $Q_{\rm ion}$) are thus expected to be generated closer to the central engine with respect to lines of low ionization (BLR *stratification*).

The line luminosity ratios in AGN spectra are rather similar, despite the differences in bolometric luminosities (Francis et al., 1991; Vanden Berk et al., 2001; Juarez et al., 2009). This suggests that the physical parameters of the BLR (temperature, particle densities, element abundances) are also comparable among different AGNs.

The broad line luminosities show a variability which follows the variations in the underlying continuum emission, i.e. broad lines *reverberate* the continuum variations (Fig. 2.1). By assuming that the observed continuum

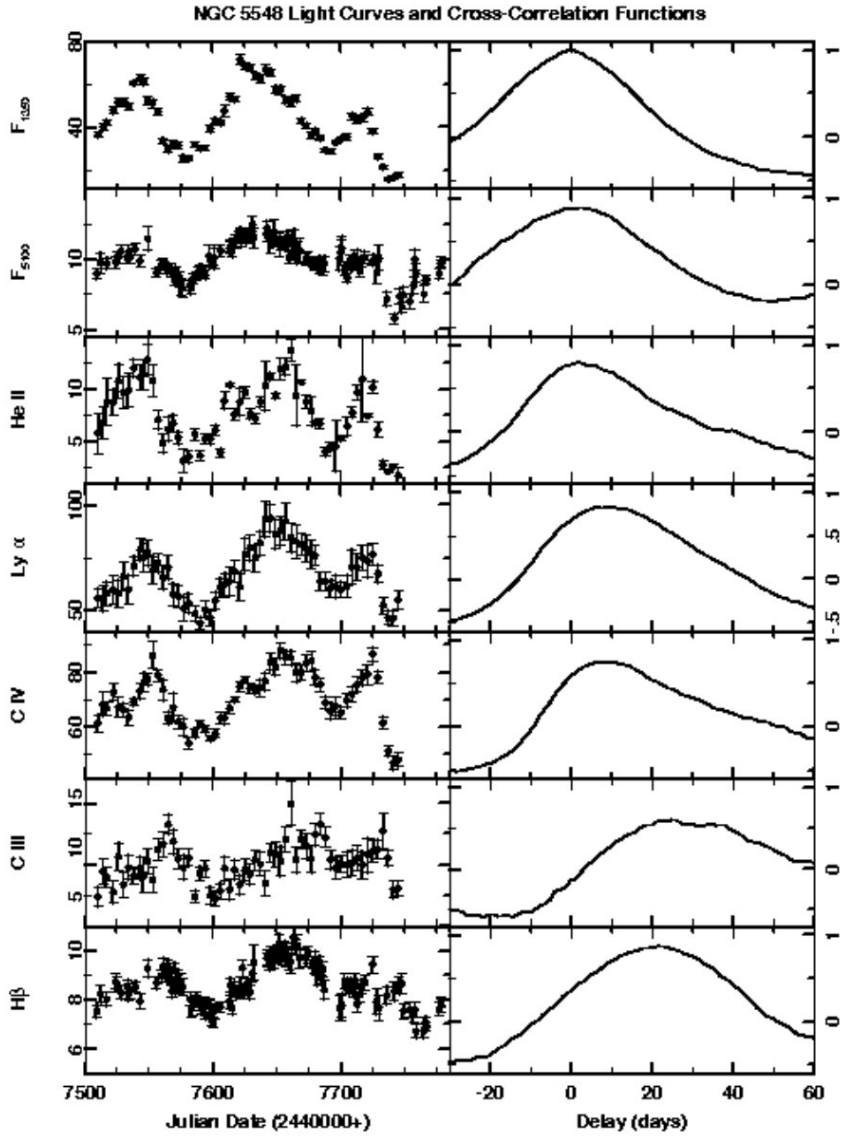

Fig. 2.1: Light curves of continuum and emission lines (left panels) and cross–correlation functions (right panels). Peterson (1997).

is being emitted from the central engine the time lag allow to estimate a characteristic BLR size, which ranges from a few light days to a few tens of light days (10^{16}–10^{17} cm) depending on the considered line. Interestingly, the time lag for high ionization lines are shorter than for low ionization lines,

as predicted by the model discussed above (Peterson, 1993). The very small sizes involved prevents direct observations of the BLR with current technologies. Hence, the kinematics and geometry of the BLR is still unknown.

2.3 Emission line profiles

As discussed in §2.2 the line broadening in the BLR spectrum is likely due to bulk motion of the emitting material. At a characteristic distance of $\sim 10^{17}$ cm (corresponding to $\sim 700\ R_{\rm g}$ from a $10^9\ M_\odot$ black hole) the kinematics of the BLR is likely influenced by the gravitational field of the SMBH. The velocity in a circular Keplerian orbit would be:

$$V_{\rm K} \sim 1.6 \times 10^4 \left(\frac{M}{10^9 M_\odot} \frac{20\ {\rm ld}}{R} \right)^{1/2} {\rm km\ s^{-1}} \tag{2.3}$$

The observed Doppler broadening is related to the velocity component along the line of sight, i.e. multiplied by $\sin(\alpha)$, where α is the angle between the normal to the plane of the orbit and the line of sight. If the BLR has a flattened structure coplanar with the accretion disk then $\alpha < 45°$, since we are dealing with type 1 AGN. Hence, the observed broadening would be smaller than predicted by Eq. 2.3.

To a first approximation the observed line profiles can be approximated by a logarithmic profile: $F_\lambda \propto -\log(\lambda - \lambda_0)$ (for $\lambda \neq \lambda_0$), where λ_0 is the transition rest frame wavelength (Blumenthal and Mathews, 1975). Also, asymmetries in the profiles are often observed, either in the blue or red wing (e.g. Capriotti et al., 1979, 1980; Peterson et al., 1987; Stirpe, 1990; Romano et al., 1996; Véron-Cetty et al., 2001), as well as profile variability (Osterbrock and Phillips, 1977; Peterson, 1987; Stirpe et al., 1988).

In the simplest case the matter in the BLR is in Keplerian orbit around the SMBH, isotropically emitting radiation at a specific transition wavelength. The observed photons are either blueshifted or redshifted according to whether the velocity component along the line of sight is directed toward the observer. The expected line profiles for such a virialized ensemble of BLR clouds can be generated by simulations, as shown in Fig. 2.2. The simulations have been performed by considering 10^5 discrete emitting clouds, each emitting isotropically the same luminosity, orbiting a $10^9\ M_\odot$ black hole. The clouds are assumed to be distributed uniformly in the region lying at a

distance of $20 \pm D_{\rm BLR}$ ld (with $D_{\rm BLR} = 0.5$ ld in the left panels, $D_{\rm BLR} = 5$ ld in the right panels), and at an angle $\pm\theta$ from the equatorial plane (with $\theta = 5^\circ, 15^\circ, 25^\circ, 45^\circ$ in the four rows respectively, the extreme values are $\theta = 0^\circ$: thin–disk shaped BLR; $\theta = 90^\circ$: isotropic BLR). The spectra are observed with a resolution of $\lambda/\Delta\lambda = 2000$ (comparable to the resolution of SDSS DR7), with an angle of sight $\alpha = 10^\circ, 20^\circ, 30^\circ, 40^\circ, 90^\circ$, (the latter would corresponds to an unobscured Type 1 AGN seen edge–on, hence it is shown with a dashed line). All the line profiles have the same integrated luminosity. The resulting line profiles are symmetric in all considered cases, and often show either a double peak profile (when $\theta \lesssim 15^\circ$) or a flat, almost squared profile (when $\theta \gtrsim 15^\circ$). The abscissa values in Fig. 2.2 scale according to Eq. 2.3, hence a measure of the line width would provide an estimate for the quantity $\sqrt{M/R}\sin\alpha$.

However, the observed line profiles (e.g. Fig. 1.2, 1.3) are significantly different from the simulations shown in Fig. 2.2, except possibly in the cases $\alpha \sim 10^\circ$ and $\theta \sim 15^\circ$ (black lines in the second row). Hence the simple model discussed here is not an adequate description of the observed line profile. Several kinematic models have been proposed in order to explain the observed line profiles in the BLR spectra of AGN, including radial inflow or outflow, different geometries and multiple components BLR (e.g. Peterson, 1987; Popović et al., 2004; Romano et al., 1996; Zhu et al., 2009), but no one has yet reached a general consensus. The main concern is the possibility that the width of the line may be due to non–virialized components in the BLR, i.e. that gravity does not dominate the motion of line emitting material. Such a possibility is discussed for the case of B2 0954+25A in §3.4.

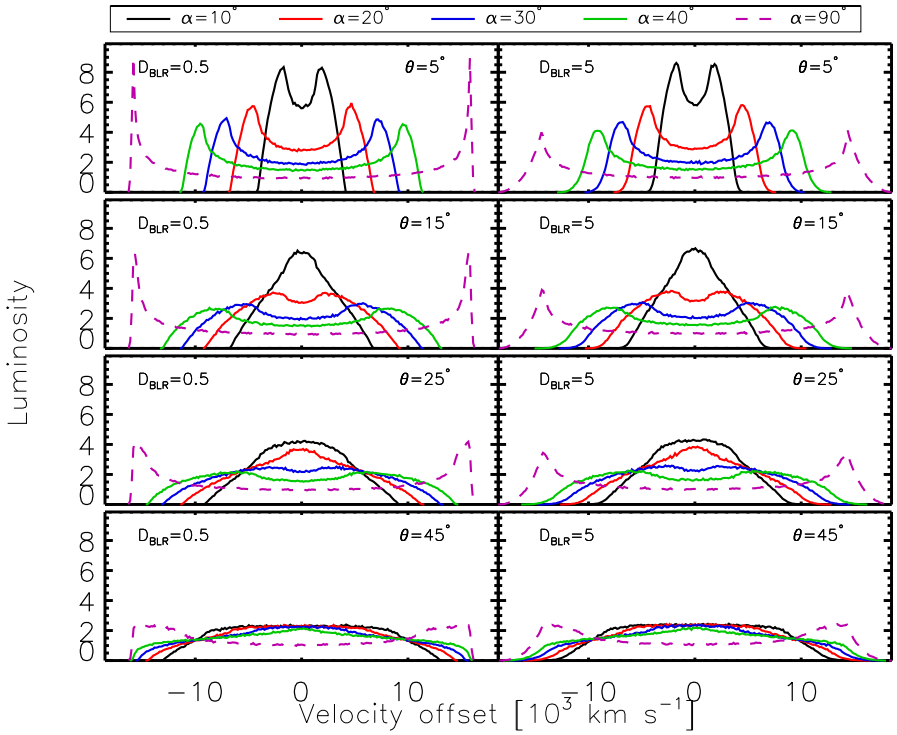

Fig. 2.2: Simulated line profiles from a virialized ensemble of BLR clouds. The simulations have been performed by considering 10^5 discrete emitting clouds, each emitting isotropically the same luminosity, orbiting a $10^9\ M_\odot$ black hole. The clouds are assumed to be distributed uniformly in the region lying at a distance of $20 \pm D_{\rm BLR}$ ld (with $D_{\rm BLR} = 0.5$ ld in the left panels, $D_{\rm BLR} = 5$ ld in the right panels), and at an angle $\pm\theta$ from the equatorial plane (with $\theta = 5°, 15°, 25°, 45°$ in the four rows respectively, the extreme values are $\theta = 0°$: thin–disk shaped BLR; $\theta = 90°$: isotropic BLR). The spectra are observed with a resolution of $\lambda/\Delta\lambda = 2000$ (comparable to the resolution of SDSS DR7), with an angle of sight $\alpha = 10°, 20°, 30°, 40°, 90°$, (the latter would corresponds to an unobscured Type 1 AGN seen edge–on, hence it is shown with a dashed line). All the line profiles have the same integrated luminosity. The resulting line profiles are symmetric in all considered cases, and often show either a double peak profile (when $\theta \lesssim 15°$) or a flat, almost squared profile (when $\theta \gtrsim 15°$). The abscissa values scale according to Eq. 2.3, hence a measure of the line width would provide an estimate for the quantity $\sqrt{M/R}\sin\alpha$.

2.4 Reverberation mapping

As discussed in §2.2 (see also Fig. 2.1) the variability in broad line luminosity lags the variations in the underlying continuum, i.e. the emission lines "reverberate". Hence it is possible to measure the time lags τ in order to esti-

mate the characteristic distance from the central engine to the line emitting material $R_{\rm BLR} = c\tau$ (Blandford and McKee, 1982; Peterson, 1993). Typical distances are of the order of $R_{\rm BLR} \sim$ 2–30 ld, depending on the considered line.

Under the assumption that gravity dominates the motion of the BLR clouds, and with a suitable estimate of the characteristic velocity of the clouds, it is in principle possible to estimate the black hole mass using Eq. 2.1. This provide the basis for the Reverberation Mapping (RM) virial method for the black hole mass estimation. As discussed in §2.3 the lack of a physical model for the BLR to describe the emission line profiles does not allow to link the width of observed emission lines to a characteristic velocity. Hence I will make the further assumption that the observed width W of the emission line is actually related to a characteristic velocity of the line emitting material through a calibration factor ($W \propto V$). The black hole mass is then estimated using:

$$M = f\frac{W^2 R_{\rm BLR}}{G} \tag{2.4}$$

where W is a measure of the width of the line profile (to be defined below), $R_{\rm BLR} = c\tau$ is the characteristic size of the line emitting region, and the f factor accounts for all the details related to the BLR geometry and the eventual de–projection factor ($\sin\alpha$, §2.3).

The RM virial method applied on the same source at different times, and considering different emission lines, is expected to provide consistent values of the black hole mass. Performing this self–consistency test amount to check whether the *virial product* $W^2\tau$ is constant (or equivalently whether $W \propto \tau^{-1/2}$) for different time series and different emission lines. Since the RM observational campaigns are extremely demanding in terms of observing time, this has been done only for a few sources: for the three cases shown in Fig. 2.3 (Peterson and Wandel, 2000) the virial product is compatible with a single value of the black hole mass.

In a RM observing campaign a single source is observed several times in order to collect spectra with different luminosity of the continuum. The light curves of the continuum and of the considered emission lines are then correlated to estimate the characteristic time lag. The spectra are then used to evaluate the line width. This can be accomplished using either the spectrum averaged over all observations or the root mean square (RMS) spectrum

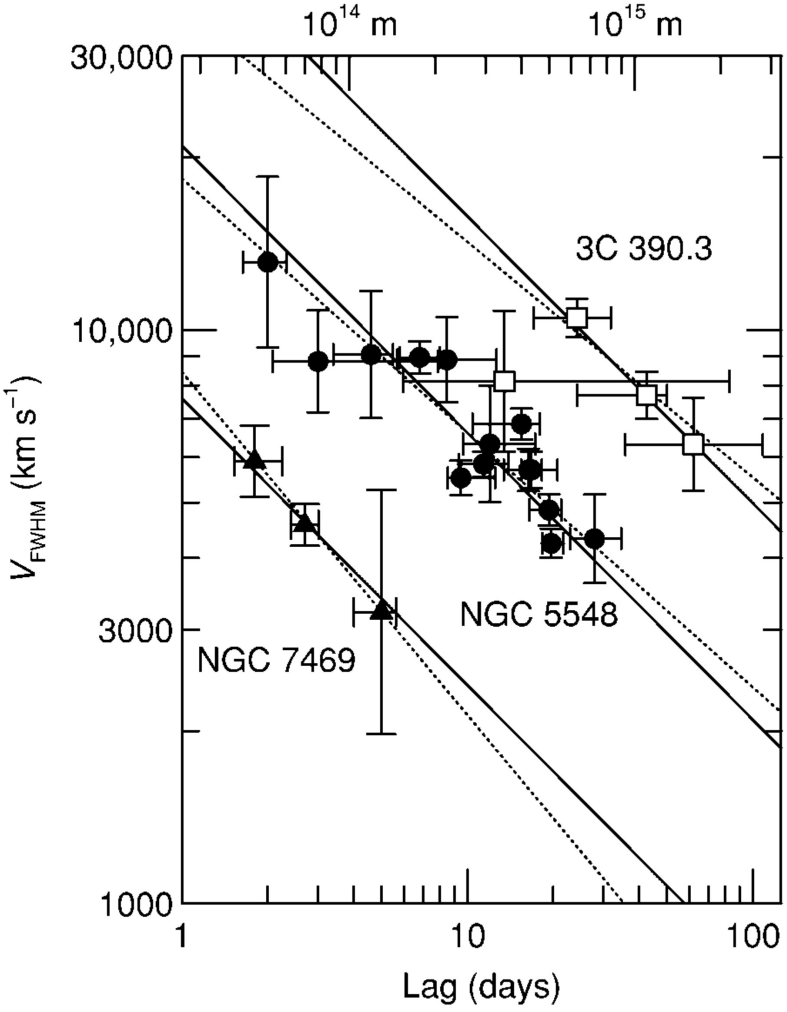

Fig. 2.3: Consistency of virial mass estimates (Peterson and Wandel, 2000).

(Peterson et al., 2004). Use of the latter allow to get rid of all the constant components in the line profile (e.g. narrow emission line components) and estimate the width of the varying components. The drawback is that the RMS spectrum can be significantly noisier than the averaged one. The width of the emission line is usually evaluated using either the FWHM or the square root of the second moment of the profile ($\sigma_{\rm line}$). For a Gaussian shaped line profile the ratio of the former to the latter would be ~ 2.36. As discussed in (Peterson et al., 2004), the highest precision value of the virial product $W^2\tau$ is estimated by evaluating the $\sigma_{\rm line}$ on the RMS spectrum.

The next step toward the black hole mass estimation is the evaluation of the f factor[1] in Eq. 2.4. By estimating the line profile width as the cloud velocity dispersion along the line of sight ($W = \sigma_{\rm line}$) the expected value for the f factor in the two limiting cases of isotropic and disk–shaped BLR is (Netzer, 1990):

$$f = \begin{cases} 3 & \text{(isotropic)} \\ \left[\left(\dfrac{H}{R}\right)^2 + \sin^2\alpha\right]^{-1/2} & \text{(disk–like)} \end{cases} \tag{2.5}$$

where H/R is the characteristic height to radius ratio of the BLR, α is the angle between the normal to the equatorial plane of the BLR and the observer direction. The actual value of the f factor can not be established until the geometry, orientation and kinematic details of the BLR are revealed.

In order to estimate the value of the f factor we require the mass obtained with Eq. 2.4 to be consistent with those of a (hopefully reliable) direct mass estimation method. However, as discussed in §1.6.1 the direct method suitable to estimate the SMBH mass of an AGNs can only be applied to Type 2 sources (megamaser rotation curves), while RM virial method can only be applied to Type 1 AGNs. Another possibility is to assume that AGNs follow the same M–σ relation as quiescent galaxies, and calibrate the f factor accordingly. Support for this hypothesis is provided by early studies which have shown that the SMBH masses estimated with the RM virial method (assuming $f = 3$) are compatible with those from the M–σ relation (Ferrarese et al., 2001; Nelson et al., 2004). By using the RM data analyzed in Peterson et al. (2004), and using the dispersion of the line profile (rather than the FWHM) as a measure of the line width ($W = \sigma_{\rm line}$), Onken et al. (2004) found a value of $f = 5.5 \pm 1.9$ on a sample of 14 sources. By using an enlarged sample of 24 sources Woo et al. (2010) found a value of $f = 5.2 \pm 1.2$. Given the larger size of the sample they also provide an estimate for the slope of the M–σ relation for the active galaxies, $\beta = 3.55 \pm 0.6$ (in rough agreement with the slope reported by Gültekin et al. 2009 for the quiescent galaxies, §1.6.2). The α parameter (normalization) can not be evaluated since it is degenerate with the f factor. The intrinsic scatter of the M–σ is estimated

[1] Notice that in some studies the definition of the f factor is $V = f$ FWHM (e.g. Decarli et al. 2008).

to be 0.43 ± 0.08, this is also a lower limit to the accuracy of the RM virial mass estimates. In contrast to the previous estimates Graham et al. (2011) found $f = 2.8^{+0.7}_{-0.5}$ using sample of 64 sources. By adopting this value all RM virial masses would be approximately halved. As discussed in Park et al. (2012), the differences in the f factor estimates are likely due to the different samples being analyzed. The adopted regression analysis may also influence the final results. Moreover the M–σ relation may not be universal, hence the quest for an average value of the f factor may be an ill–posed problem. To this regard it is worth to notice that reliable σ_* estimates can be obtained only for relatively nearby AGNs, hence the whole picture may suffer from selection effects in the choice of the calibration sample. Finally, the f factor is not expected to be a universal constant, rather it will likely depend on the considered source. In particular, if the BLR is not spherically symmetric, it will depend on the angle of sight (Eq. 2.5).

2.5 Radius–Luminosity (R–L) relations

Analysis of RM data have shown the existence of a correlation among the characteristic size of the BLR and the observed continuum luminosity (Kaspi et al. 2000, Fig. 2.4). This R–L (or *Kaspi*) relation is usually expressed as:

$$\frac{R_{\rm BLR}}{10 \text{ ld}} = A \left(\frac{\lambda L_\lambda}{10^{44} \text{ erg s}^{-1}} \right)^B \tag{2.6}$$

where $R_{\rm BLR}$ characterize the radius at which a specific broad emission line is preferentially generated, and the wavelength λ is typically taken to be close to the considered emission line center wavelength. By assuming constant values for the electron density $n_{\rm e}$, ionization parameter U and the $Q_{\rm ion}$ to λL_λ ratio, Eq. 2.2 provides a straightforward physical interpretation for this relation: a given line is efficiently generated wherever the flux density of ionizing photons is in balance with the density of electrons, i.e. $R_{\rm BLR} \propto (\lambda L_\lambda)^{-0.5}$.

Early estimates (based on the characteristic emitting radius of the $H\beta$ broad line and the continuum luminosity at 5100Å) are $A \sim 2$ and $B \sim 0.7$ (Kaspi et al., 2000, 2005), roughly in agreement with the prediction. Recent estimates based on enlarged and updated RM databases adopted a distinctly shallower slope of B after the contribution of the host galaxy starlight has

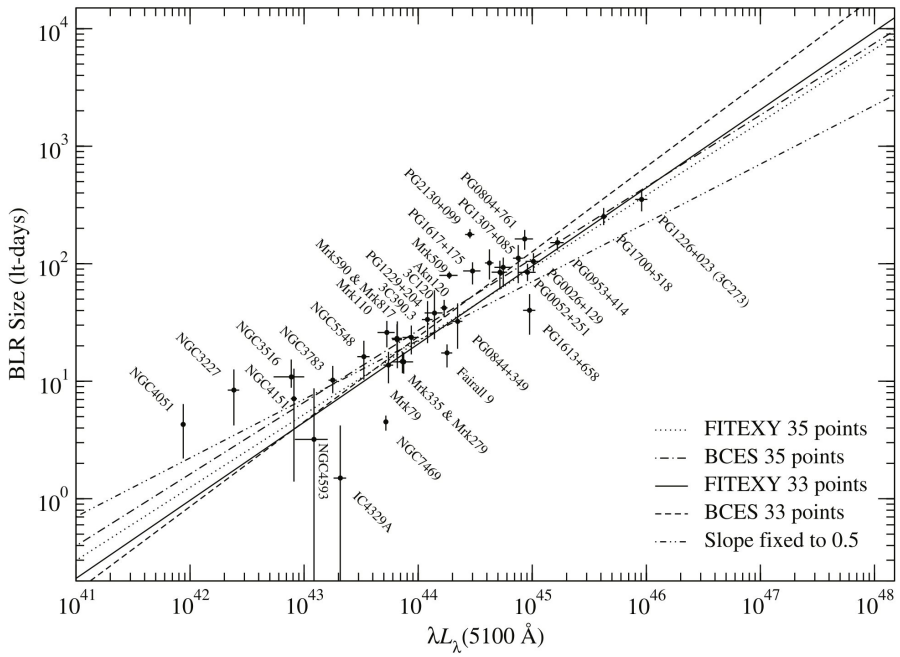

Fig. 2.4: R–L (or *Kaspi*) relation (Kaspi et al., 2005).

been properly taken into account: $A = 3.44$, $B = 0.519$ (Bentz et al., 2009). The intrinsic scatter of the R–L relation is claimed to be of the order $\sim$0.11 dex (Peterson, 2010), i.e. comparable to the uncertainties in RM–based BLR size estimates.

2.6 Single Epoch Virial method (SEV)

Under the assumption that the BLR clouds kinematics is dominated by the gravitational field of the SMBH the velocity dispersion and the size of the line emitting region are directly related to the SMBH mass. The former can be estimated with the broadening of the line profile W. The characteristic size of the line emitting region can be estimated using the continuum luminosity and the R–L relation described in §2.5. Both these estimates require a single spectroscopic observation. By means of RM studies it is possible to calibrate an average virial f factor (§2.4). Finally, through Eq. 2.4 it is possible to estimate the SMBH mass. This is the Single Epoch Virial method (SEV) for SMBH mass estimation.

The SEV method is usually parametrized using the FWHM of the observed

line profile and the continuum luminosity at a given wavelength (λ):

$$\log \frac{M}{M_\odot} = A + 2\log\left(\frac{\mathrm{FWHM}}{\mathrm{km\ s^{-1}}}\right) + B\log\left(\frac{\lambda L_\lambda}{10^{44}\ \mathrm{erg\ s^{-1}}}\right) \tag{2.7}$$

where the calibration constants A and B depends on the considered emission line. Recent calibrations of the SEV method are:

- Hβ, $\lambda = 5100$Å: A=0.67, B=0.61 (McLure and Dunlop, 2004);
- Hβ, $\lambda = 5100$Å: A=0.91, B=0.5 (Vestergaard and Peterson, 2006);
- Mg II, $\lambda = 3000$Å: A=0.51, B=0.62 (McLure and Dunlop, 2004);
- Mg II, $\lambda = 3000$Å: A=0.86, B=0.5 (Vestergaard and Osmer, 2009);
- Mg II, $\lambda = 3000$Å: A=0.74, B=0.62 (Shen et al., 2011);
- C IV, $\lambda = 1350$Å: A=0.66, B=0.53 (Vestergaard and Peterson, 2006).

The uncertainty of the SEV method is estimated to be of the order of ~ 0.5 dex, as a consequence of the scatter in the M–σ and the R–L relations relation (§2.4, §2.5, Peterson 2011). Note however that there may be systematic uncertainties not accounted for in this analysis (§2.7).

The great advantage in using the SEV method rely on its easy applicability on large samples, since it only requires a single optical spectroscopic observation to estimate the observables (FWHM and λL_λ) and a calibrated formula to estimate the SMBH mass (Eq. 2.7).

2.7 Issues related to the SEV method

The SEV method discussed here provides a very simple way to estimate the SMBH mass of a Type 1 AGN. It is important to summarize the several underlying assumptions, in order to evaluate the actual reliability of the method. Also, I will briefly discuss the (possibly involved) biases, and the corresponding systematic uncertainties.

1. the method relies on the assumption that the BLR clouds are in Keplerian orbital motion around the SMBH, i.e. that the dynamic is dominated by the SMBH gravitation field. Support for this hypothesis is provided by the constancy of the virial product (Fig. 2.3, Peterson and

Wandel 2000). However, the number of sources for which this check has been performed is very small(Peterson and Wandel, 2000; Peterson et al., 2004). Moreover, the same kinematical fingerprint can be impressed by other (non–virial) dynamical models (Krolik, 2001);

2. the calibration of the SEV method relies on the M–σ relation for quiescent galaxies (§1.6.2), and on the R–L relation derived from RM studies (§2.5). Both these empirical relation have been established using samples of nearby AGNs ($z \lesssim 0.3$). By using the SEV method for sources at higher distances we are implicitly assuming that the same relations hold for those AGNs. Moreover, there are hints that the calibration of the M–σ relation may depend on the host galaxy morphology. (Graham et al., 2011);

3. the virial f factor depend on the unknown BLR geometry and inclination of the BLR with respect to the line of sight. Currently it is not possible to estimate the f factor for each source, therefore we must resort to an "averaged" calibrated value. However, there is no reason to assume that a single value will provide reliable estimates for all sources. In particular, for significantly flattened BLR the f factor show a strong dependence on the angle of sight (for almost pole–on views, §2.5).

4. the radiation pressure experienced by the electrons in the BLR may play a role in determining the kinematic properties of the BLR clouds (Marconi et al., 2008). In this case the SEV mass as computed by Eq. 2.7 would be underestimated. By assuming that the bolometric luminosity is proportional to the luminosity at the wavelength λ the correct expression for the mass is:

$$\log \frac{M - RP}{M_\odot} = A + 2 \log \left(\frac{\mathrm{FWHM}}{\mathrm{km\ s^{-1}}} \right) + B \log \left(\frac{\lambda L_\lambda}{10^{44}\ \mathrm{erg\ s^{-1}}} \right) \qquad RP = 10^C \times \left(\frac{\lambda L_\lambda}{10^{44}\ \mathrm{erg\ s^{-1}}} \right) \tag{2.8}$$

where the RP term accounts for the radiation pressure effect. A recent calibration is: $A = 0.6$, $B = 0.5$, $C = 7.5$ (Chiaberge and Marconi, 2011). As discussed in Marconi et al. (2008) the use of Eq. 2.8 reduces the scatter between the RM–based mass estimates and the SEV–based

ones. However, it is not clear whether this effect is a due to a more realistic model or to the addition of a further degree of freedom.

5. as discussed in §2.3, the lack of a physical model to describe the broad emission line profile prevents us from reliably associate orbital velocities to observed line widths. Moreover, broad line profile sometimes show asymmetries and both blue and red shifts which may affect the line width estimate. Finally, the width estimates may depend on the analysis procedure being used. In particular the broad/narrow decomposition is not unique, as it depends on the assumed line profile. This may introduce significant uncertainties especially when the broad and narrow component have comparable widths (Fig. 7.1).

6. the line width estimates used in the calibration of the RM method are usually based on the velocity dispersion of the line profile ($\sigma_{\rm line}$) as measured on the RMS spectrum(Peterson et al., 2004). In the SEV method the line width estimate is provided by the FWHM of the profile as measured on a single spectrum (containing both constant and variable spectral components).

7. the uncertainty of the SEV method ($\sim$0.5 dex) does not take into account the errors associated to the FWHM and λL_λ estimates. In order to be negligible the uncertainty in the former should be $\ll 0.25$ dex. The uncertainty in the latter is never an issue.

8. the λL_λ term in both Eq. 2.7 and 2.8 is the continuum luminosity at wavelength λ. However, an estimate of this quantity is likely contaminated by the host galaxy starlight, especially when $\lambda < 3000$Å. In the case of RL sources, a further contamination may be due to the synchrotron radiation from the jet (§1.2.6). These contributions are taken into account when calibrating the SEV method by choosing RQ sources and by subtracting the host galaxy contribution.

The aforementioned issues may introduce additional uncertainties (beyond the nominal 0.5 dex uncertainty) or systematic biases, and may become crucial for specific AGN classes (e.g. §3.2). Further discussion on possible uncertainties and systematics are given in Peterson (2011); Vestergaard et al. (2011). These issues should receive careful attention when the SEV masses are used as a base to infer additional results.

2.7.1 Analysis of SEV results on large samples

The SEV method can be easily applied on large samples of spectroscopic observations. Here we will consider the results on the Shen et al. (2011) catalog (S11). This catalog reports the analysis of SDSS spectra on a sample of 105,783 AGNs (Schneider et al., 2010). The sources have been selected among the SDSS observed ones having $M_{i'} < -22$ ($\nu L_\nu(5100\text{Å}) \sim 10^{44}$erg s^{-1}) and at least one broad emission line with FWHM > 1000 km s^{-1}. The catalog reports estimates of broad line widths and luminosities (for Hα, Hβ, Mg II and C IV), continuum luminosities (at 1350Å, 3000Å and 5100Å), as well as many other spectral properties. Furthermore it reports the SEV SMBH mass estimates using the (Hβ, 5100Å, Vestergaard and Peterson 2006), (Mg II, 3000Å, Shen et al. 2011) and (C IV, 1350Å, Vestergaard and Peterson 2006) calibrations. Fig. 2.5 shows the distributions of line widths (FWHM) and continuum luminosities (λL_λ) for the three considered combinations (left panels), and the corresponding distributions of SEV SMBH mass estimates (right panels). The purple histogram shows the mass distribution computed according to the Chiaberge and Marconi (2011) calibration (Eq. 2.8). Also shown on the right panels are the Gaussian distributions with the same mean as the SEV distributions, and a standard deviation of 0.5 dex (dashed lines). Fig. 2.6 shows the redshift distribution of the sources in the S11 sample (colors identify the subsamples used in Fig. 2.5.) In the following I will always consider the logarithmic values of the FWHM, λL_λ and M values.

According to the assumptions of the SEV method, the line width accounts for the characteristic orbital velocity of the clouds, while the continuum luminosity accounts for their characteristic distance from the SMBH. These quantities are related to the fundamental physical properties of the system, namely the AGN luminosity[2] L (2.2, §2.5) and the SMBH mass M (Eq. 2.7). Apparently, there is no correlation between the line widths and the continuum luminosities, hence the system has two degrees of freedom.

The standard deviations of the FWHM distributions are $\sigma_{\rm FWHM} = 0.23$, 0.18 and 0.21 dex (for Hβ, Mg II and C IV respectively), while those of λL_λ distributions are $\sigma_{\lambda L_\lambda} = 0.37$, 0.51, and 0.38 dex (at 5100Å, 3000Å and 1350Å respectively). These are the only observational quantities entering

[2]It is common practice to assume a relation $L \propto \lambda L_\lambda$, with a different calibration for each considered value of λ (§4.3.1).

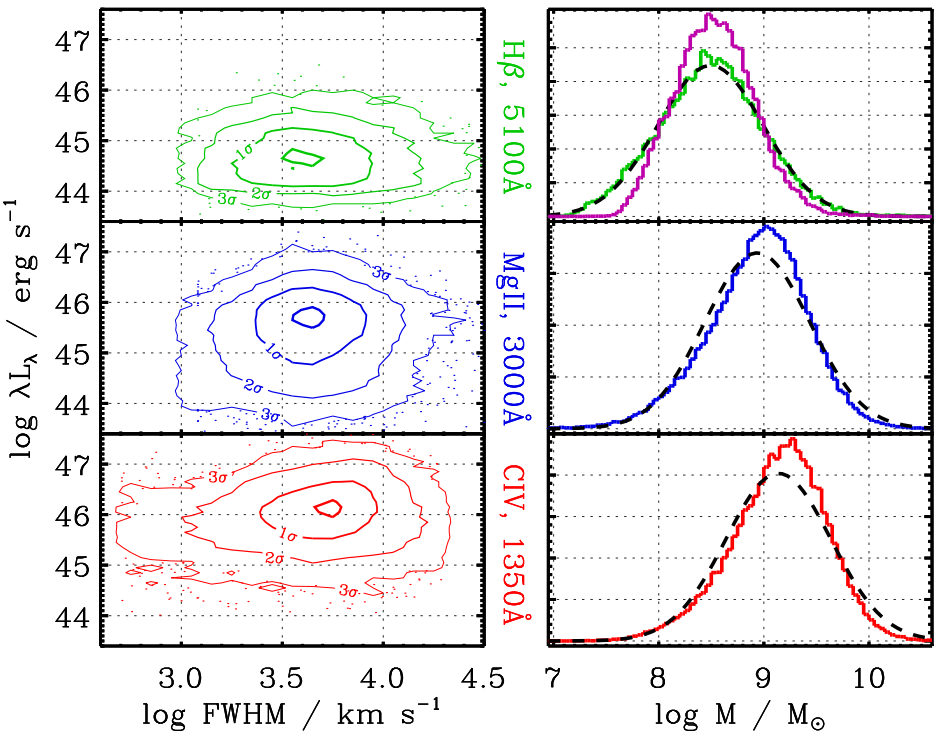

Fig. 2.5: Left panel: distributions of line widths (FWHM) and continuum luminosities (λL_λ) from the S11 catalog for the three combinations (Hβ, 5100Å), (Mg II, 3000Å) and (C IV, 1350Å). Contours are at the 10%, 68.3% (1 σ) 95.5% (2 σ) and 99.7% (3 σ) levels. Right panel: corresponding distributions of SEV SMBH mass estimates according to the Vestergaard and Peterson 2006 (Hβ and C IV), Shen et al. 2011 (Mg II) and Chiaberge and Marconi 2011 (Hβ with radiation pressure correction, Eq. 2.8, purple line) calibrations. The dashed lines are Gaussian distributions with the same mean as the SEV distributions, and a standard deviation of 0.5 dex.

Eq. 2.7. Since their distributions are log–normal, the resulting observed distribution of SMBH mass is also log–normal with width (σ_M) given by:

$$\sigma_M = \sqrt{(2 \times \sigma_{\rm FWHM})^2 + (B \times \sigma_{\lambda L_\lambda})^2} \tag{2.9}$$

where the B parameter depends on the SEV calibration (see discussion after Eq. 2.7). On the other hand, the shape of the observed mass distribution is expected to be the convolution of the intrinsic SMBH mass distribution and the uncertainty of the estimation method ($\sigma_{SEV} = 0.5$). By assuming that the intrinsic distribution of SMBH masses selected in large sample of quasars is log–normal with width $\sigma_{\rm intrinsic}$, the expected width of the observed mass

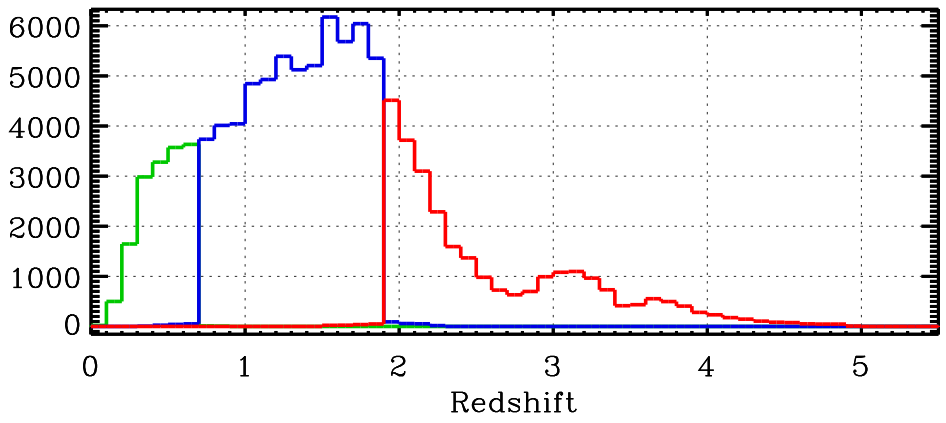

Fig. 2.6: Redshift distribution of sources in the S11 catalog. The colors identify the subsamples used in Fig. 2.5.

distribution is:

$$\sigma_M = \sqrt{\sigma^2_{\rm intrinsic} + \sigma^2_{SEV}} \tag{2.10}$$

The observed values of σ_M are 0.5, 0.48 and 0.45 dex respectively, in good agreement with the expectations from Eq. 2.9: 0.5, 0.47 and 0.47 dex. The width of the SMBH mass distribution computed by taking into account the radiation pressure correction term (Eq. 2.8) is even smaller: 0.38 dex. All the σ_M values are similar (or even smaller!) than the nominal uncertainty of the SEV method ($\sigma_{SEV} = 0.5$ dex). Therefore the observed mass distributions show the smallest possible width. Furthermore, according to Eq. 2.10 the intrinsic dispersion of the SMBH mass distribution is $\sigma_{\rm intrinsic} \ll 0.5$, i.e. all SMBHs share a single value of the mass. Note that the narrowness of the observed mass distribution can not be a consequence of a a "compensation" effect among the two observables (FWHM and λL_λ) since they are uncorrelated.

Hence, among the two postulated degrees of freedom related to M and L only one is free to vary, namely L (since we do observe sources with different luminosities), while the mass M is actually fixed. This is at odds with a reasonably broad distribution of SMBH masses. The same consideration applies when considering the whole S11 sample: since the bulk of the sources lie in the redshift range $z = 0.7$–1.9 (Fig. 2.6) where only the Mg II emission line is available the overall SMBH mass distribution is quite similar to the one in the middle right panel of Fig. 2.5, with $\langle \log M/M_\odot \rangle = 8.96$ and $\sigma_M = 0.5$

dex.

For a fixed luminosity (fixed $R_{\rm BLR}$, Eq. 2.6) the mass depends only on the line width (Eq. 2.7). If M is fixed the line width does not carry any information about the SMBH mass. Indeed, by replacing it with the average FWHM value in Eq. 2.7 all mass estimates would lie within the uncertainty $\sigma_{\rm SEV}$ from the average mass. The average SMBH mass in the distribution would not be influenced since (by definition) it is fixed by the calibration of the f factor. The SEV method based on the (Mg II,3000Å) and (C IV,1350Å) calibrations show an higher average SMBH mass with respect to the (Hβ, 5100Å) calibration. This is possibly related to the different samples by which the respective f factors have been calibrated. Moreover it is reasonable that sources at higher redshift (for which the Mg II or C IV lines enter the observed waveband) show a larger SMBH mass, having on average a larger luminosity.

A similar results have been found by Croom (2011) by analyzing large samples of spectra with either Hβ, Mg II or C IV emission lines. He estimated the SMBH mass according to the SEV method. Then he repeated the analysis by randomly scrambling the FWHM estimates among the sources, and found there were no significant changes in the resulting SMBH mass distributions. This findings have been questioned by Assef et al. (2012), who show that the information carried by the FWHM is as important as that carried by the continuum luminosity, in order to recover the M–$L_{\rm bulge}$ relation (§1.6.2). However, the two analysis procedures are not directly comparable since the former uses single epoch spectra to evaluate the line width, while the latter relies on RM observations and the line widths are measured on the RMS spectra.

We conclude that, using the SEV method to estimate the SMBH mass on the largest available AGN samples, all probed black holes share a single value for their mass ($\sigma_{\rm intrinsic} \ll 0.5$). This is a consequence of the similarity between the width of the observed mass distributions $\sigma_{\rm M}$ and the uncertainty of the SEV method $\sigma_{\rm SEV}$. Furthermore, the FWHM estimate for a single source does not guarantee a reliable estimate of the SMBH mass. On the contrary, *the average FWHM* over a large sample could provide a reliable estimate of the *average SMBH mass*. By looking at subsamples with very small or very large line widths, the resulting SEV masses will differ by more than 1 dex (or $\gtrsim 2\sigma_{\rm SEV}$) from the average one. However, this occurs in a

few cases, which are marginally relevant for the overall distribution.

Possible interpretations of the "single mass" issue discussed above are:

- the procedures employed to compile the AGN catalogs (such as S11) selects preferentially those SMBH with a given mass, and the "single mass" issue is actually a selection effect;
- the nominal uncertainty of the SEV method ($\sim$ 0.5 dex) is actually overestimated. However, it is not expected to be significantly smaller since the accuracy of the underlying calibration mass estimates are of the order of $\sim$ 0.4 dex (§2.4);
- the spectroscopic properties listed in the S11 catalog (as well as those used by Croom 2011) are not reliable. In particular, the FWHM estimates are actually random numbers not related to the actual line widths;

The last possibility point out a further limit of the SEV method. Even by assuming that all FWHM estimates are unreliable, their distribution is definitely the real one since the majority of AGNs show line widths in the range 2×10^3–10^4 km s^{-1}, i.e. the $\sigma_{\rm FWHM}$ value is perfectly reliable. The same consideration apply for $\sigma_{\lambda L_\lambda}$: brighter AGN are rare, while fainter ones would be missed by the selection criteria. Therefore, the width of the mass distribution $\sigma_{\rm M}$ (Eq. 2.9) is not expected to grow significantly beyond the 0.5 dex limit even in future analysis. Hence the SEV method is intrinsically limited: the SEV estimates on large samples comprising sources spanning the whole range of observed FWHM could in principle be compatible with a single value of SMBH mass. A possible way out would be to find a correlation between the line width and the continuum luminosity in future studies. Eq. 2.9 then would no longer apply, and in principle the observed width of SMBH mass distribution may broaden significantly.

In summary, the SEV method show several issues which may affect the reliability of the mass estimates, both in a random and systematic fashion (§2.7). When considering the largest available AGN samples the SEV mass estimates are all compatible with a single value of SMBH mass (within the uncertainty). This is a consequence of the narrowness of the distributions of the line width and of the continuum luminosity, and could imply that line widths are weakly related to the actual SMBH masses. These considerations

apply only to the analysis of the largest available samples, and may be due either to selection effects or to an inconsistency in the SEV method. The availability of independent SMBH mass estimation method is therefore crucial to settle the reliability of the SEV method.

Chapter 3

Narrow Line Seyfert 1 (NLS1)

3.1 Introduction

Narrow Line Seyfert 1 (NLS1) sources are characterized by relatively small values of the FWHM of the "broad" component of the Hβ emission line (FWHM(Hβ) $<$ 2000 km s^{-1}) and by the presence of strong blended iron lines (Osterbrock and Pogge, 1985; Goodrich, 1989). Historically, the definition of NLS1 source required the flux ratio [OIII]/Hβ $<$ 3 in order to discriminate against Type 2 sources. However, this criterion is almost always satisfied by the cut in FWHM(Hβ) broad component (Zhou et al., 2006). A typical optical spectrum of a NLS1 source in shown in Fig. 1.3. The fraction of NLS1 source among Type 1 AGNs is $\sim$ 15% (Williams et al., 2002). NLS1 sources are typically hosted in late type galaxies (Zhou et al., 2006).

At shorter wavelengths the NLS1 typically show strong flux in soft X–rays with respect to hard X–rays, i.e. a steep photon index ($\Gamma \gtrsim 2$, Pounds et al. 1986; Boller et al. 1996). As a consequence the incidence of NLS1 in soft X–ray selected AGN is relatively high ($\sim$ 40–50%, Puchnarewicz et al. 1992; Boller et al. 1996; Grupe et al. 1998). The dominance of soft X–ray radiation hints toward low intrinsic (i.e. local to the AGN host) absorption. The NLS1 show X–ray variability on timescales of the order of $\sim$ days, with extreme cases of variability over $\sim$ 1000 s (Boller et al., 1996). Furthermore, the variability amplitude on timescales $\lesssim$ 20 days appear to be larger for sources showing steep X–ray spectra than for flat X–ray AGNs (Fiore et al., 1998).

The relative narrowness of broad Hβ component, defining the NLS1 class, is usually accompanied with the other characterizing properties of NLS1

sources (strong iron emission, steep X–ray spectrum, rapid X–ray variability). Since these properties occur together they may be related to a single physical property. Given the small widths of the Balmer lines it has been suggested that NLS1 sources may be characterized by relatively small SMBH masses ($< 10^8 M_\odot$) and high Eddington ratios ($\ell \sim 1$) (Laor, 2000). Another possibility is that the characteristic size of the BLR in NLS1 is greater than for typical Broad Line AGNs (BLAGNs) (Wandel and Boller, 1998).

It is worth to notice that there is no abrupt change in the observed properties between NLS1 and BLAGNs, i.e. the properties of the two subclasses are smoothly joined without jumps or thresholds (Goodrich, 1989; Véron-Cetty et al., 2001). As an example, Fig. 3.1 shows the distribution of FWHM(Hβ) estimates in the S11 catalog. The NLS1 defining threshold of FWHM(Hβ) $= 2000$ km s^{-1} is shown with a dashed lines. Given the smoothness of the distribution of FWHM(Hβ) (as well as the other properties) this threshold is somewhat subjective.[1]

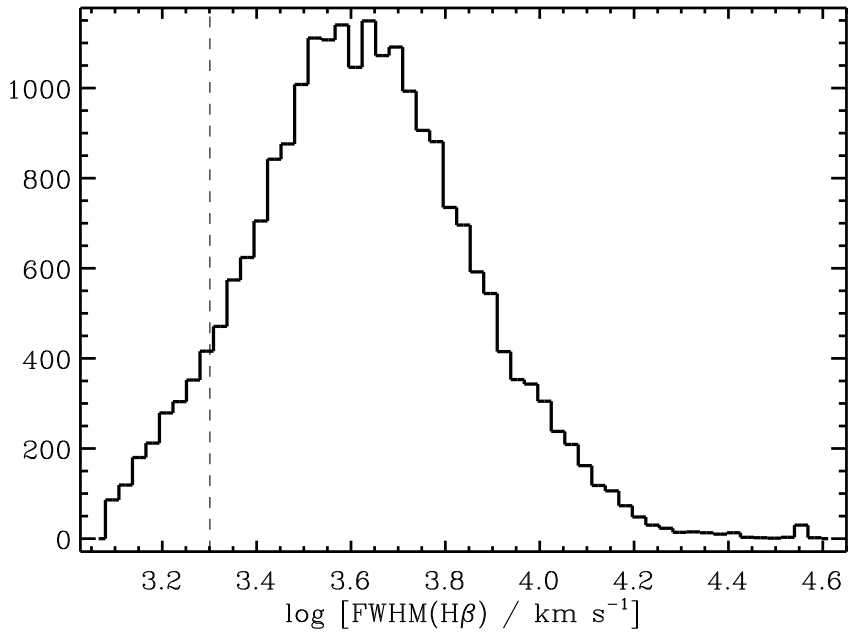

Fig. 3.1: Distribution of FWHM(Hβ) in the S11 catalog.

NLS1 are typically radio–quiet (§1.2.5) or even undetected, although there are a few sources showing powerful emission at radio wavelength,

[1] e.g. Zhou et al. (2006) adopt a threshold of FWHM(Hβ) $= 2200$ km s^{-1}.

with Radio–loudness parameter ($R_{\rm loud}$) exceeding 10^3 (Yuan et al., 2008). The fraction of RL sources among NLS1s is ∼7%, while that of BLAGN is 10–20%, i.e. RL–NLS1 are more rare than RL–BLAGN (Komossa et al., 2006). Yuan et al. (2008) have compiled a catalog of 23 Radio–Loud Narrow Line Seyfert 1 (RL–NLS1) with $R_{\rm loud} > 100$. All sources in the catalog are unresolved at the scale of a few arcseconds, and show flat or even inverted radio spectra ($\alpha_\nu > -0.5$) at GHz frequencies. The sources show variability at radio frequencies from which it is possible to estimate the brightness temperature which is $\gtrsim 10^{11}$ K, suggesting the presence of relativistic jets closely aligned to the line of sight.

NLS1 are an interesting case study because of their extreme observational properties. In particular, the long standing question is whether they represent an intrinsically different population of AGNs, or rather if they "fit" into the standard unification model (§1.3) for some particular value of the fundamental parameters, e.g. small angle between the normal to the accretion disk and the line of sight. In order to address this issue it is necessary to reliably estimate the SMBH mass (§3.2). Furthermore, the recent γ–ray detection of a few NLS1 have shown that some of these sources show blazar–like behavior (§3.3).

Thorough reviews on the observational properties of NLS1 are given in (Pogge, 2000; Komossa, 2008).

3.2 The SMBH mass of Narrow Line Seyfert 1

The relatively small widths of the broad Hβ components in NLS1, when interpreted as a measure of the velocity dispersion of the BLR clouds, suggest that the SMBH masses in NLS1 sources are smaller than for "canonical" BLAGN. By estimating the SMBH mass with both the SEV method (§2.6) and the M–σ relation (using the width of [O III] line as a surrogate for σ_*, §1.6.2), Grupe and Mathur (2004) and (Mathur and Grupe, 2005) claimed that NLS1 lie systematically below (∼ 0.5 dex) the M–σ_* of quiescent galaxies and BLAGN. This indicates that the black hole masses of NLS1 are systematically smaller than the black hole masses of BLAGN for a given value of σ_*. The same considerations apply when considering objects of the same luminosity: NLS1 appear to accrete at a higher Eddington ratio with respect to BLS1, with some objects exceeding the Eddington luminosity (Zhou et al., 2006).

This may imply that the NLS1 are AGN observed at an early phase of evolution, in which SMBH is still under massive with respect to those in BLAGN (Mathur et al., 2001; Mathur and Grupe, 2005). However, these results depend strongly on the reliability of both the σ_* and SEV mass estimates. In particular, the use of the whole [O III] profile as a proxy for the bulge stellar velocity dispersion σ_* may not be appropriate since NLS1 often show prominent blue wings and/or strong blueshifts. By taking into account these effects Komossa and Xu (2007) have shown that NLS1 follow the same M–σ relation as BLAGN. Furthermore, the same result can be obtained by using the (lower ionization) [S II] line width as a proxy for σ_*.

The SEV mass estimates may also be affected by issues specific to NLS1. As discussed in §2.3, by assuming that the BLR has a thin disk–like geometry coplanar with the accretion disk, the width of the line profile depends on the angle α between the normal to the disk and the line of sight. Moreover the dependence become quite strong for almost pole–on views ($W \propto \sin\alpha$). The relative "narrowness" of the broad Hβ component in NLS1 may be related to the small values of α. However as discussed in §2.7, this occurrence may strongly affect the SEV method and the resulting SMBH mass would be systematically underestimated by a factor which depends on α. The average systematic error can be derived as follows: assume that a Type 1 AGN is classified as NLS1 if the angle of sight is smaller than a critical angle $\alpha < \alpha_{\rm cr}$, while it is classified as BLAGN if $\alpha_{\rm cr} < \alpha < \alpha_{\rm max}$, where $\alpha_{\rm max} \sim 40^\circ$ is the aperture of the obscuring torus. By requiring the fraction of NLS1 among BLAGN sources to be $N_{\rm NLS1} \sim 15\%$ (Williams et al., 2002) we find:

$$\alpha_{\rm cr} = \cos^{-1}\left[1 - N_{\rm NLS1} \times (1 - \cos\alpha_{\rm max})\right] \sim 15^\circ. \tag{3.1}$$

The calibration f factor for both NLS1 ($f_{\rm NLS1}$) and BLAGN ($f_{\rm BLAGN}$) sources can be estimated by averaging Eq. 2.5 over $0 < \alpha < \alpha_{\rm cr}$ and $\alpha_{\rm cr} < \alpha < \alpha_{\rm max}$ respectively. By assuming $H/R \sim 0.1$, Decarli et al. (2008) found $f_{\rm NLS1}/f_{\rm BLAGN} \sim 3$. This is the average systematic error in SEV mass estimates for NLS1 sources.

A further issue in the SEV method may be related to radiation pressure. Since NLS1 sources are believed to accrete close to the Eddington limit, the latter is expected to play a role in the BLR clouds dynamic. By considering a simple model that take into account the effect of radiation pressure in SEV

mass estimates (Eq. 2.8), Marconi et al. (2008) have calibrated the f factor by re–analyzing the sample of reverberation mapped sources of Peterson et al. (2004). Then, by using the new expression for the mass estimate they computed the SMBH mass for a sample of 110 Type 1 AGN sources. By dividing the sample into NLS1 and BLAGN according to the width of the Hβ line, they found that the mass distributions for the two subsamples overlaps almost perfectly once the radiation pressure correction is taken into account.

In summary, the issue of whether the SMBH mass of NLS1 sources are significantly lower (and the Eddington ratios correspondingly higher) than that of BLAGN is still open. The mass estimates from both the M–σ relation (using the width of [O III] as a proxy for σ_*) and the SEV method reported in the literature are inconsistent. In particular, the SEV method as is currently employed may be affected by systematic errors. Hence an independent SMBH mass estimation method is required in order to address the issue.

A closely related problem is whether the distribution of SMBH mass of Type 1 AGNs is actually bimodal (with NLS1 separated from BLAGN sources) or rather a smooth continuous distribution. Since the observational properties does not show abrupt jumps the latter hypothesis is to be preferred. This implies the existence of "intermediate" sources between the class of NLS1 and BLAGN sources with FWHM(Hβ) $\sim$ 2000 km s^{-1}. A candidate intermediate source will be discussed in §3.4.

3.3 High energy emission from NLS1 sources

As discussed in §3.1 the majority of NLS1 sources are radio quiet. The SED of these objects extends at most to the hard X–ray waveband. Also, the RL–NLS1 were thought to be inactive in γ-rays, although several authors speculated the occurrence of similarities with blazars (Zhou et al., 2003; Komossa et al., 2006; Zhou et al., 2007; Yuan et al., 2008).

In 2008, the important discovery of γ-ray emission from the RL–NLS1 source PMN J0948+0022 (Foschini et al., 2009a; Abdo et al., 2009a) confirmed these similarities, i.e. the presence of a jet closely aligned to the line of sight as a source of Compton up–scattered γ–ray photons. Variations of the γ–ray flux of a factor 2.2 rules out the possibility that the γ–ray emission is due to a starburst contribution (Abdo et al., 2009b). Shortly after this discovery, three more RL–NLS1 had been observed in γ–rays (Abdo et al.,

2009c): 1H 0323+342, PKS 1502+036 and PKS 2004–447, thus confirming the existence of a new class of γ–ray emitter (after blazars and radio galaxies): the γ–ray active Narrow Line Seyfert 1 (γ–NLS1).

The detection of γ–rays from the four mentioned RL–NLS1, as well as their radio properties (namely temporal variability, flat spectrum and high brightness temperature) together with the γ–ray detection suggests the presence of a relativistic jet closely aligned to the line of sight (Foschini et al., 2009b; Gu and Chen, 2010). The broad band SED of the aforementioned γ–NLS1 sources have been analyzed with the one–zone leptonic model of Ghisellini and Tavecchio (2009). The power carried by the jets of PMN J0948+0022 and PKS 1502+036 is in the range of FSRQ, while that of 1H 0323+342 and PKS 2004–447 is in the range of BL Lac sources (Abdo et al., 2009c).

AGNs producing such powerful jets are typically hosted in giant elliptical galaxies (Marscher, 2009), while low power, mildly relativistic and poorly collimated radio jets are observed in a few spiral galaxies hosting Seyfert nuclei (e.g. Keel et al., 2006, and references therein). The observation of powerful jets in NLS1 sources (commonly believed to be hosted in late type galaxies Zhou et al. 2006) is at odds with this scheme. Note however that the host morphology of the γ–NLS1 is not yet determined, except possibly for 1H 0323+342 for which we have an *HST*/WFPC2 optical image of the host galaxy. The host shows a ring–like structure of 15.6 kpc in diameter and the entire galaxy looks like a one–armed spiral (Zhou et al., 2007). Another study, based on NOT data, suggests that 1H 0323+342 may be the remnant of a galaxy merger (Antón et al., 2008).

Recently, three more γ–NLS1 sources have been detected[2] by *Fermi*/LAT (Foschini et al., 2011).

3.3.1 γ–ray variability in NLS1

The γ–ray variability of PMN J0948+0022[3], 1H 0323+342, PKS 1502+036 and PKS 2004–447 has been discussed in (Calderone et al., 2011). Here I will briefly review the results of this work.

[2]The current status of candidate γ–NLS1 monitoring is being updated on the site http://tinyurl.com/gnls1s

[3]The variability of PMN J0948+0022 is discussed also in Abdo et al. (2009b); Foschini et al. (2011).

I analyzed the *Fermi*/LAT light curves of the aforementioned RL–NLS1 galaxies in order to put the γ–ray variability on a firm basis, and to find the minimum variability time-scale. The data span the period from 2008 august 4 to 2010 october 08 ($\sim$26 months) I computed the average integrated flux for each source analyzing all data over the entire period of 26 months. Then I extracted light curves with time binning of 15 days (the time binning for PKS 2004-447 is 30 days) using a TS threshold of 10 (Test Statistic = 10, roughly equivalent to 3σ, Mattox et al. 1996). If the detection in a time bin was not significant (TS$<$10) we computed a 2σ upper limit to the flux. Middle panels show the photon indices for points with significant detection, assuming a simple power law model ($F(E) \propto E^{\Gamma}$) for each source in the range 0.1 – 100 GeV. Horizontal dashed lines in both upper and middle panels are the integrated (over 26 months) flux and photon index respectively. Lower panels show the TS value (plus symbol) and number of counts (triangle symbol) for each bin with significant detection. By performing a chi–squared test against the null hypotesis of constant flux I find that all sources show variability on a $\sim$ 2 year timescale with high significance.

This rules out the possibility that the γ–ray emission is due to a starburst activity. Thus, the data support the hypotesis that γ–ray photons are associated to the presence of a jet. We cannot exclude the possibility of a starburst activity but its contribution would be negligible compared to the jet emission, since the γ-ray luminosities (Table 3.1) found in our RL-NLS1 are at least four order of magnitude greater than the archetypal starburst galaxy M82 hosting a quiescent black hole (Gaffney et al., 1993) and whose γ–ray luminosity in the 0.1–100 GeV range is $\sim 10^{40}$ erg s^{-1} (Abdo et al., 2010a).

I further proceeded on the analysis of the light curves in order to compute the minimum *e*-folding timescale for each source. We extracted light curves with different time binnings starting from 30 days. When the detection is significant (TS$>$10) I re–run the analysis halving the time bin interval, down to a minimum of approximately 6 hours (roughly corresponding to four *Fermi* orbits, thus ensuring that each source is observed at least twice for each temporal bin). Then, I considered all combinations of non-overlapping time bins with (i) significant detection (TS$>$10), (ii) flux and count significant difference at the 3σ level and (iii) count greater than 3. For such pairs of

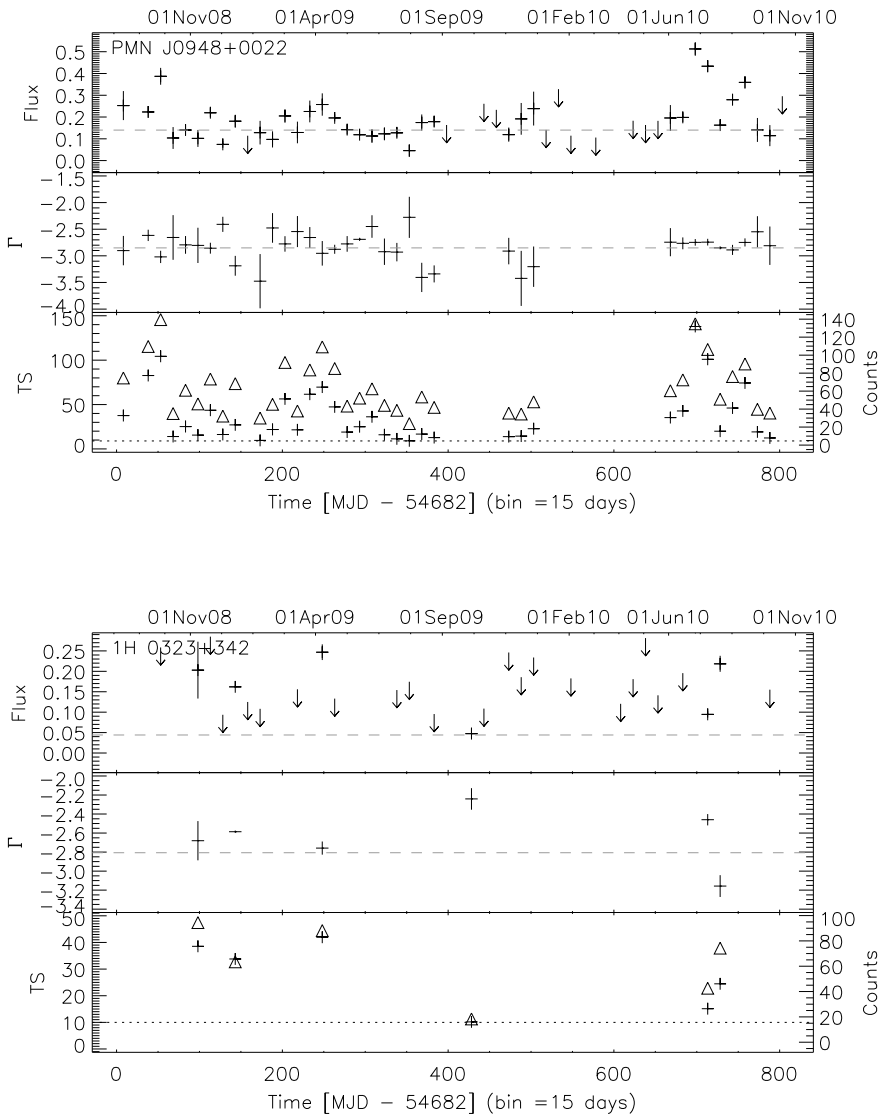

Fig. 3.2: Upper panels: light curves of the four RL-NLS1 for detections with TS>10. Fluxes are given in units of 10^{-6} ph cm^{-2} s^{-1} in the range 0.1–100 GeV. Vertical error bars correspond to 1σ errors, while horizontal bars corresponds to the time binning (15 days for PMN J0948+0022, 1H 0323+342 and PKS 1502+036, 30 days for PKS 2004-447). Upper limits (TS<10) at 2σ level are denoted by arrows. Middle panels: photon indices assuming a simple power law model ($F(E) \propto E^{\Gamma}$) for each source in the range 0.1–100 GeV. Vertical error bars correspond to 1σ errors. In both panels horizontal dashed lines are the integrated (over the entire period of 26 months) flux value and photon index respectively. Lower panels: TS values (plus symbols) and number of counts (triangle symbols, values on the right axis), the horizontal dotted line is the threshold (TS = 10).

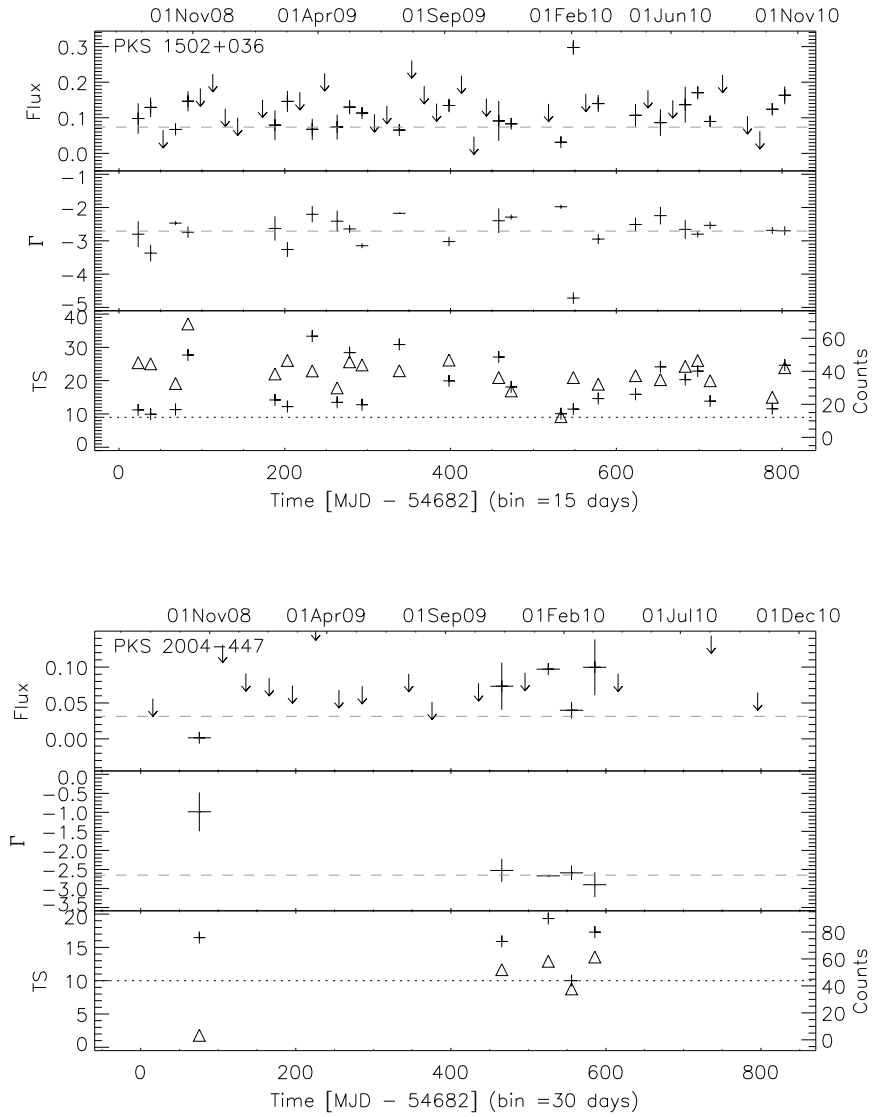

Fig. 3.2: (continued)

bins I computed the *e*-folding timescale as:

$$\tau_{ij} = \left| \frac{t_i - t_j}{\ln F_i/F_j} \right| \tag{3.2}$$

where i and j are the indices of the involved time bins ($i > j$). The associated error (at 3σ level) is computed through error propagation. Finally, I computed the minimum *e*-folding variability timescale as $\tau = \min(\tau_{ij})$, and

Table 3.1: Data and results of the analysis on the four RL-NLS1 sources. Columns are: (1) name of the source; (2) integrated γ-ray luminosity (0.1 – 100 GeV) over the entire period (26 months) with errors at 1σ level; (3) photon index with errors at 1σ level; (4) χ^2 and (5) DOF computed on the light curves of Fig. 3.2 in the null hypotesis of constant flux equal to the integrated flux; (6) minimum *e*-folding variability timescale with error at 3σ level.

Source	L_γ [10^{45} erg s^{-1}]	Γ	χ^2	DOF	τ [days]
PMN J0948+0022	250.00 ± 13.04	-2.851 ± 0.007	528	33	3.3 ± 2.5
1H 0323+342	0.16 ± 0.04	-2.807 ± 0.010	2575	5	17.7 ± 14.4
PKS 1502+036	41.45 ± 4.10	-2.708 ± 0.007	385	21	12.0 ± 9.0
PKS 2004-447	3.85 ± 0.70	-2.650 ± 0.006	4032	4	28.4 ± 18.5

associate the corresponding error. The results are shown in Tab. 3.1.

The sources display an *e*-folding minimum timescale variability in the range of 3–30 days. In particular, variability of the order of ∼days has been found for PMN J0948+0022, and of the order of ∼tens of days for 1H 0323+342, PKS 1502+036 and PKS 2004-447. Note that these are actually upper limits to the minimum variability timescales, since I required the source to be significantly detected in any time bin considered for the calculation of τ_{ij}. Variability could have occurred on shorter timescales but being missed because of non–significant detection.

The minimum measured variability timescales in blazars can be as low as 200 seconds at very high energies (E>200 GeV) and 800 seconds at X-rays (see Aharonian et al., 2007, and references therein). At *Fermi*/LAT energies variability on scales of few hours has been detected in several blazars (e.g. Foschini et al., 2008; Tavecchio et al., 2010; Foschini et al., 2010). In particular, the bright blazars 3C 454.3 and PKS 1510-089 showed variability on scales of 3–6 hours with flux $\sim 10^{-5}$ ph cm^{-2} s^{-1} (Tavecchio et al., 2010), that is 1–2 orders of magnitude greater than the flux of the sources analyzed here. As discussed above, I expect to measure longer timescales on weaker sources, as a consequence of the longer time integration required to significantly detect the source. Our minimum timescale estimates are indeed approximately 1–2 orders of magnitude longer compared to those of the above-mentioned blazars. Therefore, I cannot exclude the possibility that variability in γ–NLS1 is as fast as the one observed in some of the most luminous blazars.

3.4 The case of B2 0954+25A

As discussed in §3.1, the NLS1 defining threshold of FWHM(Hβ) = 2000 km s^{-1} is somewhat subjective. Therefore we expect the existence of sources with FWHM(Hβ) $\sim$ 2000 km s^{-1} whose properties are "intermediate" between the class of NLS1 and BLAGN. One such candidate is B2 0954+25A (z=0.712, Burbidge and Strittmatter 1972) a blazar with many interesting observational properties. This source has been thoroughly analyzed in Calderone et al. (2012a). Here I will briefly review the results of this work.

At radio wavelengths is a compact, radio–loud, flat–spectrum radio quasar whose radio emission extends to very low radio–frequencies (74 MHz, Cohen et al. 2007). The radio spectrum is usually flat and becomes inverted during burst activity (Torniainen et al., 2005). The jet is clearly visible in several radio maps: see e.g. the VLA radio maps at 1.64 GHz in Murphy et al. (1993) and the VLBA radio maps at 22 and 43 GHz in Lister and Smith (2000). The core component has angular size $\sim 0.23 \times 0.07$ mas (at 15 GHz), corresponding to a linear size of 1.6×0.49 pc (Kovalev et al., 2005). Several components in the jet show superluminal motion (up to 12c, Kellermann et al. 2004). A one–sided jet (projected size $\sim$50 kpc) extends from the core in the south–west direction (Liu and Zhang, 2002).

In the optical band, the source is unresolved, variable (Pica et al., 1988) and slightly polarized (1.29%, Wills et al., 1992), with m_i $\sim$18 mag. The bolometric luminosity (estimated from SED fitting, Woo and Urry 2002) is log($L_{\rm bol}$/erg s^{-1}) = 46.59. SEV SMBH mass estimates are log($M/M_{\odot}$) = 8.7 (Liu et al., 2006) and log($M/M_{\odot}$) = 9.5 (Gu et al., 2001). Both these estimates rely on a FWHM estimate of the Hβ emission line given in Jackson and Browne (1991), who found FWHM(Hβ) = 65 Å (rest frame), corresponding to $\sim$4000 km s^{-1}. The source is also present in the S11 catalog S11 report a FWHM(Hβ) = 1870 km s^{-1} and log($M/M_{\odot}$) = 8.6 (computed with Hβ), or 9.3 (computed with Mg II). The spectrum analyzed in S11 is exactly the same as the one I use in §3.4.1.

Several X–ray facilities (*Swift*/XRT, *Chandra*, *ROSAT*, *Einstein*) observed the source at different times measuring fluxes in the range (2.5–20) $\times 10^{-13}$ erg cm^{-2} s^{-1} (§3.4.2 and Fig. 3.5). Finally, B2 0954+25A is present in both the 1yr and 2yr *Fermi* Large Area Telescope (LAT) point source catalogs (Abdo et al., 2010b, 2011, with catalog names 1FGL J0956.9+2513 and

2FGL J0956.9+2516 respectively).

3.4.1 Optical spectroscopy

I used optical spectra from the *Isaac Newton Telescope* (INT) and from SDSS (DR7)[4] (see Fig. 3.3). The spectrum from INT (observed on 16th Dec. 1987) has been derived directly from the plot given in Jackson and Browne (1991, their Fig. 2), thus it is suitable only for a qualitative analysis. A qualitative comparison of the spectra by INT and SDSS taken $\sim$9 years apart shows that the continuum has changed both in intensity (by a factor $\sim$5) and in slope. The intensity and shape of the Balmer line seem to be the same in both spectra. In §3.4.2 I also analyze the broad–band SED (lower panel of Fig. 3.5) of the source, considering also the photometric data from SDSS, taken $\sim$1 year before the SDSS spectroscopic observations. Again, we see that a change in intensity of the optical emission of a factor $\sim$10 occurred in just 1 year. Also, a change in slope occurred, as indicated by the photometric data in the 5 available bands. Thus, we conclude that B2 0954+25A has been observed in at least three emission states at optical wavelengths which differs in intensity: from the dimmer one (SDSS/photometric), through an intermediate one (INT), to the brighter one (SDSS/spectroscopic). The spectral slope is correlated to the change of state.

The FWHM(Hβ) estimate available in literature are inconsistent. Therefore I ran my own analysis of the SDSS spectrum. I performed a fit of the spectrum using five components model (**Model 1**): a power–law to account for the continuum emission, four Gaussian–shaped emission lines to account for the Hβ (both narrow and broad component) and the [OIII] 4959Å, [OIII] 5007Å lines. FWHM and velocity offset of the narrow lines are forced to be the same. Results are shown in Fig. 3.4 (upper panel). Although Model 1 fits reasonably well the spectrum, the residuals of the fit look random everywhere, except in two regions: 4840–4900Å and 4930–4945Å, in which the residuals are quite "coherent", suggesting the presence of further components. In order to accounts for these residuals I ran another fit by adding another emission line component named Hβ^* (**Model 2**, Fig. 3.4 lower panel). The extra component accounts well for the asymmetry of the Hβ profile, and the residuals in the region now look random. Therefore our Model 2 seems

[4] Data from DR8 does not differ significantly from DR7.

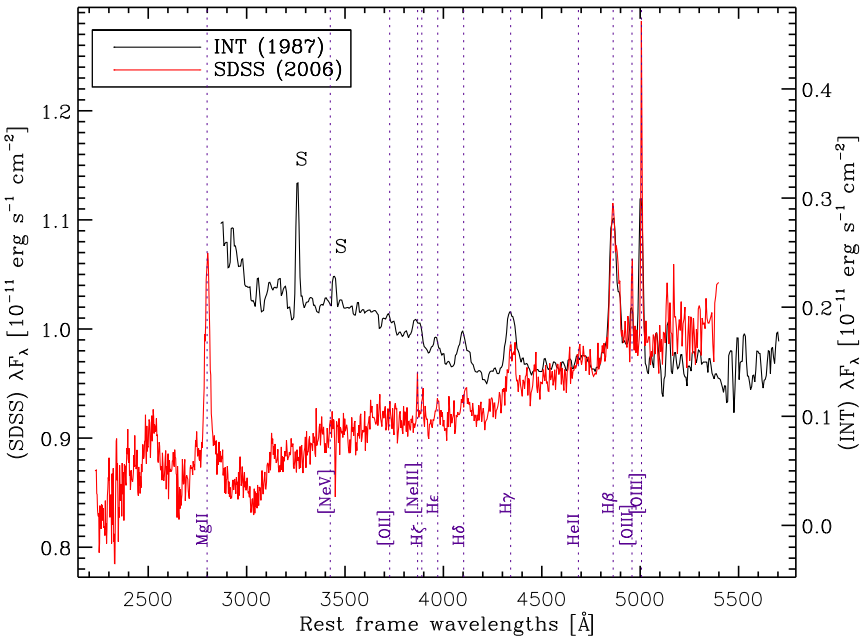

Fig. 3.3: Optical spectrum of B2 0954+25A observed by SDSS in 2006 (red line, flux scale on the left axis) and with the *Isaac Newton Telescope* (INT) in 1987 (black line, flux scale on the right axis). The range of values covered by both axes is exactly the same ($\sim 0.5 \times 10^{-11}$ erg s^{-1} cm^{-2}) so that spectra can be directly compared. SDSS spectrum have been de–reddened using Cardelli et al. (1989) with E(B–V)=0.0375, transformed to the rest frame using our redshift estimate (z=0.70747, see text) and rebinned by a factor of 2. The INT spectrum has been derived from the plot given in Jackson and Browne (1991, their Fig. 2) and transformed to rest frame. The "S" letter denote telluric lines. Some of the most important emission lines are highlighted. The spectra show that the continuum has changed both in intensity (by a factor ∼5) and in slope. The intensity and shape of the Balmer lines seem to be the same in both spectra.

to be the best description of the spectrum of B2 0954+25A in the 4810–5100 Å range. The spectral fitting parameters of Model 2 are quite similar to those from S11 (Tab. 3.2).

The FWHM(Hβ) estimates found with both Model 1 and 2 of our fit is significantly lower than the value reported in literature is ($\sim$ 4000 km s^{-1}, Jackson and Browne 1991). Since the Hβ profiles observed with INT and SDSS (Fig. 3.3) overlap perfectly, we can exclude a variation in the line profile, and conclude that previous value was likely overestimated.

Fig. 3.4 show that the broad Hβ emission line can hardly be modeled

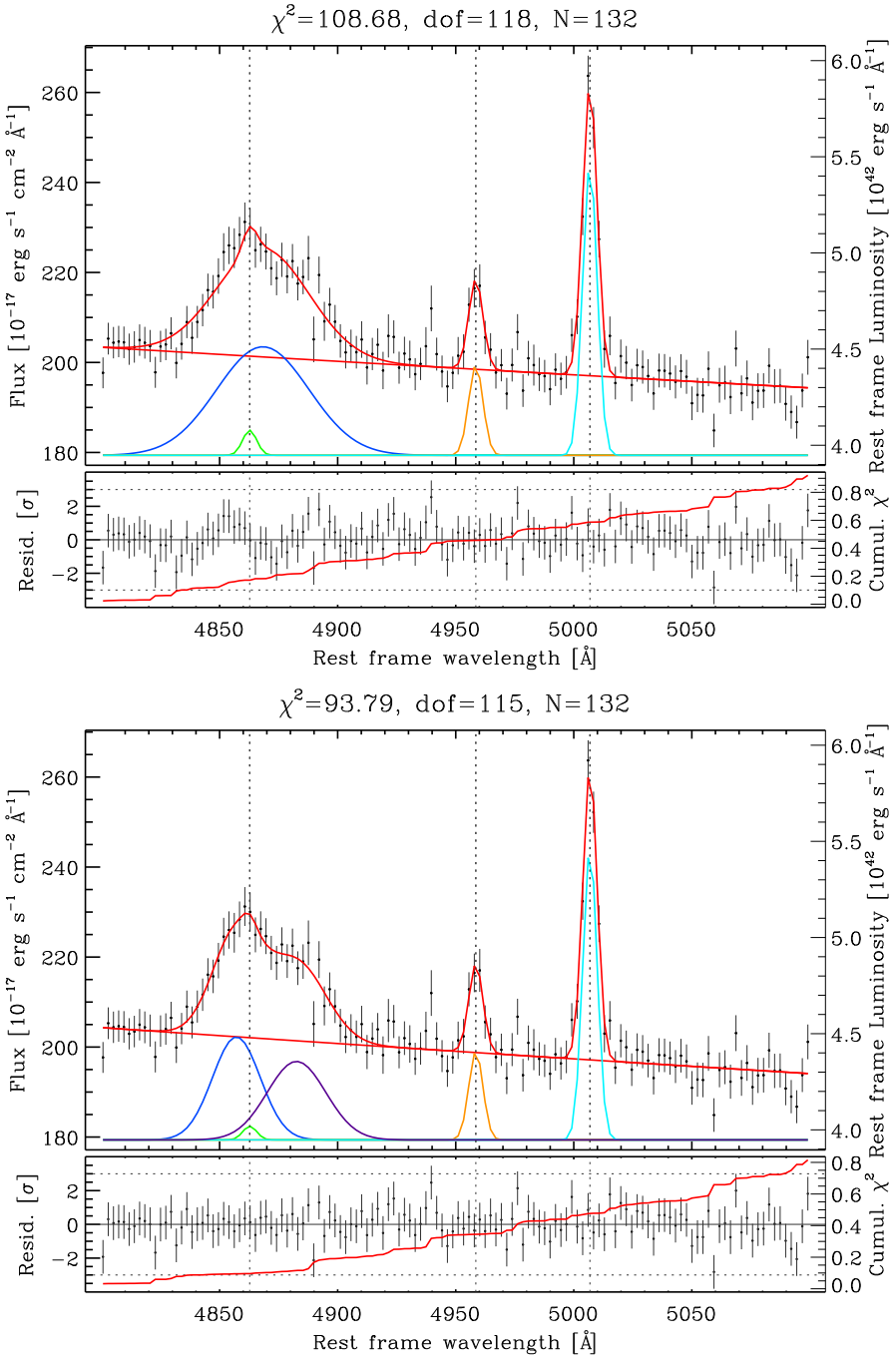

Fig. 3.4: Spectrum of B2 0954+25A (black points with 1σ error bars) and fitted model (red line) in the range 4810–5100 Å. Upper panel: fit of Model 1. Lower panel: fit of Model 2 (see text). All quantities are quoted in rest frame. The model components are: continuum (red), broad Hβ component (blue), narrow Hβ component (blue), [O III] 4959Å (orange), [O III] 5007Å (cyan). Lower panel (Model 2) show a further component: Hβ^* (purple). Dotted lines are the rest frame wavelengths of the emission lines. The residuals are shown in units of standard deviation. Red solid line is the cumulative reduced chi–squared (values on right axis).

Table 3.2: Model parameters as derived from optical SDSS spectrum fitting, and corresponding quantities in the Shen et al. (2011) catalog.

Parameter	Model 1	Model 2	S11	Units
Lum. ($H\beta_{broad}$)	26.3 ± 2.2	12.9 ± 6.3	23 ± 13	[10^{42} erg s^{-1}]
Lum. ($H\beta^*$)	—	12.1 ± 5.8	—	[10^{42} erg s^{-1}]
Lum. ($H\beta_{narrow}$)	0.93 ± 0.58	0.50 ± 0.92	8 ± 42	[10^{42} erg s^{-1}]
Lum. ([OIII], 5007)	11.07 ± 0.59	11.01 ± 0.58	12.2 ± 1.9	[10^{42} erg s^{-1}]
FWHM ($H\beta_{broad}$)	2830 ± 220	1470 ± 320	1870 ± 600	[km s^{-1}]
FWHM ($H\beta^*$)	—	1790 ± 600	—	[km s^{-1}]
FWHM ($H\beta_{narrow}$)	431 ± 24	428 ± 24	1200 ± 400	[km s^{-1}]
V_{off} ($H\beta_{broad}$)	344 ± 75	$-(350 \pm 270)$	$-(1250 \pm 630)$	[km s^{-1}]
V_{off} ($H\beta^*$)	—	1220 ± 400	—	[km s^{-1}]
V_{off} ($H\beta_{narrow}$)	$-(0 \pm 10)$	1 ± 10	37 ± 200	[km s^{-1}]
λL_λ (5100Å)	220.88 ± 0.80	220.59 ± 0.78	220.73 ± 0.74	[10^{44} erg s^{-1}]
Continuum index	$-(0.75 \pm 0.13)$	$-(0.85 \pm 0.11)$	$-(0.709 \pm 0.018)$	

with a single Gaussian profile, nor with any symmetric line profile such as the often quoted logarithmic profile (Blumenthal and Mathews, 1975), since the red wing is highly asymmetric. Iron emission lines in the range 4840–4900 Å are usually much weaker than the Balmer lines (Capriotti et al., 1979), thus such profile is hardly the result of a blending of different lines. As discussed in §2.3, the asymmetry of emission lines may be due to either specific geometries of the emitter and/or absorber, or non–virialized motion (e.g. outflows). The last hypothesis, in particular, may affect the reliability of SEV mass estimates. The virialized part of the line profile may be just the symmetric core, while the red wing may be due to non–virialized components. Of course the reasoning can be inverted: the "real" Hβ line profile may be much wider, but some intervening gas could absorb radiation only on the blue side. Currently I have no evidence to exclude any of these hypothesis. The FWHM estimates provided by the fitting procedure can be used to estimate the SMBH mass, as discussed in §3.4.3.

3.4.2 Broad–band SED

To build the broad–band SED (Fig. 3.5) I collected publicly available data from several facilities using NED. As discussed in §1.2.6, the broad band SED of blazars is the superposition of a standard RQ–AGN SED (torus, accretion disk, X–ray emitting corona, shown with dotted gray lines in bottom panel of Fig. 3.5) and the emission from the relativistic jet. The latter is due to the contribution of synchrotron emission from relativistic electrons flowing in the jet (the IR hump), and high energy emission resulting from the Compton up–

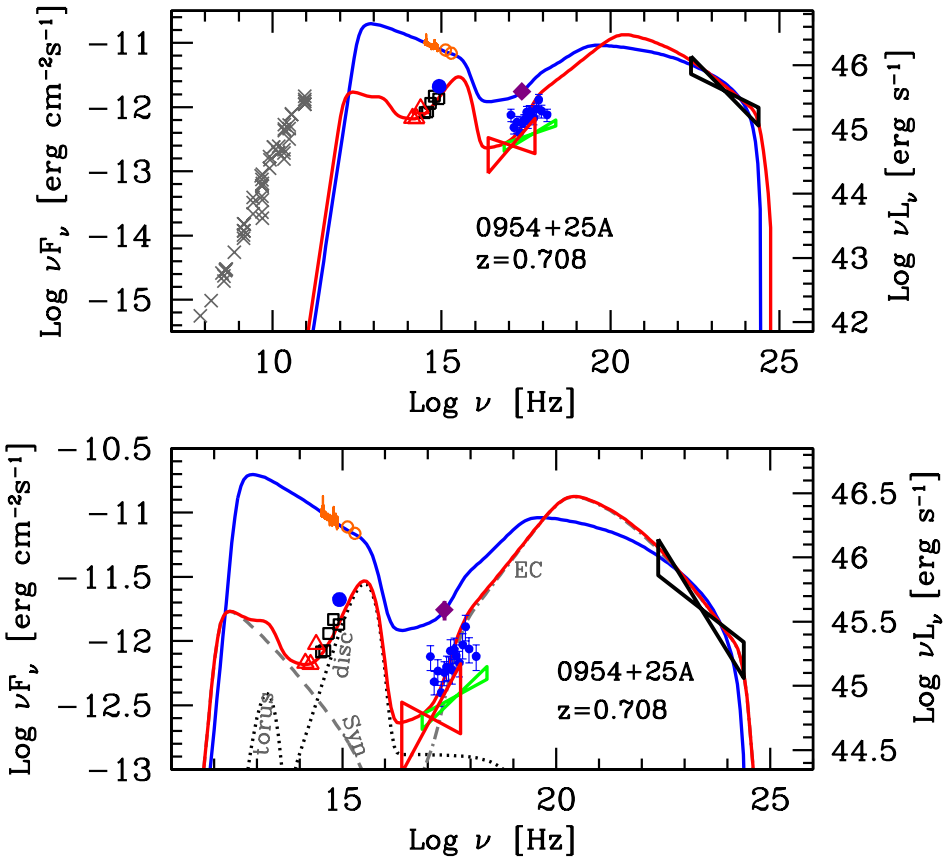

Fig. 3.5: Broad band spectral energy distribution, and related models, of B2 0954+25A. Data are provided by several facilities (see references in Calderone et al. 2012a). Upper panel shows all available data, from radio to γ–ray energies, as well as the SED models in the low and high synchrotron state. The lower panel shows a detailed view of the SED from IR to γ–rays, and highlights the most important components of the models.

scattering of ambient photons from the same population of electrons (high energy hump). The ambient photons are generated either by the synchrotron emitting electrons (Synchrotron Self Compton) or by other components, e.g. IR torus, accretion disk, or BLR (Ghisellini and Tavecchio, 2009).

The most notable feature of the broad–band SED of B2 0954+25A is the large variability in the optical, from a disk to a jet dominated state. These correspond to the different emission states discussed in §3.4.1. The change of state can be interpreted as a change in quantities related to the jet emission

(namely the magnetic field and the injected power), and does not necessarily involves the disk luminosity and/or the BLR properties. Indeed, no change in the broad Hβ emission line profile or luminosity is detected between the two considered optical spectra (Fig. 3.3). By assuming that the disk component is well described by a standard Shakura and Sunyaev (1973) accretion disk model it is possible to estimate the SMBH mass by comparison with data in the disk dominated state[5].

The values of the physical parameters derived from the SED modeling are similar to those found by fitting *Fermi* blazars (Ghisellini et al., 2010), with the black hole mass being in the low end of the distribution (§3.4.3). The picture that emerges is that of a typical *Fermi* blazar, with a flat radio spectrum produced by a powerful jet, and black hole mass significantly smaller than $10^9 M_\odot$. The source cycles through different emission states, characterized by different amount of power emitted by the jet. Although the SED parameters are only rough estimates of physical quantities, the possibility to model two different states of the same source provides at least a clue that the parameters kept fixed in both models (black hole mass, disk luminosity, BLR radius, covering factor) are reliable.

Comparison with 3C 273 and PMN J0948+0022

In Fig. 3.6 I compare the broad band SED of B2 0954+25A to that of 3C 273 (upper panel) and PMN J0948+0022 (lower panel, §3.3). Both sources have been analyzed in Ghisellini et al. (2010). The radio spectrum of the prototypical blazar 3C 273 shows a flat spectrum comparable in luminosity with B2 0954+25A, although slightly steeper. At the lowest observed frequencies the two SED are markedly different: whereas the 74–365 MHz radio spectral index of 3C 273 become steep ($\alpha \sim -0.5$), the spectral index of B2 0954+25A remains flat ($\alpha \sim -0.2$). This behaviour can be explained with a different amount of relativistic beaming which boosts the jet emission in B2 0954+25A. At shorter wavelengths 3C 273 is $\sim$1 order of magnitude more powerful than B2 0954+25A. If emission in both sources occur at approximately the same Eddington ratio as suggested by SED modeling, the luminosity ratio at optical/UV wavelengths ($\sim$ 3) provides an estimate for the mass ratio. Since $\log(M/M_\odot)$ of 3C 273 is 8.9, for B2 0954+25A I ex-

[5]This method will be thoroughly discussed in (§4.3, 6.3).

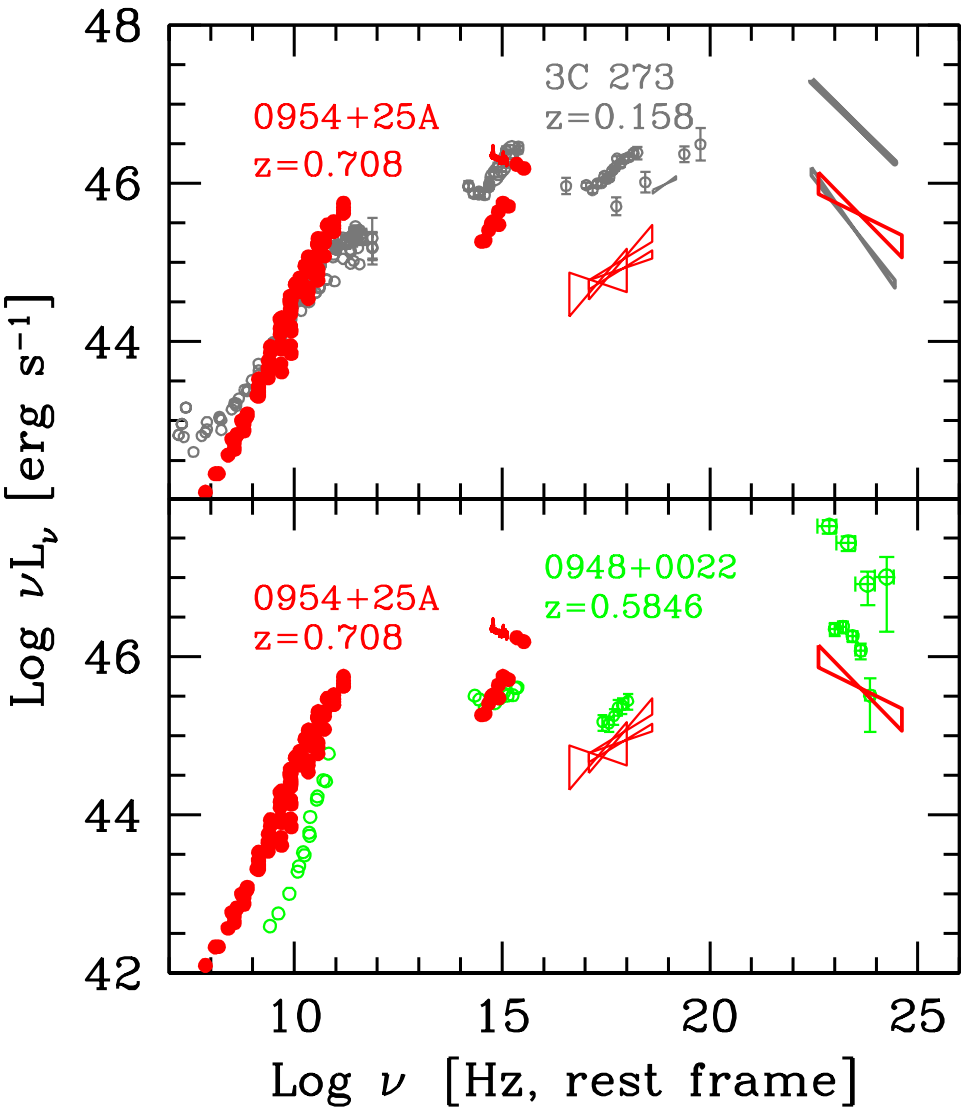

Fig. 3.6: Comparison of the SED of B2 0954+25A with the SED of 3C 273 (top panel) and PMN J0948+0022 (bottom panel).

pect a mass of ∼8.4. This is yet another indication that the black hole mass of B2 0954+25A should be significantly smaller than $\log(M/M_\odot) = 9$.

Also, the SED of PMN J0948+0022 is very similar to that of B2 0954+25A (in the disk dominated state), the only difference being at γ–rays (where PMN J0948+0022 showed an exceptional flaring episode (Foschini et al., 2011)). This similarities support our speculation on the possible classification of B2 0954+25A as a γ–NLS1.

However, this similarity cannot be pushed too far, since B2 0954+25A lacks the strong iron emission that usually characterizes NLS1. Also, X–ray photon index of B2 0954+25A is $\Gamma = 1.74$ (§3.4.2), while that of NLS1 is typically $\Gamma > 2.5$ (Boller et al., 1996). However, it should be noted that also the other γ–NLS1 have a flat X–ray spectrum (Abdo et al., 2009b,c), because the (flat) emission from the jet dominates at X–rays.

3.4.3 The SMBH mass of B2 0954+25A

I considered several SMBH mass estimates for B2 0954+25A (Tab. 3.3) obtained with different methods and calibrations. For all estimates, except the last two, I used the SEV method (§2.6). The first two estimates are computed using the FWHM estimates (of the broad component and the whole profile respectively) of the Mg II emission line provided by S11, a continuum luminosity derived from SDSS photometry (when the source was in the disk dominated state) of $\log(\nu L_\nu/\mathrm{erg\ s^{-1}}) = 45.7$ and the calibrations given in Shen et al. (2011) and Vestergaard and Osmer (2009) respectively. The mass estimates are very similar, so I will refer to them as the Mg II virial mass estimates ($\log M/M_\odot \sim 9$).

The next two estimates are computed using the FWHM of the Hβ emission line fitted with a single Gaussian. Values for FWHM are provided by S11 and by our Model 1 respectively, the continuum luminosity is derived from SDSS photometry (disk dominated state): $\log(\nu L_\nu/\mathrm{erg\ s^{-1}}) = 45.3$, and the calibration are from Vestergaard and Peterson (2006, same as S11) and Bentz et al. (2009), respectively. This pair of mass estimates are also very similar, so I will refer to them as the single Hβ virial mass estimates ($\log M/M_\odot \sim 8.5$).

The next estimate is computed using the FWHM of the Hβ emission line from Model 2, neglecting the additional Hβ^* component, and the calibration by Bentz et al. (2009).

Finally, the last two rows of Tab. 3.3 report mass estimates obtained without using the SEV method. For the first one I used the width of the [O III] line (provided by Model 2 fitting) as a proxy for the stellar velocity dispersion σ_*, and the calibration of the M–σ relation given in Tremaine et al. (2002, their Eq. 20). Updated calibration given in Graham et al. (2011) produces the same result. In the last row I report the mass estimate obtained

Table 3.3: Black hole mass estimates using different methods and calibrations. Continuum luminosity at 3000Å and 5100Å (rest frame) used in virial estimates are $\log(\nu L_\nu/\mathrm{erg\ s^{-1}}) = 45.7$ and 45.3 for Mg II and Hβ respectively (derived from SDSS photometry). Col. [1]: method used; Col. [2]: reference for the FWHM of the emission line; Col. [3]: FWHM of the broad emission line; Col. [4]: black hole mass estimate; Col. [5]: Eddington ratio, assuming a bolometric luminosity $\log(L_{\rm bol}/\mathrm{erg\ s^{-1}}) = 45.95$; Col. [6]: calibration references: (a) Shen et al. (2011), (b) Vestergaard and Osmer (2009), (c) Vestergaard and Peterson (2006), (d) Bentz et al. (2009), (e) Tremaine et al. (2002).

Method [1]	FWHM ref. [2]	FWHM [km s^{-1}] [3]	log M/M$_\odot$ [4]	Edd. ratio [5]	Calib. ref. [6]
Virial, Mg II	S11, broad comp.	3980	9.0	0.1	(a)
	S11, whole profile	3390	8.8	0.1	(b)
Virial, Hβ, single comp.	S11	2970	8.6	0.2	(c)
	Model 1	2830	8.5	0.3	(d)
Virial, Hβ, Hβ^*	Model 2	1470	7.9	1.1	(d)
M-σ_* ([OIII])	Model 2	430	8.0	0.9	(e)
SED modeling	—	—	8.2	0.6	

through SED modeling (§3.4.2). Notice that the last three methods yield very similar results ($\log M/M_\odot \sim 8$), even if they have been derived using different and independent methods.

Our black hole mass estimates ranges from $10^8\ M_\odot$ to $10^9\ M_\odot$, while the mass reported in literature exceeds significantly $10^9\ M_\odot$ (§3.4). This is likely a consequence of the different adopted values of the Hβ line width. Also, the mass given in S11 is possibly overestimated since the continuum luminosity has been measured while the source was in the jet dominated state.

The mass estimate obtained with Model 2, the M–σ relation and the SED modeling procedure, although being independent methods, yields quite compatible results $\sim 10^8\ M_\odot$. Therefore they provide greater confidence about the reliability of the mass estimate. A SMBH mass smaller than 10^8 appears unlikely since the disk would become super–Eddington. Also, mass greater than $\sim 5 \times 10^8$ are unlikely because the disk model would no longer be compatible with observed data. Therefore I conclude that the black hole mass of B2 0954+25A is in the range $\log(M/M_\odot) = 8$–8.5.

3.4.4 The classification of B2 0954+25A

The FWHM of the whole Hβ profile is ~ 2800 km s^{-1}, hence it can not be classified as a genuine NLS1. However, as discussed in §3.4.1 the Hβ line

profile shows an asymmetric red wing. In order to bring the SEV mass estimates in agreement with two other independent methods (M–σ with [O III] as a proxy for σ_* and SED modeling) we need to consider only the symmetric core of the Hβ line. Hence, I speculate that the asymmetric red wing may be due to a non–virialized component. This issue may have important consequences on the classification of B2 0954+25A. Should the additional Hβ^* component vanish in future observations, the FWHM of the remaining (virialized), Hβ component would be $\sim$1500 km s^{-1}, and the source would become a powerful γ–NLS1 (Foschini et al., 2009a; Abdo et al., 2009c; Calderone et al., 2011). Such variations in line profiles have already been observed, on timescales of tens of years in NGC 5548 (Peterson, 1987).

As discussed in §3.4.2, B2 0954+25A is a typical *Fermi* blazar. However, the likely small black hole mass of B2 0954+25A and the SED resemblance with prototypical γ–NLS1 PMN J0948+0022 suggest some similarities between the two sources. B2 0954+25A does not meet the commonly adopted classification criterion for NLS1, namely a FWHM of broad Hβ $<$2000 km s^{-1} (Osterbrock and Pogge, 1985).[6] However, the physical nature of such empirical threshold has been often questioned (e.g. Goodrich, 1989; Véron-Cetty et al., 2001) since all observational properties show a continuous transition at FWHM(Hβ) $\sim$2000 km s^{-1}, i.e. properties of NLS1 and BLS1 sources are smoothly joined.

Alternative criteria to distinguish among BLS1 and NLS1 sources have been put forward. Sulentic et al. (2000) proposed to increase the dividing threshold to 4000 km s^{-1}, to select radio–quiet sources with low mass and high accretion rate. Véron-Cetty et al. (2001) suggested to consider the strength of Fe II emission relative to Hβ as a possible tracer of the Eddington ratio. Netzer and Trakhtenbrot (2007) proposed to classify as narrow–line AGN (NLAGN) all sources exceeding an Eddington ratio of 0.25 (regardless of black hole mass).

A small black hole mass is likely a characterizing property of NLS1 sources (Grupe and Mathur, 2004). I would like to stress that if asymmetry in broad Balmer line profiles are due to non-virialized components in the BLR, then only the virialized one should be considered to estimate the black hole mass, and thus the NLS1 classification. In this case B2 0954+25A would be classi-

[6] The further criterion on flux ratio [OIII]/Hβ $<$3 is almost always automatically satisfied when a broad Hβ component is detected (e.g. Zhou et al., 2006).

fied as a powerful γ–NLS1, just like PMN J0948+0022.

Since the overall properties of B2 0954+25A are similar to both classes of *Fermi* blazars and γ–NLS1, I conclude that it is one of those objects which smoothly joins the population of narrow–line and broad–line AGNs.

Chapter 4

SED of Type 1 AGN

4.1 Introduction

The Spectral Energy Distribution (SED) of Active Galactic Nuclei (AGN) spans several orders of magnitude in frequency and results from the superposition of radiation emitted by different components (Fig. 4.1).

In radio–quiet Type 1 sources, characterized by the presence of broad emission lines in their optical spectrum, the most luminous components are the "Big Blue Bump" (BBB, between $\sim$1 μm and $\sim$3 nm, or $\log(\nu/\mathrm{Hz})$ $\sim$14.5–17) and the "infrared bump" (IR bump, between $\sim$1 mm and $\sim$1 μm or $\log(\nu/\mathrm{Hz})$ $\sim$11.5–14.5). The former is the most prominent feature in the SED (Sanders et al., 1989; Elvis et al., 1994; Richards et al., 2006), while the latter accounts for 20–40% of the bolometric AGN luminosity (Chap. 5). The BBB is thought to be thermal radiation from the accretion disk, while the IR bump is thermal radiation emitted from a dusty torus located a $\sim$1 pc from the black hole (Sanders et al., 1989). Superimposed to the BBB there is often a minor component named "Small Blue Bump" (SBB, extending from 2200Å to 4000Å) which is likely the blending of several iron lines and hydrogen Balmer continuum (Wills et al., 1985; Vanden Berk et al., 2001). This scheme roughly describes the SED of AGN over at least 5 orders of magnitude in bolometric luminosity (Sanders et al., 1989; Elvis et al., 1994; Richards et al., 2006). It also applies to powerful blazars, although in these cases two more components are needed to describe the entire SED: the "synchrotron hump" (extending from radio to IR/optical wavelengths) and the "Compton hump" (extending from X–rays to TeV energies) which may overwhelm the

torus and the BBB radiation. These further components characterize radio–loud sources whose jet is closely aligned to the line of sight, and are due to the synchrotron and inverse Compton processes, respectively.

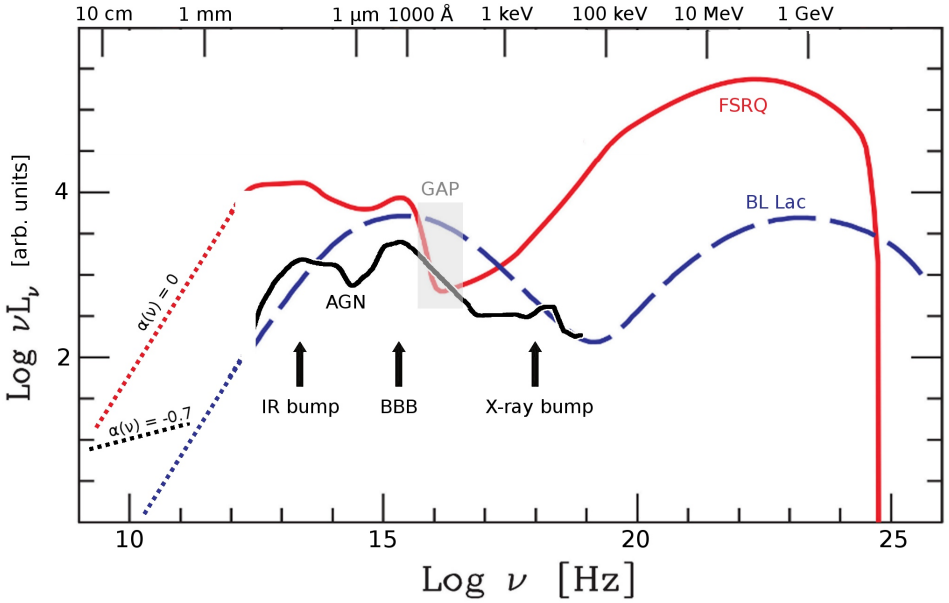

Fig. 4.1: Comparison of average SED of Type 1 AGN (black, Elvis et al. 1994), FSRQ (red) and BL Lac (blue, Ghisellini et al. 2010). The black arrows show the location of the IR bump, BBB and X–ray bump in Type 1 AGN. The dotted lines show the typical spectral slopes at radio wavelengths for blazars ($\alpha_\nu \sim 0$) and RL–AGN ($\alpha_\nu \sim -0.7$). The grey area show the frequency range inside which the absorption by neutral hydrogen in our Galaxy hampers our observation capabilities. This is the same figure as 1.7, we show it again for convenience.

4.2 A model for the central engine

The common energy production process in AGN is believed to be accretion onto a super–massive black hole ($M \sim 10^{6-10} M_\odot$, §1.4), through a disk whose observational properties depend (among other parameters) on the black hole mass and accretion rate. This interpretation led several authors to use the model of geometrically thin, optically thick accretion disk (Shakura and Sunyaev, 1973, hereafter AD model) to fit the optical/UV SED of AGN in order to determine the SMBH mass and the accretion rate (e.g. Shields, 1978; Malkan and Sargent, 1982; Malkan, 1983; Zheng et al., 1995; Sun and

Malkan, 1989). The AD fitting method allowed to estimate such quantities for those active nuclei which are too distant ($z \gtrsim 0.3$) or too bright for other direct methods, such as resolved stellar/gas dynamics, to be applied (Ferrarese and Ford, 2005). Furthermore, the AD model fitting may provide independent SMBH mass estimates to be compared to SEV method, in order to assess their reliability (§2.7, 3.2, 3.4.3).

However, as discussed extensively in Koratkar and Blaes (1999) and references therein, such simple models provide only rough fits to the observed data. Among the major issues with this interpretation, I point out a few ones: the broad–band continuum slopes α_ν (with $F_\nu \propto \nu^{\alpha_\nu}$) at optical–NUV wavelengths found in literature (e.g. Neugebauer et al., 1979; Vanden Berk et al., 2001; Davis et al., 2007; Bonning et al., 2007) are incompatible with the slope $\alpha_\nu = 1/3$, expected from the AD model; the spectrum from a simple accretion disk does not reproduce the observed power law extending at X–rays and the soft X–ray excess (e.g. Pounds et al., 1986; Nandra and Pounds, 1994; Fabian and Miniutti, 2005); the gross properties of the spectrum of radio–quiet AGN appear to scale with the luminosity (Sanders et al., 1989; Walter and Fink, 1993), but does not shift in frequency (Davis et al., 2007; Laor and Davis, 2011a). The latter issue indicates that the BBB spectrum peaks always at, or near, the same frequency. However, this observation is hard to reconcile with reasonably broad distributions of SMBH masses, accretion rates, inclinations and radiative efficiencies.

The non–perfect agreement between data and the predicted disk spectrum may be due to oversimplifications in the Shakura and Sunyaev (1973) model. More realistic disk models should account for the possible departure from black body emission in the innermost regions of the disk and for general relativity corrections. At radii where the temperature increases above $\sim 10^5$ K ($\sim$13.6 eV) the opacity becomes dominated by electron scattering, rather than free–free or bound–free absorption. The emitted spectrum is therefore a color temperature corrected black body with $T_{\rm col} = f_{\rm col} T(R)$ (Zhang et al., 1997). The correction factor depends on the maximum temperature of the disk and from the detailed disk structure. Recent calculations show that $f_{\rm col} \sim 2.5$ for disks with $T_{\rm max} \gtrsim 10^5$ K, and drops to $f_{\rm col} = 1$ for $T_{\rm max} \lesssim 10^4$ K, when the amount of free electrons is negligible (Done et al., 2012). The general relativistic corrections can be consistently treated as discussed in §6.2.3, as long as frequencies below the peak are concerned (in the νL_ν rep-

resentation). A more realistic model requires a self–consistent treatment of departures from thermodynamic equilibrium, Compton scattering and continuum opacities effects (Hubeny et al., 2001, and references therein). The resulting spectrum depends on the model parameters, e.g. the viscosity of the disk. However, the most significant departures from the standard Shakura and Sunyaev (1973) disk spectrum lie at frequencies close to and above the peak frequency (a region which is not critical for the analysis discussed in this work).

Given the difficulties in formulating a complete, self–consistent theory on the subject, the AD fitting method is not widely employed as a black hole mass estimation method. Rather, it is sometimes used to indirectly infer other parameters such as the accretion efficiency (Davis and Laor 2011; Laor and Davis 2011a, but see Raimundo et al. 2012) or to explain specific quasar properties (Laor and Davis, 2011b), while the SMBH mass is usually estimated using the SEV method §2.6 (Peterson, 1993; Peterson et al., 2004; Onken et al., 2004; Vestergaard and Peterson, 2006; Bentz et al., 2009).

In this chapter I will revisit the AD spectrum fitting method and show (§4.3) that the AD model provides a rather satisfactory description of the Type 1 AGN SED in the majority of cases (at least at optical/NUV wavelengths) once the contributions from other emitting components (such as host galaxy and/or jet) have been properly taken into account. Therefore, the AD modeling method is a viable and independent way to estimate SMBH masses. This is particularly interesting for a class of AGN sources for which black hole masses are suspected to be systematically underestimated by the SEV method: the Narrow Line Seyfert 1 (NLS1) galaxies (§2.7, 3.2, 3.4.3, Marconi et al. 2008; Decarli et al. 2008; Peterson 2011). In the following I will show that the broad–band composite SEDs of AGN are roughly compatible with a simple, non–relativistic AD model (§4.3). In §4.3.1 and 4.3.2 I will show that basic observational properties such as the continuum and emission line luminosities scale linearly with the disk luminosity. Furthermore, in Chap. 5 I will show that also the torus luminosity at IR wavelengths show a simple dependence on the disk luminosity, in well agreement with the overall picture that the accretion disk is actually the “prime mover” of the AGN phenomenon.

The observational properties of the Shakura and Sunyaev (1973) AD model, and their relationship with fundamental physical properties are dis-

cussed in §6.2. In §6.3 I will discuss a new method to estimate the SMBH mass and accretion rate, using AD spectrum modeling, and apply this method on a sample of 23 radio–loud NLS1 (§7.1). These results are discussed in Calderone et al. (2012b).

4.2.1 Notation

In what follows I will consider a non–relativistic,[1] steady state, geometrically thin, optically thick accretion disk (Shakura and Sunyaev, 1973), extending from $R_{\rm in} = 6R_{\rm g}$ to $R_{\rm out} = 2\times10^3 R_{\rm g}$, where $R_{\rm g} = GM/c^2$ is the gravitational radius of the black hole. The integrated disk luminosity is $L_{\rm d} = \int L_\nu d\nu = \eta\dot{M}c^2$, with $\eta \sim 0.1$ (radiative efficiency). The corresponding Eddington ratio is $\ell = L_{\rm d}/L_{\rm Edd}$ with $L_{\rm Edd} = 1.3\times10^{47}(M/10^9 M_\odot)$ erg s^{-1}.

The relation between the disk luminosity and its "isotropic equivalent" counterpart is $L_{\rm d}^{\rm iso} = \langle 2\cos\theta\rangle L_{\rm d}$ (Eq. 6.13), where θ is the angle between the normal to the disk and the line of sight. For Type 1 AGN I take $\langle 2\cos\theta\rangle = 1.7$ (Eq. 6.16).

I will refer to the peak frequency in the νL_ν representation as $\nu_{\rm p}$, and to the luminosity of the peak as $\nu_{\rm p}L_{\nu_{\rm p}}$. These quantities scale with the physical parameters as follows (Eq. 6.8 and 6.9):

$$\nu_{\rm p} \propto M^{-1/2}\dot{M}^{1/4}$$
$$\nu_{\rm p}L_{\nu_{\rm p}} \propto \dot{M}.$$

In particular notice that $\nu_{\rm p}L_{\nu_{\rm p}} \sim 0.5 L_{\rm d}$ (Eq. 6.10). The location of the peak (i.e. its luminosity and frequency) determines uniquely the black hole mass and accretion rate. Details about the observational properties of the AD spectrum are given in §6.2.

All spectral slopes α_ν are defined as $F_\nu \propto \nu^{\alpha_\nu}$.

4.3 Accretion disk spectrum in AGN spectra

Richards et al. (2006) built an average SED of Type 1 AGNs using data from 259 (mainly radio–quiet) sources, observed with instruments ranging from radio wavelengths to X–rays. Individual SEDs have been interpolated between available bands. An average SED is then computed as a geometric

[1] General relativistic correction are negligible for the purpose of our work, see §6.2.3

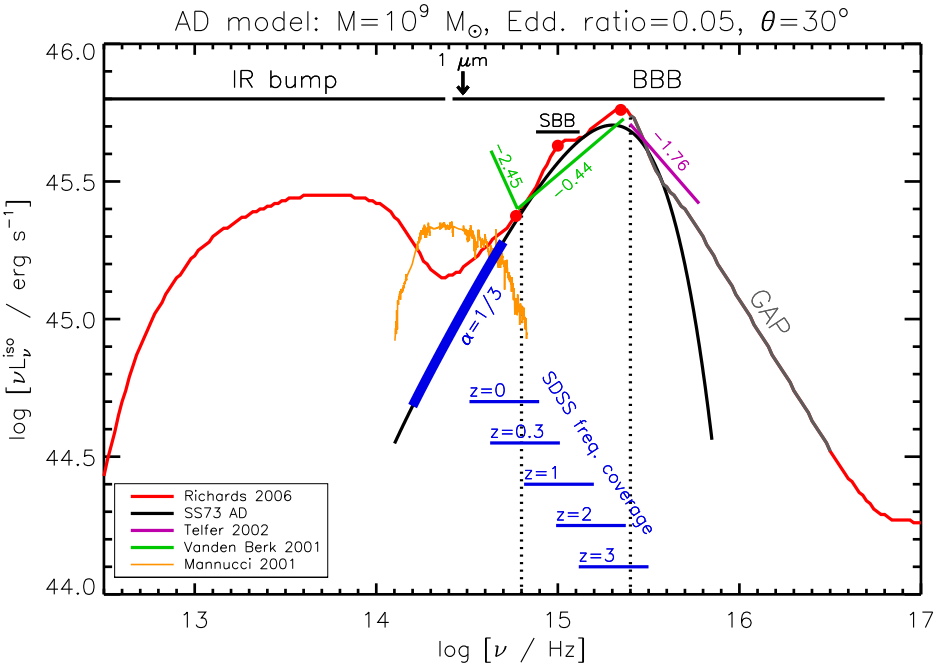

Fig. 4.2: Comparison of the composite Type 1 AGN SED (red line) from Richards et al. (2006) and an AD model with $\log(M/M_{\odot})$=9, ℓ=0.05 and $\theta = 30°$ (black line). Also shown are: a spiral galaxy template as given in Mannucci et al. (2001, orange), normalized to have a bolometric luminosity of $10^{45.5}$ erg s^{-1}; the location of the Small Blue Bump (SBB, Wills et al., 1985; Vanden Berk et al., 2001); three reference frequencies corresponding to 5100Å, 3000Å and 1350Å (red filled circles), commonly used in calculation of bolometric luminosity; the average spectral slopes found in literature, as measured on composite spectra at near IR, optical/UV (Vanden Berk et al., 2001, green) and far UV wavelengths (Telfer et al., 2002, purple); the rest frame frequency range covered by SDSS, for values of $z = 0$, 0.3, 1, 2 and 3 (thin blue lines). Thick blue line highlights the portion of the AD spectrum characterized by the slope $\alpha_{\nu} = 1/3$. The rest frame frequency range inside which the AD model reproduces the shape of the AGN composite SED ($\log(\nu/\mathrm{Hz})$ = 14.8–15.5) is shown with dotted black lines.

mean of individual ones, and is shown in Fig. 4.2, (red line). Also shown in Fig. 4.2 are: a spiral galaxy template as given in Mannucci et al. (2001, orange), normalized to have a bolometric luminosity of $10^{45.5}$ erg s^{-1}; the location of the Small Blue Bump (SBB, Wills et al., 1985; Vanden Berk et al., 2001); three reference frequencies corresponding to 5100Å, 3000Å and 1350Å (red filled circles), commonly used in calculation of bolometric luminosity (§4.3.1); the average spectral slopes found in literature, as mea-

sured on composite spectra at near IR, optical/UV (Vanden Berk et al., 2001, green) and far UV wavelengths (Telfer et al., 2002, purple); the rest frame frequency range covered by SDSS, for values of $z = 0$, 0.3, 1, 2 and 3 (thin blue lines). Finally, I show the AD spectrum that best fits the composite Type 1 SED at optical/UV wavelengths (black line). The parameter for the AD model are: $\log(M/M_{\odot})$=9, ℓ=0.05 and $\theta = 30°$.

The agreement between the AD model and the composite SED is rather good, therefore the association between the BBB and thermal emission from simple AD model is justified, at least in the interval 1000–5000Å, or $\log(\nu/\mathrm{Hz})$ = 14.8–15.5 (black dotted vertical lines). A few discrepancies between the AD model and the composite Type 1 SED arise:

- at $\log(\nu/\mathrm{Hz})$ <14.7 a further component emerges in the spectrum, which may be either the host galaxy, the emission from a dusty torus or some other component;
- at $\log(\nu/\mathrm{Hz})$ ∼15 a Small Blue Bump (SBB) is present, likely due to a blending of iron lines and Hydrogen Balmer continuum;
- at $\log(\nu/\mathrm{Hz})$ $\gtrsim$15.6 other physical components contribute to the flux (e.g. a corona).

Note that, in this interpretation of the BBB, the portion of the AD spectrum characterized by the $\alpha_{\nu} = 1/3$ slope (thick blue line) is hidden by the host galaxy and the torus components, and cannot be revealed directly with observations (although in some case it may be detected in polarized light, Kishimoto et al. 2008). The average slopes at optical/UV and far UV (green and purple lines) are roughly consistent with the slopes near the peak of the AD spectrum. Notice however that fixed spectral features (such as the SBB) may affect the estimation of spectral slopes. Furthermore, the value of the slope likely depends on the width of the wavelength range inside which it is defined. Therefore it is not always possible to infer the presence of an AD spectrum by just checking the spectral slopes at optical/UV wavelengths. By contrast, at near IR the average slope (green line) is inconsistent with an AD spectrum, but this is likely due to the host galaxy component.

I conclude that the AD model provides a reasonable description of the gross properties of Type 1 AGN SED at optical/NUV wavelengths, and the similarity between the predicted spectrum and the average BBB is rather

strong. Under this assumption it is possible to infer the SMBH mass and the accretion rate by comparing the observed SED with the AD spectrum, as discussed in §6.3.

Our SMBH mass estimation method requires an estimate of the disk luminosity ($L_{\rm d}$). In the following I will discuss two method to estimate $L_{\rm d}$, relying on the continuum and emission line luminosity respectively.

4.3.1 Continuum luminosity as a proxy to disk luminosity

The broad–band similarity among AGN spectra allows to use the continuum luminosity at a given wavelength as a proxy for the bolometric luminosity, that is $L_{\rm bol} = {\rm C}_{\rm bol} \times \lambda L_{\lambda}$. In order to explore this relationship Richards et al. (2006) measured the bolometric luminosity for each spectrum (defined to be the integral isotropic luminosity between 100μm and 10 keV) and derived a bolometric correction (C$_{\rm bol}$) based on the continuum luminosity at 3000Å, 5100Å and 3μm. The resulting values are: ${\rm C}_{\rm bol}(3000\text{Å}) = 5.62 \pm 1.14$, ${\rm C}_{\rm bol}(5100\text{Å}) = 10.33 \pm 2.08$, ${\rm C}_{\rm bol}(3\mu{\rm m}) = 9.12 \pm 2.62$. The distribution of C$_{\rm bol}$ values is relatively narrow, with a relative dispersion of the order of ∼20%. Note however, that in particular cases the C$_{\rm bol}$ value can differ by as much as 50% from the mean value. Shen et al. (2011) have slightly re–calibrated the C$_{\rm bol}$ values, and extended the analysis to 1350Å, in order to compute bolometric luminosities for all the sources in their sample. Their values are: ${\rm C}_{\rm bol}(5100\text{Å}) = 9.26$, ${\rm C}_{\rm bol}(3000\text{Å}) = 5.15$ and ${\rm C}_{\rm bol}(1350\text{Å}) = 3.81$.

In order to calibrate analogous relations to estimate the disk luminosity $L_{\rm d}^{\rm iso}$ I numerically estimate the bolometric luminosity of the composite SED in Richards et al. (2006), and compare it with the disk luminosity for the AD model shown in Fig. 4.2. The resulting relation is:

$$L_{\rm d}^{\rm iso} \sim \frac{1}{2} L_{\rm bol} \tag{4.1}$$

Then, I compare $L_{\rm d}^{\rm iso}$ with the luminosities at 5100Å, 3000Å and 1350Å wavelengths, as measured on the composite SED:

$$\begin{aligned} L_{\rm d}^{\rm iso} &\sim 4.4\ \nu L_{\nu}(5100\text{Å}) \\ L_{\rm d}^{\rm iso} &\sim 2.4\ \nu L_{\nu}(3000\text{Å}) \\ L_{\rm d}^{\rm iso} &\sim 1.8\ \nu L_{\nu}(1350\text{Å}) \end{aligned} \tag{4.2}$$

The locations of these wavelengths are shown with red filled circles in Fig. 4.2. Considering the uncertainties ($\sim$20%) of $C_{\rm bol}$ I conclude that our relations (Eq. 4.1 and 4.2) are compatible with those of S11. Eq. 4.2 provides a reliable estimate of $L_{\rm d}^{\rm iso}$ as long as the source continuum is not dominated by other emitting components such as host galaxy starlight or synchrotron radiation from a relativistic jet (for radio–loud sources). In these cases we need alternative luminosity estimators, as discussed in the following section.

4.3.2 Line luminosities as a proxy to disk luminosity

Relations similar to Eq. 4.2 can be obtained by using line luminosities. Line ratios are known to be approximately constant among AGN (Francis et al., 1991; Vanden Berk et al., 2001): by setting the Lyα luminosity to 100, relative luminosities of Hβ, Mg II and C IV (both narrow and broad components) lines are 22, 34 and 63, respectively, while the total line luminosity is 555.8 (Francis et al., 1991; Celotti et al., 1997). Therefore it is possible to have a rough estimate of the luminosity of all emission lines by measuring the luminosity of a single line. Also, according to the photo–ionization model, the line–emitting gas is ionized by the accretion disk continuum radiation. Therefore I expect (to a first approximation) the disk to line luminosity ratio to be a constant: $L_{\rm d}^{\rm iso} = \kappa\, L_{\rm line}$. This provides a way to estimate the disk luminosity using a single (or a few) line luminosity estimates. In order to calibrate the κ parameter I consider all sources in the S11 catalog having both a continuum and line luminosity estimate for at least one of the combinations: 5100Å–Hβ, 3000Å–Mg II and 1350Å–C IV. The number of sources in each subsample are 22644, 85514 and 52157 respectively (note that a single source typically belongs to two such subsamples). For each source I estimate $L_{\rm line}$ using the broad and narrow line luminosities given in S11 and the coefficients given in Francis et al. (1991) and Celotti et al. (1997). Then I compute the κ parameter as follows:

$$\kappa = \frac{L_{\rm d}^{\rm iso}({\rm Eq.4.2})}{L_{\rm line}} \tag{4.3}$$

where the disk luminosity $L_{\rm d}^{\rm iso}$ is computed using the continuum luminosity given in S11, and Eq. 4.2. The distributions of κ for the three combinations

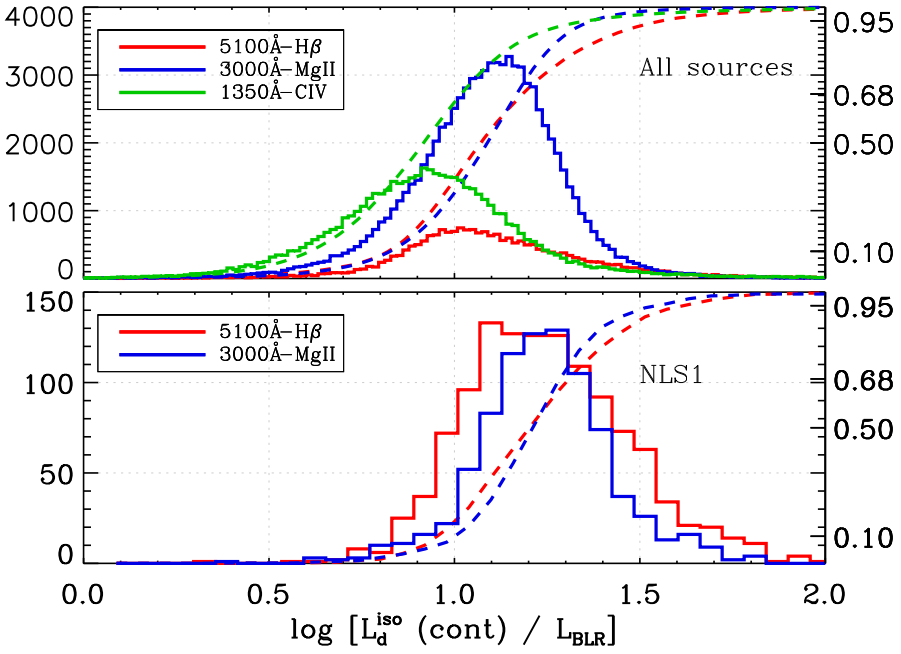

Fig. 4.3: Upper panel: distribution of the κ parameter (Eq. 4.3) for the three combinations 5100Å–Hβ, 3000Å–Mg II and 1350Å–C IV. Both the continuum and line luminosity estimates are those reported in the S11 catalog. The number of sources in each subsample are 22644, 85514 and 52157 respectively (note that a single source typically belongs to two such subsample). Lower panel: the same as upper panel, for the subsample of Narrow–Line Seyfert 1 sources common to both the S11 and Zhou et al. (2006) catalog.

are approximately log–normal (Fig. 4.3, upper panel) with median values:

$$\begin{aligned} \log\kappa(5100\text{Å} - \text{H}\beta) &= 1.08 \pm 0.28 \\ \log\kappa(3000\text{Å} - \text{Mg II}) &= 1.10 \pm 0.21 \\ \log\kappa(1350\text{Å} - \text{C IV}) &= 0.92 \pm 0.28 \end{aligned} \tag{4.4}$$

The widths of the κ distributions in Fig. 4.3 show that the disk luminosity $L_{\rm d}^{\rm iso}$ computed using the continuum and the line intensities differs by $\lesssim$0.3 dex, i.e. a factor $\lesssim$2. Hence, the relationships between continuum and line luminosities seem quite robust. A possible explanation for the larger dispersion in the 5100Å–Hβ case, with respect to the 3000Å–Mg II one, may be that the continuum luminosity at 5100Å is contaminated by the host galaxy.

Both the continuum and the line luminosities in S11 are affected by uncertainties, therefore the distributions shown in Fig. 4.3 are likely broad-

ened by measurement errors. Thus, the intrinsic dispersion is expected to be smaller than 0.3 dex (a factor of ∼2) for Hβ and C IV, and 0.2 dex (a factor of ∼1.6) for Mg II. This is yet another evidence that SEDs in most AGN show some degree of universality: the constancy of the continuum to line luminosity ratio at optical wavelengths implies a constant optical continuum to ionizing UV luminosity ratio.

Since the samples in the S11 catalog are dominated by radio–quiet sources (the great majority are undetected in the FIRST survey), I repeat the analysis on radio–loud sources, i.e. those sources for which the radio–loudness parameter[2] is greater than 100. Interestingly, the κ parameters for the radio–loud sub–sample of S11 differ by at most ∼5% from the values quoted above.

By using the values given in Eq. 4.4 and the coefficients to compute the line luminosity $L_{\rm line}$ discussed above, we are able to estimate the total disk luminosity as follows:

$$\begin{aligned} L_{\rm d}^{\rm iso} &= 12\, L({\rm H}\beta)\, \frac{555.8}{22} = 303\, L({\rm H}\beta) \\ L_{\rm d}^{\rm iso} &= 12.5\, L({\rm Mg\,II})\, \frac{555.8}{34} = 204\, L({\rm Mg\,II}) \\ L_{\rm d}^{\rm iso} &= 8.4\, L({\rm C\,IV})\, \frac{555.8}{63} = 74.1\, L({\rm C\,IV}). \end{aligned} \tag{4.5}$$

I repeat the above analysis on the subsample of NLS1 sources, that are the focus of our study. In particular, I consider the sources common to both the Zhou et al. (2006) and the S11 catalog (1210 sources). The distributions[3] of the κ parameter are still log–normal, and are shown in the lower panel of Fig. 4.3. Median values are now ∼0.15 dex (i.e. a factor ∼1.4) greater:

$$\begin{aligned} \log \kappa(5100{\rm \AA} - {\rm H}\beta) &= 1.23 \pm 0.23 \\ \log \kappa(3000{\rm \AA} - {\rm Mg\,II}) &= 1.24 \pm 0.21. \end{aligned} \tag{4.6}$$

The uncertainties are of the same order of magnitude. The class of NLS1 sources is therefore characterized by both a smaller width and a smaller

[2]The radio–loudness parameter provides an indication of whether the AGN SED is dominated by radiation at radio frequencies or optical band. Historically, it is defined as the ratio of 5 GHz to optical B–band luminosity (Kellermann et al., 1989). The values used here are those given in S11, defined as the ratio of flux densities at 6 cm and 2500Å (rest frame).

[3]The 1350Å–C IV case is missing since the SDSS wavelength coverage does not allow to observe both the C IV line and the Hβ line (required to classify the source as a NLS1).

luminosity of lines. The resulting disk luminosities are:

$$\begin{aligned} L_{\rm d}^{\rm iso} &= 424\, L(\mathrm{H}\beta) \\ L_{\rm d}^{\rm iso} &= 286\, L(\mathrm{Mg\,II}). \end{aligned} \tag{4.7}$$

In order to estimate the accretion disk luminosity using a single spectrum we can use either Eq. 4.2 (whose uncertainties are $\sim$20%) or Eq. 4.7 (whose uncertainties are a factor $\sim$2). In cases where the observed continuum radiation is dominated by components other than AD, e.g. synchrotron emission from the jet or host galaxy starlight, Eq. 4.2 would overestimate the disk luminosity. Therefore Eq. 4.7 is our preferred choice to estimate $L_{\rm d}^{\rm iso}$.

Chapter 5

The disk–torus connection

5.1 Introduction

The simplest version of the unification model (§1.3) predicts the presence of a dusty "torus" surrounding the central regions of the Active Galactic Nucleus (AGN) intercepting a fraction of the illuminating accretion disc radiation and re–emitting it in the infrared (Chap. 1). If the absorption is due to dust, there is a natural temperature scale in the system, since dust sublimates for temperatures greater than ~ 1500 K, corresponding to a peak in the corresponding black body spectrum at $\nu_{\rm p} = 3.93\ kT/h \sim 1.2 \times 10^{14}$ Hz (or $\lambda_{\rm p} \sim 2\mu$m; the 3.93 factor is appropriate for the peak in the νL_ν spectrum). Along the years, the idea of a simple and uniform "doughnut" around the accretion disc has been replaced by a clumped material, possibly outflowing (or inflowing), as envisaged and modeled by many authors (see e.g. Elvis 2000; Risaliti et al. 2002; Elitzur and Shlosman 2006; Nenkova et al. 2008.

According to the picture outlined in Chap. 4 the torus is expected to re–process a given amount of radiation from the accretion disk, i.e. we expect to find a disk–torus connection. In order to study this correlation we need to collect the largest group of radio–quiet AGN with reliable detections of the IR luminosity and an optical spectrum to characterize the accretion disc features. The Sloan Digital Sky Survey (SDSS; York et al. 2000) and the Wide–field Infrared Survey Explorer (WISE; Wright et al. 2010) are the catalogs with the widest number of objects in these two bands, hence they are the most appropriate for our study. WISE provided photometric observations in 4 IR

bands (3.4, 4.6, 12 and 22 μm) for half a billion sources (all sky) with fluxes larger than 0.08, 0.11, 1 and 6 mJy in unconfused regions on the ecliptic in the four bands.

The covering factor of the torus is not well known. Estimates come from direct observations of optical and IR AGN, as well from statistical considerations concerning the number of type 1 and type 2 AGN. In the first case, the studies were hampered up to now by the relatively small samples of objects (especially in the IR) suitable for a combined study (see e.g. Landt et al. 2011) for a sample of 23 objects observed spectroscopically in the optical and in the IR, down to $\sim 3\mu$m).

In this chapter I will explore the disk–torus connection and discuss a new way to estimate the torus covering factor, by appropriately taking geometrical effects into account (Calderone et al., 2012c).

5.2 Sample selection

I consider the Shen et al. (2011) (S11) catalog which provides several spectral properties for a sample of 105,783 magnitude smaller than $M_{i'\,\mathrm{band}} = -22$ (i.e. $\nu L_\nu(5100\text{Å}) \sim 10^{44}$erg s^{-1}), at least an emission line with FWHM > 1000 km s^{-1} and a reliable spectroscopical redshift. I will use the 3000Å continuum luminosity to estimate the bolometric luminosity of the sources, according to Eq. 4.2, 4.1. In the following I will assume that the bolometric luminosity equals the luminosity of the central engine, namely accretion disk and X–ray emitting corona. The superscript "iso" reminds that they are derived under the assumption of isotropic emission.

I require that all sources lie68 in a relatively narrow redshift range $0.56 < z < 0.73$[1] The S11 catalog has also been cross–correlated with the Faint Images of the Radio Sky at Twenty–centimeter survey (FIRST; Becker et al. 1995) and hence S11 include in their sample the radio fluxes. The flux limit of the FIRST sample is $\sim$1 mJy at 1.4 GHz. Therefore, I can select the radio–quiet quasars as those objects observed by the FIRST without a detectable radio flux. The radio–quiet requirement ensures the absence of a contamination from the jet in the wavelength intervals of interest. After the radio–quietness and the redshift selections, we are left with 5122 sources.

[1]The redshift range is a consequence of the original selection criteria in Calderone et al. (2012c), which required both the Hβ and Mg II lines to be observed in the SDSS spectrum.

I have cross–correlated this sample with the WISE All–Sky source catalog requiring that the optical and IR positions are closer than 2 arcsec (5082 sources), and selecting only those objects with detections in all the four WISE IR–bands, to have the most complete IR luminosity information. This last selection leaves us with a sample of 3965 WISE–detected, radio–quiet type 1 AGN in a redshift range z=0.56–0.73.

5.3 Data analysis and results

For all the 3965 sources in our sample I computed the IR flux in the four WISE bands by first transforming the observed (Vega) magnitudes in the AB systems setting $m_{\rm AB} = m + \Delta m$, with Δm given in Tab. 5.1. In the AB system, the flux–magnitude relation is simply:

$$\log F = -\frac{m_{\rm AB} + 48.6}{2.5} \tag{5.1}$$

where the flux density is measured in erg s^{-1} cm^{-2} Hz^{-1}. The integrated IR luminosity is computed by assuming a power law spectrum between two contiguous bands, and summing the contributions in all the three intervals. The slopes of the power laws are given by:

$$\alpha_{\rm i+1,i} = \frac{m_{\rm AB,i} - m_{\rm AB,i+1}}{2.5 \log(\lambda_{\rm i+1}/\lambda_{\rm i})} \tag{5.2}$$

The integrated luminosity in each interval is:

$$L_{\rm i+1,i} = \frac{\nu_{\rm i} L_{\nu_{\rm i}}}{1 - \alpha_{\rm i,i+1}} \left[1 - (\nu_{\rm i+1}/\nu_{\rm i})^{1-\alpha_{\rm i,i+1}}\right] \tag{5.3}$$

Table 5.1: Center wavelengths and frequencies of the four WISE bands, and value of Δm needed to transform the magnitudes given in the Vega system to the AB one. See Cutri et al. (2012) in http://wise2.ipac.scaltech.edu/docs/release/allsky.

band	λ [μm]	log Freq. [Hz]	Δm
1	3.435	13.94	2.699
2	4.6	13.81	3.339
3	11.56	13.41	5.174
4	22.08	13.13	6.620

Table 5.2: Mean and standard deviation of IR luminosities and spectral slopes in the four WISE bands for the whole sample, and the three subsample described in §5.3. Luminosities are in units of erg s^{-1}.

	Band	$\log \nu L_\nu$	α
Whole	1	44.87±0.26	1.3±0.5
sample	2	44.92±0.29	0.9±0.3
	3	44.87±0.29	1.4±0.5
	4	44.99±0.27	–
Sub A	1	44.88±0.20	1.2±0.4
	2	44.74±0.17	0.9±0.3
	3	44.77±0.15	1.5±0.4
	4	44.74±0.15	–
Sub B	1	45.01±0.20	1.4±0.4
	2	44.91±0.19	0.9±0.2
	3	44.96±0.16	1.4±0.4
	4	44.91±0.15	–
Sub C	1	45.15±0.22	1.6±0.3
	2	45.09±0.17	0.8±0.2
	3	45.16±0.15	1.2±0.4
	4	45.09±0.13	–

Finally, the integrated luminosity is $L_{\rm IR}^{\rm iso} = L_{2,1} + L_{3,2} + L_{4,3}$. As discussed in §5.2 the bolometric luminosity is computed using the continuum luminosity at 3000Å and to Eq. 4.2, 4.1. Again, the "iso" superscript reminds that these quantities are computed assuming isotropic emission.

The ratio $R = L_{\rm IR}^{\rm iso}/L_{\rm bol}^{\rm iso}$ is approximately constant (~ 0.3, Tab. 5.3) and will be used in §5.4 to estimate the torus covering factor. The bolometric and IR luminosities of all sources show a well defined correlation over at least 1.5 dex, as shown in Fig. 5.1. I performed two least squares fits by taking at first $x = \log L_{\rm bol}^{\rm iso}$ and $y = \log L_{\rm IR}^{\rm iso}$, then inverting the variables. I took the bisector as the best description of the correlation: $\log L_{\rm IR}^{\rm iso} \propto 0.83 \log L_{\rm bol}^{\rm iso}$. The slope, being smaller than one, suggests that IR luminosities become smaller at larger optical luminosity (receding torus). Similar results have been found using independent methods by e.g. Arshakian 2005; Simpson 2005).

To provide a deeper insight on the disc–torus connection I select three subsamples according to $L_{\rm bol}^{\rm iso}$; I will refer to these subsamples with letters A, B, C. Tab. 5.2 lists the νL_ν IR luminosities in the four WISE bands for

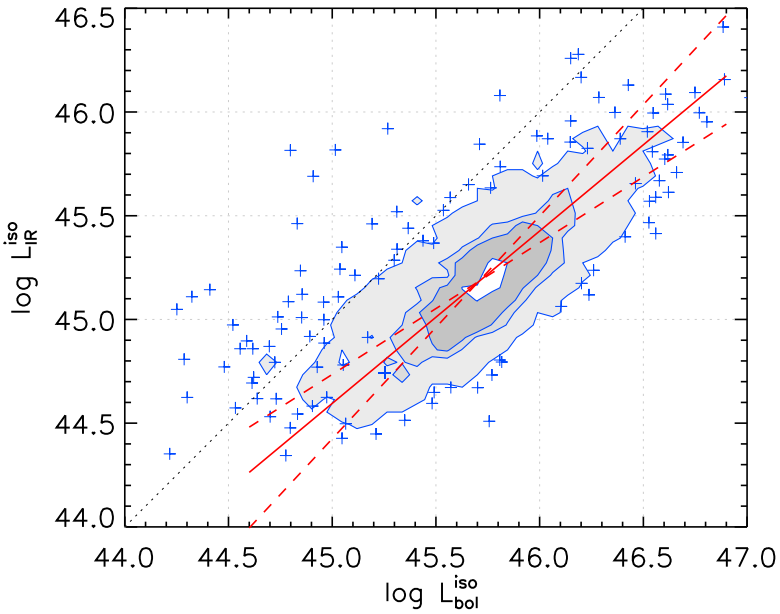

Fig. 5.1: Comparison of bolometric luminosity $L_{\rm bol}^{\rm iso}$ and integrated IR luminosity $L_{\rm IR}^{\rm iso}$ as measured by WISE. Contour levels are at 10%, 50%, 68% and 95% of total source number (3965). The dotted line identifies equal luminosity. The solid line ($\log L_{\rm IR}^{\rm iso} \propto 0.83 \log L_{\rm bol}^{\rm iso}$) is the bisector of the two least squares fitting (dashed) lines.

the whole sample and for the subsamples A, B, C, together with the average spectral indices. Tab. 5.3 reports the average and the standard deviation of $L_{\rm bol}^{\rm iso}$ and $L_{\rm IR}^{\rm iso}$ together with their ratio $R = L_{\rm IR}^{\rm iso}/L_{\rm bol}^{\rm iso}$ for the whole sample and for the A, B, C subsamples. For the latter, instead of the standard deviation of $L_{\rm bol}^{\rm iso}$, I give the logarithmic width of the considered luminosity bin. Note that sources in these subsamples account for only $\sim$1/3 of the entire sample. Dropping 2/3 of the sample was necessary to significantly separate the bolometric luminosity classes.

Table 5.3: Results of our analysis. Columns are: (1) sample; (2) number of sources in the sample; (3) mean bolometric luminosity in the sample; (4) width of luminosity bin ([a]: value in the first row is the standard deviation); (5) mean and standard deviation of $L_{\rm IR}^{\rm iso}$ in the sample; (6) mean and standard deviation of parameter $R = L_{\rm IR}^{\rm iso}/L_{\rm bol}^{\rm iso}$; (7) range of covering factor (Eq. 5.9); (8) range of torus opening angles; (9) range of Type 2 to Type 1 AGN count ratio (#2/#1). All means and standard deviations are computed using logarithmic values.

Sample	N src.	log $L_{\rm bol}^{\rm iso}$	log $\Delta L_{\rm bol}^{\rm iso}$	log $L_{\rm IR}^{\rm iso}$	R	Cov. factor	$\theta_{\rm T}$	#2/#1
Whole	3965	45.72	0.33[a]	45.18±0.27	$0.29^{+0.18}_{-0.11}$	0.54–0.70	57–46	1.2–2.3
A	408	45.55	0.10	45.05±0.16	$0.31^{+0.14}_{-0.10}$	0.56–0.74	56–42	1.3–2.8
B	569	45.80	0.10	45.22±0.16	$0.26^{+0.12}_{-0.08}$	0.51–0.66	59–49	1.0–1.9
C	389	46.05	0.14	45.40±0.16	$0.22^{+0.10}_{-0.07}$	0.47–0.60	62–53	0.9–1.5

5.4 The covering factor of the torus

Consider the simplest case of a doughnut–shaped torus with opening angle $\theta_{\rm T}$, as measured from the symmetry axis. The covering factor c is defined as:

$$c = \frac{\Omega_{\rm T}}{4\pi} = \frac{2 \times 2\pi \int_{\theta_{\rm T}}^{\pi/2} \sin\theta d\theta}{4\pi} = \cos\theta_{\rm T} \tag{5.4}$$

We must relate c to the observed ratio R, accounting for the anisotropy of disc and torus emission. Since the emission of geometrically thin discs follows a $\cos\theta$ pattern, for a given viewing angle $\theta_{\rm v}$ (calculated from the disc axis) the ratio between the real disc luminosity $L_{\rm bol}$ and the isotropic estimate $L_{\rm bol}^{\rm iso}$ is:

$$\frac{L_{\rm bol}}{L_{\rm bol}^{\rm iso}} = \frac{2 \times 2\pi \int_{0}^{\pi/2} \cos\theta \sin\theta d\theta}{4\pi \cos\theta_{\rm v}} = \frac{1}{2\cos\theta_{\rm v}} \tag{5.5}$$

The ratio is smaller than unity for $\theta_{\rm v} < 60^\circ$, thus for Type 1 AGN we likely have $L_{\rm bol} < L_{\rm bol}^{\rm iso}$. We are not able to determine $\cos\theta_{\rm v}$ for each source, but we can safely assert that $0 \leq \theta_{\rm v} \leq \theta_{\rm T}$, since we are dealing with Type 1 AGN. Therefore a reasonable estimate is:

$$\cos\theta_{\rm v} \sim \langle\cos\theta\rangle_{0-\theta_{\rm T}} = \frac{\int_0^{\theta_{\rm T}} \cos\theta \sin\theta d\theta}{\int_0^{\theta_{\rm T}} \sin\theta d\theta} = \frac{1+\cos\theta_{\rm T}}{2} \tag{5.6}$$

A relation similar to Eq. 5.5 for the torus luminosity ($L_{\rm T} = L_{\rm IR}$) is currently unknown. However, we can reasonably state that

$$\frac{L_{\rm bol}}{L_{\rm bol}^{\rm iso}} < \frac{L_{\rm T}}{L_{\rm T}^{\rm iso}} < 1 \tag{5.7}$$

The lower limit corresponds to a thin disc–shaped emitting torus, the upper limit to an isotropic emitting torus. Both limits are rather unrealistic: the torus is expected to show a lower degree of anisotropy than the disc since we are able to detect radiation emitted from the side (i.e. Type 2 AGN); also, the torus is hardly an isotropic emitter since IR signatures are different in Type 1 and 2 AGN (Calderone et al., in prep.). The above limits should then bracket the real case. The amount of disc radiation intercepted (and re–processed) by the torus is:

$$\frac{L_{\rm T}}{L_{\rm bol}} = \frac{\int_{\theta_{\rm T}}^{\pi/2} \cos\theta \sin\theta d\theta}{\int_{0}^{\pi/2} \cos\theta \sin\theta d\theta} = \cos^2\theta_{\rm T} \tag{5.8}$$

Rearranging the previous equations, we find a relation between the observable parameter $R = L_{\rm IR}^{\rm iso}/L_{\rm bol}^{\rm iso}$ and the covering factor c:

$$\frac{c^2}{1+c} < R < c^2 \tag{5.9}$$

This relation can be inverted to find the allowed range of c and $\theta_{\rm T}$, given a value of the observable parameter R (Fig. 5.2). Finally, the covering factor c can be used to estimate the count ratio between Type 1 and Type 2 AGN:

$$c = \frac{\Omega_{\rm T}}{4\pi} = \frac{\#2}{\#1 + \#2} \quad \Rightarrow \quad \frac{\#2}{\#1} = \frac{c}{1-c} \tag{5.10}$$

The last three columns of Tab. 5.3 report the value of c, $\theta_{\rm T}$ and #2/#1 corresponding to the observed values of R in all discussed samples.

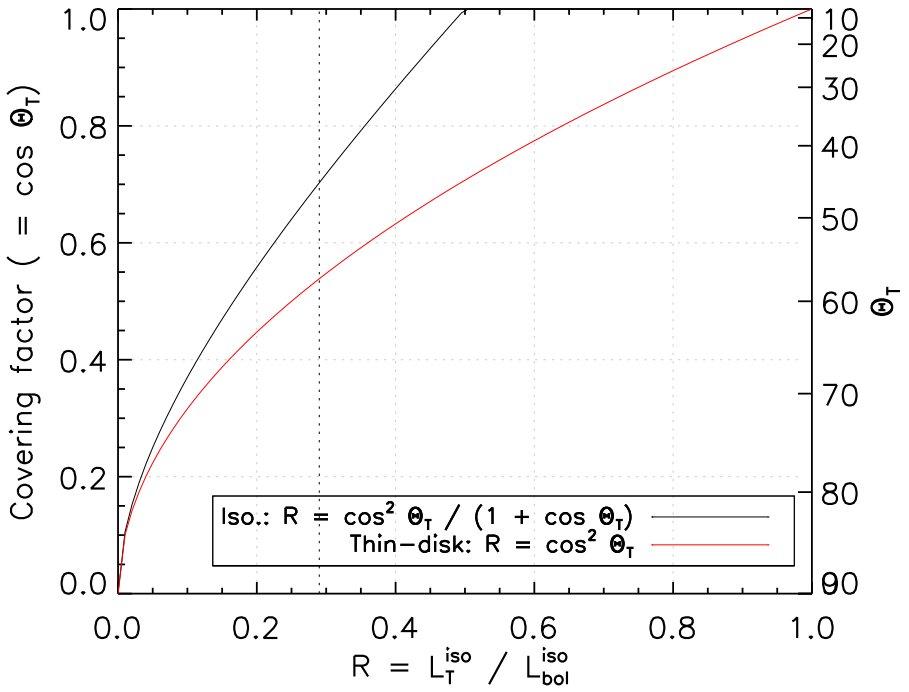

Fig. 5.2: Torus covering factor ($c = \cos\theta_{\rm T}$, left axis) and torus opening angle ($\theta_{\rm T}$, right axis) as a function of the R parameter for the two cases of isotropic and thin disc–shaped emitting torus(Eq. 5.9).

5.5 Discussion

The disk–torus connection, i.e. the fact that the torus and disk luminosities are related, is shown in Fig. 5.1. By adopting the approach described in §5.5 we were also able to estimate the average covering factor of the torus using a very large data set. The *observed* fraction of IR to bolometric, isotropically equivalent optical luminosity is about 30%. This implies that the obscuring torus covering factor is in the range 0.5–0.7 and that the opening angle $\theta_{\rm T}$ is 40°– 60°. On average, our sources emit in the IR a similar fraction of their bolometric luminosities ($\sim 1/3$). For each Type 1 AGN, there should be between 1 and 3 Type 2 sources. If there is a broad distribution of covering factors (as suggested by Elitzur 2012) our Type 1 sample may be drawn preferentially from the lower end of the distribution. In this case our estimate of #2/#1 ratio is a lower limit. The very basic prediction of the unified model that the torus re–processes a given amount of disc luminosity is verified (Fig. 5.1). The dispersion of this fraction is remarkably small, being at most a factor of 2. The broad–band spectral energy distribution (SED) from IR to

near–UV are expected to be quite similar among Type 1 AGN. A hint of the "receding torus" hypothesis is found in Fig. 5.1, with $\log L_{\rm IR}^{\rm iso} \propto 0.83 \log L_{\rm bol}^{\rm iso}$. In Fig. 5.3 I show both data and model for a prototypical broad–band SED, in the three luminosity classes considered above (coded with colors). For each subsample I also compute a composite spectrum using SDSS spectra.

At IR wavelengths the torus emission dominates. Spectral indices between the four WISE bands are very similar for different overall luminosities (Tab. 5.2). Despite the rather poor coverage, it appears that the IR emission is structured with at least two broad bumps. Such features are easily modeled by the superposition of two black bodies with temperatures of $\sim$300 K and $\sim$1500 K respectively. A naïve interpretation is to consider the hotter one as emitted from the hot part of the torus facing the disc, at the dust sublimation temperature. The colder one would come from the cooler outer side of the torus. This should be the region visible also in Type 2 AGN.

The underlying optical continua are well described by a standard (Shakura and Sunyaev, 1973) accretion disc spectrum. The dashed lines in Fig. 5.3 are the models of three accretion discs having the same bolometric luminosity as the spectra in the subsample, and masses 1.7×10^8, 2.3×10^8 and 3.4×10^8 $M_\odot$ respectively, grossly in agreement with the SEV masses calculated in S11. The WISE data points (in νL_ν) lie a factor $\sim$3 below the disc peaks (at $\log(\nu/\mathrm{Hz}) \sim 15.5$). This factor corresponds to the value $\sim$1/3 found in Tab. 5.3. The composite spectra follow closely the accretion disc continuum in all but the lowest luminosity subsample, in which some other component is present at frequencies below $\log(\nu/\mathrm{Hz}) < 14.9$. This further component may be the starlight contribution from host galaxy (Vanden Berk et al., 2001), as shown by the yellow line which is the sum of the accretion disc spectrum and an appropriately scaled template for an elliptical (quiescent) galaxy from Mannucci et al. (2001). At higher luminosity subsamples, the contribution from galaxy becomes relatively less important.

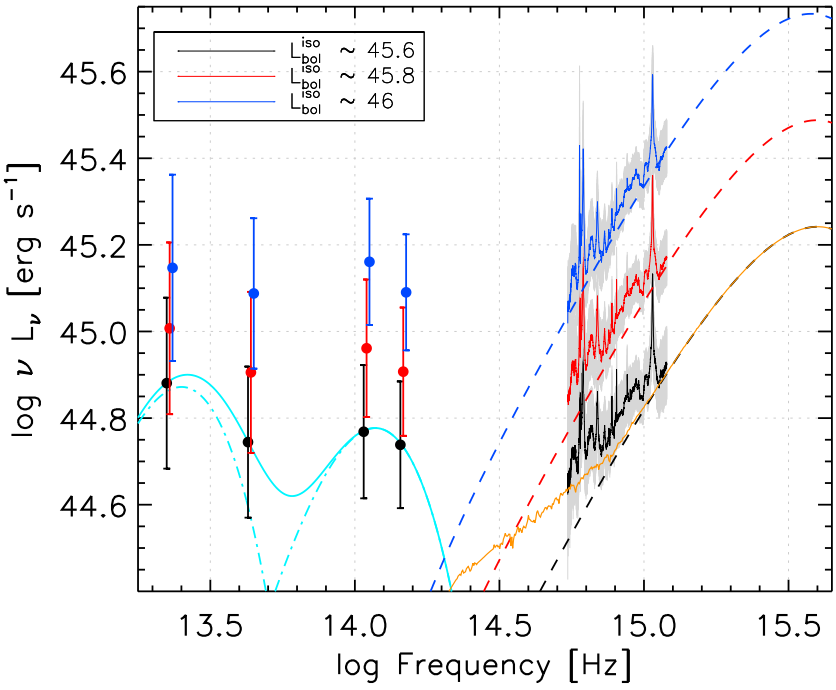

Fig. 5.3: The disc–torus connection. AGN in our sample were divided in three subsamples according to their bolometric luminosity (see Tab. 5.3), and associated to black, red and blue color respectively. The logarithmic mean and standard deviation of IR luminosities in each subsample are computed using data from WISE, and displayed as filled circles and bars (points are slightly displaced for a clearer view). Composite optical/NUV spectra (solid color–coded lines) are computed as follows: SDSS spectra are transformed to rest–frame and de–reddened using Schlegel et al. (1998) and Pei (1992). The spectra are then rebinned to a common wavelength grid and a composite spectrum is computed as the geometric mean. The gray shades indicate the 68% level dispersion. Standard Shakura and Sunyaev (1973) accretion disc spectra fitting the composite spectra are shown with dashed lines. The disc–torus connection is clearly visible in this figure, in which the torus luminosity in all four WISE bands follows the trend in accretion disc bolometric luminosity. Discrepancies between the composite spectrum in the lower luminosity subsamples (black and red) and the accretion disc spectrum may be due to the contribution of host galaxy starlight (Vanden Berk et al., 2001). The yellow solid line shows the sum of the accretion disc spectrum (black dashed line) and the elliptical galaxy template from Mannucci et al. (2001) with a bolometric luminosity of $\log(L_{\rm host}/{\rm erg\ s^{-1}}) \sim 44.3$. The IR points may be modeled as sum (solid line) of at least two black bodies with temperatures 308 K and 1440 K (dot–dashed lines), and luminosities $\log(L_{\rm torus,BB}/{\rm erg\ s^{-1}}) = 45.00$ and 44.91 respectively.

Chapter 6

AD modeling procedure

6.1 Introduction

As discussed in Chap. 4 and 5 the broad–bandSED of radio–quiet Type 1 AGNs can be interpreted as the superposition of two main components: the accretion disk and the obscuring torus. The identification of these component allows to estimate the fundamental physical properties of the AGN through the comparison with theoretical models. In this chapter I will discuss the observational properties of the Shakura and Sunyaev (1973) accretion disk model and their relationships with SMBH mass M and accretion rate $\dot{M}$. Then, I will present a new method for the SMBH mass estimation which relies on the AD modeling. These results are discussed in Calderone et al. (2012b).

6.2 Shakura&Sunyaev Accretion Disc (AD)

The simplest and most attractive model for accretion disc, from the observational point of view, is the steady state (all disc parameters does not change with time), geometrically thin (characteristic height is much smaller than linear size), optically thick (emitted radiation is in thermodynamic equilibrium with accreting plasma) accretion disc. The last two conditions translate into an allowed range for the Eddington ratio: $\ell = L_{\rm d}/L_{\rm Edd}$ must be in the range 0.01–1. Shakura and Sunyaev (1973) have shown that if we parametrize the viscosity in the disc by a single parameter α (with values in the range

0–1) the structure of the accretion disc can be resolved analytically and the main physical parameters (surface density, radial velocity, pressure) can be determined as a function of α. Furthermore, the rate at which energy is emitted (at each radius) does not depend on the detailed viscosity mechanism. Finally, the hypothesis of optical thickness in the vertical direction allows us to assume that each annulus emits radiation as a black body, with a well defined temperature. This accretion disc model is known as α–disc (hereafter AD).

The AD model is likely an over–simplification of the problem, especially at inner radii: the disc is not necessarily geometrically thin; radiation pressure may exceed thermal pressure and the disc may "inflate"; relativistic correction may be important. Finally, the accretion rate is hardly steady. Nevertheless the robustness of the physics involved, the simplicity of the model and the independence from the detailed mechanism of viscosity allow to easily connect observational properties of the AD to physical parameters. Furthermore, there is empirical evidence that the AD model provides at least a rough prediction of the expected spectrum from an accretion disc. Detailed treatment of accretion disc theory can be found in several text books (e.g. Frank et al., 2002; Longair, 2010) or reviews (e.g. Pringle, 1981)

Here I will review the properties of geometrically thin, optically thick accretion discs (Shakura and Sunyaev, 1973, hereafter SS73 model) adopted in our analysis of the SED, with particular emphasis on their observational properties associated to AGNs.

The amount of gravitational energy released from each annulus of the disk is given by

$$F(R) = \frac{3}{8\pi}\left(\frac{R}{R_{\rm g}}\right)^{-3}\left[1-\left(\frac{R}{R_{\rm in}}\right)^{-1/2}\right]\frac{\dot{M}c^2}{R_{\rm g}^2} \tag{6.1}$$

where R is the distance from the black hole, $R_{\rm g} = GM/c^2$ is the gravitational radius of the black hole, $R_{\rm in}$ is the inner radius of the disk. By introducing the adimensional parameters:

$$x = \frac{R}{R_{\rm in}} \qquad \eta = \frac{R_{\rm g}}{2R_{\rm in}} \tag{6.2}$$

we rewrite the emitted flux as $F(R) = \tilde{F}(x)\ \mathcal{P}$, with

$$\tilde{F}(x) = \frac{3}{\pi} x^{-3}(1 - x^{-1/2}) \qquad \mathcal{P} = \eta^3 \frac{\dot{M}c^2}{R_{\rm g}^2} \tag{6.3}$$

where all physical quantities are cast into the $\mathcal{P}$ parameter, while $\tilde{F}(x)$ accounts for dimensionless flux distribution. The total disk luminosity is given by

$$\begin{aligned} L_{\rm d} &= 2 \times \int_{R_{\rm in}}^{R_{\rm out}} 2\pi R\ F(R)\ {\rm d}R \\ &= \left[3 \int_1^{x_{\rm out}} x^{-2}(1 - x^{-1/2})\ {\rm d}x\right] \eta \dot{M} c^2 \end{aligned} \tag{6.4}$$

where $x_{\rm out} = R_{\rm out}/R_{\rm in}$ is the normalized outer radius of the disk. The quantity in squared parentheses is equal to 1 (provided $R_{\rm out} \gg R_{\rm in}$), therefore the parameter η as defined above is the radiative efficiency of the disk. By assuming $R_{\rm in} = 6R_{\rm g}$ (appropriate for a non–rotating black hole) we obtain $\eta \sim 0.1$.

The maximum amount of energy flux is (by differentiating Eq. 6.3):

$${\rm MAX}[F(R)] = F(R_{\rm max}) = \frac{64}{\pi} \left(\frac{3}{7}\right)^7 \mathcal{P} \tag{6.5}$$

and it is emitted at a radius $R_{\rm max} = 49/36\ R_{\rm in}$. The assumption of optical thickness implies that each annulus emits radiation as a black body with temperature: $T(R) = [F(R)/\sigma]^{1/4}$. The maximum temperature is therefore (Eq. 6.5):

$$\frac{T_{\rm max}}{[{\rm K}]} = 3.46 \times 10^4 \left(\frac{\eta}{0.1}\right)^{3/4} \left(\frac{M}{10^9 M_\odot}\right)^{-1/2} \left(\frac{\dot{M}}{M_\odot\ {\rm yr}^{-1}}\right)^{1/4} \tag{6.6}$$

The emitted spectrum is a superposition of black body spectra:

$$\begin{aligned} L_\nu &= 2 \times \int_{R_{\rm in}}^{R_{\rm out}} 2\pi\ R\ {\rm d}R\ \pi B[\nu, T(R)] \\ &= 4\pi^2 R_{\rm in}^2 \mathcal{P}^{3/4} \int_1^{x_{\rm out}} x\ {\rm d}x\ B\left[\frac{\nu}{\mathcal{P}^{1/4}}, \left(\frac{\tilde{F}(x)}{\sigma}\right)^{1/4}\right] \end{aligned} \tag{6.7}$$

where $B[\nu, T(R)]$ is the Planck function. The spectrum profile is completely

determined by the dimensionless integral, the only dependences on physical parameters ($\mathcal{P}$) being the characteristic frequency ($\propto \mathcal{P}^{1/4}$) and the overall normalization ($\propto R_{\rm in}^2 \mathcal{P}^{3/4}$). The disk spectra are therefore self–similar, and the peak frequency and luminosity scale as:

$$\begin{aligned} \frac{\nu_{\rm p}}{[\rm Hz]} &= \mathcal{A} \left(\frac{\eta}{0.1}\right)^{3/4} \left(\frac{M}{10^9 M_\odot}\right)^{-1/2} \left(\frac{\dot{M}}{M_\odot \ {\rm yr}^{-1}}\right)^{1/4} \\ \frac{\nu_{\rm p} L_{\nu_{\rm p}}}{[\rm erg \ s^{-1}]} &= \mathcal{B} \left(\frac{\eta}{0.1}\right) \left(\frac{\dot{M}}{M_\odot \ {\rm yr}^{-1}}\right) \end{aligned} \tag{6.8}$$

where $\nu_{\rm p}$ is the frequency of the peak in the νL_ν representation, $\log \mathcal{A} = 15.25$ and $\log \mathcal{B} = 45.36$. By introducing the Eddington ratio $\ell = L_{\rm d}/L_{\rm Edd}$ (with $L_{\rm Edd} = 1.3 \times 10^{47} (M/10^9 M_\odot)$ erg s^{-1}), the previous equations can be rewritten as:

$$\begin{aligned} \frac{\nu_{\rm p}}{[\rm Hz]} &= \mathcal{A} \left(\frac{\eta}{0.1}\right)^{1/2} \left(\frac{M}{10^9 M_\odot}\right)^{-1/4} \left(\frac{\ell}{0.04}\right)^{1/4} \\ \frac{\nu_{\rm p} L_{\nu_{\rm p}}}{[\rm erg \ s^{-1}]} &= \mathcal{B} \left(\frac{M}{10^9 M_\odot}\right) \left(\frac{\ell}{0.04}\right) \end{aligned} \tag{6.9}$$

Notice that, for a given value of η, an estimate of the peak luminosity and of the peak frequency allow to determine the physical parameters M and $\dot{M}$.

The spectrum of an AD is shown in Fig. 4.2 (black solid line): the superposition of black body spectra, weighted by the surface of emitting annuli produces a "flat" spectrum with slope[1] $\alpha_\nu \sim 1/3$; at highest frequencies, the Wien spectrum from the inner ring dominates, and the overall spectrum decays exponentially.

The self–similarity of AD spectra implies the existence of relations among quantities at the peak frequencies in the L_ν and the νL_ν representations ($\nu_{\rm p'}$ and $\nu_{\rm p}$ respectively), and the disk luminosity $L_{\rm d}$:

$$\frac{\nu_{\rm p}}{\nu_{\rm p'}} = 3.1 \qquad \frac{L_{\nu_{\rm p}}}{L_{\nu_{\rm p'}}} = 0.66 \qquad \frac{\nu_{\rm p} L_{\nu_{\rm p}}}{L_{\rm d}} = 0.5 \tag{6.10}$$

Also, note that the peak luminosity $\nu_{\rm p} L_{\nu_{\rm p}}$ is independent from the actual value of $R_{\rm out}$, as long as $R_{\rm out} \gtrsim 10 \, R_{\rm in}$. The relation between the maximum

[1] The slope $\alpha_\nu = 1/3$ is achieved only for $R_{\rm out} \to \infty$. For a finite value of the outer radius of the disk, such as the one used in this work $R_{\rm out} = 2 \times 10^3 R_{\rm g}$, a more realistic value for the slope is $\alpha_\nu \sim 1/4$.

temperature in the disk and the color temperature of the AD spectrum (i.e. the black body temperature associated to the peak frequency $\nu_{\mathrm{p}'}$) is $T_{\max} = 3.5\, T_{\mathrm{col}}$.

6.2.1 Peak shift

The physical parameters η, M and $\dot{M}$ uniquely identify the frequency and luminosity of the spectral peak (Eq. 6.8 or 6.9). Variations of one or more of these parameters will shift the peak along specific directions, whose slope in a $\log \nu L_\nu$ vs. $\log \nu$ plot is given by:

$$\alpha = \frac{\mathrm{d} \log \nu_{\mathrm{p}} L_{\nu_{\mathrm{p}}}}{\mathrm{d} \log \nu_{\mathrm{p}}} \tag{6.11}$$

Here is a list of peak shift relations used in this work:

1. vertical shift ($\alpha = \infty$): variations in M, $\dot{M}$ with constant $\dot{M}/M^2$ ratio (fixed η);
2. horizontal shift ($\alpha = 0$): variations in M with constant $\dot{M}$ (fixed η);
3. $\alpha = 4$: variations in $\dot{M}$, with constant M (fixed η);
4. $\alpha = -4$: variations in M and $\dot{M}$, with constant $\ell \propto \dot{M}/M$ (fixed η);
5. no shift: variations in all parameters, with constant $\eta\dot{M}$ and η/M.

In particular, case (v) is used in §7.4.1 to show that if the actual radiative efficiency η is greater than hypothesized in §6.3.1, then our SMBH mass estimate is a lower limit. The physical interpretation of case (v) is depicted in Fig. 6.1. By following the SMBH mass estimation method outlined §6.3.2 we identify an AD model (black line) in agreement with observed data (brown line): the peak lies at the "ceiling" luminosity level determined by broad line luminosities (Eq. 4.7) and the AD spectrum is in agreement with the observed continuum. This model relies on the assumption of radiative efficiency $\eta \sim 0.1$. However, the actual value of efficiency may be different. By increasing the η parameter (i.e. decreasing the inner radius of the disk R_{in}) the peak shifts to higher frequencies and luminosities as radiation comes from the inner, hotter radii (blue line). This new model would no longer be in agreement with the "ceiling" luminosity argument, therefore we must decrease the accretion rate (green line), leaving M and η unchanged. Still,

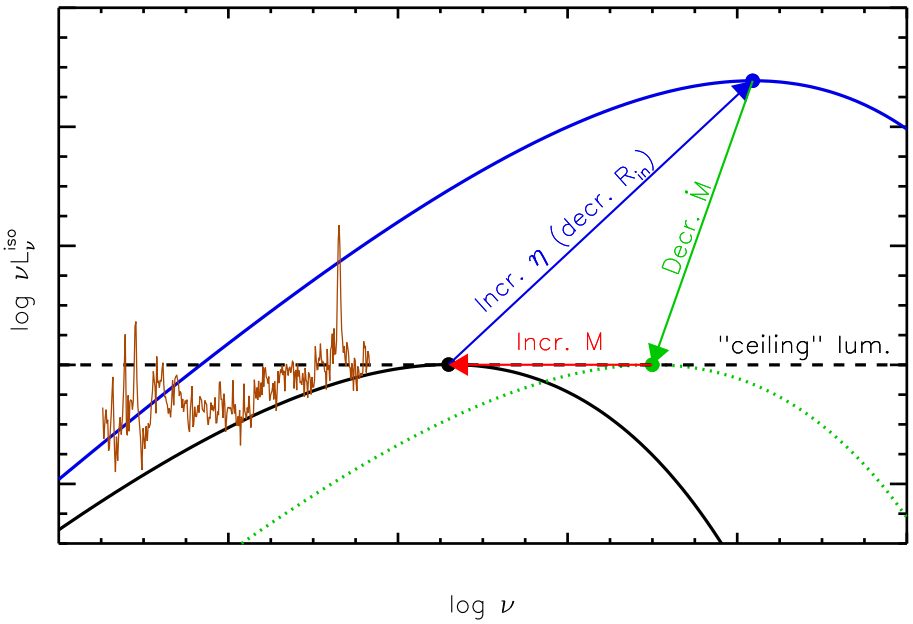

Fig. 6.1: The SMBH mass estimate provided by the AD modeling procedure (§6.3) show a linear dependence on the assumed value of the radiative efficiency: $M \propto \eta$ (case (v) in §6.2.1). The physical interpretation of this dependence is shown in the figure: the AD model (black line) identified is in agreement with observed data (brown line). In particular the peak lies at the "ceiling" luminosity level determined by broad line luminosities (Eq. 4.7) and the AD spectrum is in agreement with the AGN continuum. By increasing the η parameter (i.e. decreasing the inner radius of the disk $R_{\rm in}$) the peak shifts to higher frequencies and luminosities as radiation comes from the inner, hotter radii (blue line). This new model would no longer be in agreement with the "ceiling" luminosity argument, therefore we must decrease the accretion rate (green line), leaving M and η unchanged. Still, the obtained spectrum is not in agreement with the observed continuum, therefore we must decrease the "temperature" of the spectrum (§7.4.2), by increasing M (red line). The final AD model is again in agreement with observed data, but has higher values of η and M (and a lower value of $\dot{M}$).

the obtained spectrum is not in agreement with the observed continuum, therefore we must decrease the "temperature" of the spectrum (§7.4.2), by increasing M (red line). The final AD model is again in agreement with observed data, but has higher values of η and M (and a lower value of $\dot{M}$).

6.2.2 Observational properties

The emission from the whole (geometrically thin) disk is anisotropic since the observed flux is proportional to the projected area seen by the observer, i.e. $F_\nu \propto \cos\theta$, where θ is the viewing angle. By requiring $\oint_{\rm Sph.} F_\nu D_{\rm L}^2 d\Omega = L_\nu$ we obtain:

$$L_\nu = \frac{2\pi D_{\rm L}^2 F_{\nu_o}}{(1+z)\cos\theta} \tag{6.12}$$

where $D_{\rm L}$ is the luminosity distance, $\nu_o = \nu/(1+z)$ is the observed frequency and F_{ν_o} is the observed flux density. Note that the luminosity–flux relation for a thin disk is different from the isotropic case, in particular the relation between the "isotropic equivalent" luminosity and the real luminosity is:

$$L_\nu^{\rm iso} = 2\cos\theta L_\nu \tag{6.13}$$

The observed flux is therefore (from Eq. 6.7, 6.12):

$$F_{\nu_o} = \frac{4\pi h\nu_o^3}{c^2 D_{\rm L}^2}(1+z)\cos\theta \int_{R_{\rm in}}^{R_{\rm out}} \frac{R\,{\rm d}R}{\exp\left(h\nu/kT\right)-1} \tag{6.14}$$

The model for the observed spectrum has four parameters: M, $\dot{M}$, $R_{\rm in}$ and $\cos\theta$ (the value of $R_{\rm out}$ is not important here) which are related to quantities in Eq. 6.14 through the temperature distribution given in Eq. 6.1. Not all parameter can be constrained observationally, since the viewing angle is degenerate with both $\dot{M}$ and M. Hence we are forced to make a simplifying assumption about the inclination angle: since we are interested in Type 1 AGN, we assume that the viewing angle is in the range 0–45 deg, i.e. the aperture of the obscuring torus. If observed at a greater angle, the source would likely be classified as a Type 2 AGN. The average value of $\cos\theta$ (where θ is measured from the disk normal) is:

$$\langle\cos\theta\rangle = \frac{1+\cos\theta_{\rm max}}{2} \tag{6.15}$$

By setting $\theta_{\rm max}$=45 deg we obtain $\langle\cos\theta\rangle$=0.854, corresponding to an average viewing angle of ∼30 deg. With this assumption Eq. 6.13 reads:

$$L_\nu^{\rm iso} \sim 1.7\ L_\nu \tag{6.16}$$

6.2.3 General relativistic corrections

The general relativistic model for the accretion disk is described in Novikov and Thorne (1973) and Page and Thorne (1974). The differences with respect to the AD model influencing the observational appearance of the spectrum are:

1. the innermost stable circular orbit (isco) depends on the spin parameter $a = Jc/GM^2$. For a non–rotating black hole ($a = 0$) $R_{\rm isco} = 6R_{\rm g}$. The maximum spin of an accreting black hole is $a = 0.998$ (Thorne, 1974), with $R_{\rm isco} = 1.24R_{\rm g}$. The binding energy of a particle at $R_{\rm isco}$ in units of the particle rest–mass is (e.g. Cunningham, 1975):

$$\eta_{\rm gr} = 1 - \sqrt{1 - \frac{2}{3}\frac{R_{\rm g}}{R_{\rm isco}}} \tag{6.17}$$

   i.e. $\eta_{\rm gr}(a = 0) \sim 0.06$ and $\eta_{\rm gr}(a = 0.998) \sim 0.32$. This is expected to be the maximum possible value for the radiative efficiency (compare Eq. 6.3).

2. the different radial distribution of energy flux (Page and Thorne, 1974; Zhang et al., 1997) with respect to Eq. 6.1. The resulting spectrum is still the superposition of black body spectra;

3. the spectrum received by distant observers is influenced by gravitational redshift, Doppler boost and gravitational bending of light (Cunningham, 1975).

Li et al. (2005) have developed a package to synthesize the observed spectrum for an optically thick, geometrically thin accretion disk around a Kerr black hole, taking into account all these effects. The code is available as the model `KERRBB` within the X-ray data reduction package `XSPEC` (Arnaud, 1996). In the following I will compare the spectral profiles of both the "classical" and "relativistic" models, and show that the differences are negligible for the purpose of our work.

I compute the accretion disk flux, as received by an observer at a given distance, using both the the SS73 and `KERRBB` models. The black hole mass, accretion rate and distance of the observer will be kept fixed for all the considered models.

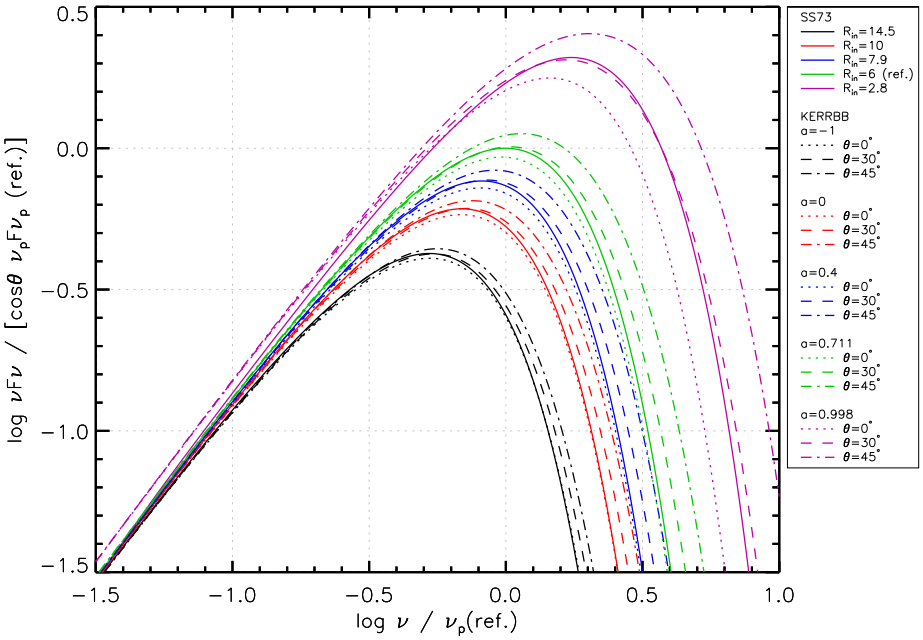

Fig. 6.2: Comparison between the SS73 (Shakura and Sunyaev 1973, solid lines) and the KERRBB (Li et al. 2005, dotted, dashed and dot–dashed lines) accretion disk spectra. The SS73 spectrum with $R_{\rm in} = 6\,R_{\rm g}$ is used as a reference spectrum: all other spectra are normalized by its peak luminosity. I consider three viewing angles $\theta = 0°, 30°$ and $45°$, and normalize all spectra by $\cos\theta$. This completely removes the dependence of the SS73 on the viewing angle. The KERRBB show a residual dependence on the viewing angle (dotted, dashed and dot–dashed lines). The colors identify a value for the inner radius of the SS73 model (respectively $R_{\rm in}/R_{\rm g} = 14.5, 10, 7.9, 6$ and 2.8) and for the black hole spin of the KERRBB model (respectively $a = -1, 0, 0.4, 0.7, 0.998$). The inner radii for the SS73 models have been chosen in order to allow the SS73 spectra to resemble as close as possible the KERRBB spectra, at given values of the spin. The resulting empirical relation between $R_{\rm in}$ and the radiative efficiency of the KERRBB model (Eq. 6.17) is given in Eq. 6.18.

I consider five SS73 AD models, by varying the inner radius of the disk $R_{\rm in}$. The values of $R_{\rm in}$ has been chosen in order to reduce the discrepancies between SS73 and KERRBB models (see below). I take the model with $R_{\rm in} = 6R_{\rm g}$ as a reference spectrum, and normalize all other SS73 spectra by the luminosity of its peak ($\nu_{\rm p}F_{\nu_{\rm p,ref}}$). These spectra are shown with solid lines in Fig. 6.2. Note that the only dependence on the viewing angle θ for the SS73 model is due to the projected area seen by the observer, i.e. to a factor $\cos\theta$. By plotting spectra normalized by $\cos\theta$ we completely remove this

dependence.

Then I consider five groups of KERRBB models, by varying the spin of the black hole: $a = -1, 0, 0.4, 0.7$ and 0.998. These values span the entire range of allowed values for the spin of an accreting black hole (Thorne, 1974). For each value of the spin, I consider three different viewing angles: $\theta = 0°, 30°$ and $45°$. All spectra are normalized by the luminosity $\nu_{\rm p} F_{\nu_{\rm p,ref}}$ of the reference SS73 model discussed above, and by $\cos\theta$. These spectra are shown with dotted, dashed and dot–dashed lines in Fig. 6.2. Note that the KERRBB models show a residual dependence on the viewing angle, due to light bending and Doppler boosting.

The values of $R_{\rm in}$ has been chosen in order to allow the SS73 spectra to resemble as close as possible the KERRBB spectra, at given values of spin. The profile of the normalized spectra are indeed very similar (spectra of the same color), the differences being at most $\pm$0.1 dex for the highest value of spin ($a = 0.998$). The (empirical) relation between the $R_{\rm in}$ in the SS73 model and the radiative efficiency of the corresponding KERRBB model is:

$$\frac{R_{\rm in}}{R_{\rm g}} = \frac{1}{2\eta_{\rm gr}} + 1.25 \tag{6.18}$$

where $\eta_{\rm gr}$ is given by Eq. 6.17.

From the observational point of view, the SS73 AD model with $R_{\rm in} = 6R_{\rm g}$ (used throughout this work) mimics the KERRBB model with spin $a \sim 0.7$ ($\eta_{\rm gr} \sim 0.1$), as long as frequencies below the peak are concerned. Therefore, the results of our work are not influenced by having neglected the general relativistic corrections in modeling the accretion disk spectrum.

6.3 Black hole mass estimation method

The AGN continuum in the rest frame wavelength range 1000–5000Å (or $\log(\nu/{\rm Hz})$=14.8–15.5), if interpreted as radiation emitted from a Shakura and Sunyaev (1973) accretion disk (§4.3), allows to constrain an AD model, and to infer the SMBH mass. Once we assume proper values for the inner radius of the disk $R_{\rm in}$ and the viewing angle θ (§6.3.1), the luminosity and frequency of the peak of the AD spectrum uniquely identify a value of the SMBH mass. In the following sections I will discuss two methods to locate the peak of the AD spectrum, and infer the SMBH mass and accretion rate.

An example of the application of both methods to a specific case will be discussed in §6.3.3.

6.3.1 Hypotheses

The methods relies on the following hypotheses, which need to be independently verified:

1. accretion in AGN occurs through steady–state, geometrically thin, optically thick, non–relativistic accretion disks. The emitted spectrum is well described by an AD model (Shakura and Sunyaev, 1973);

2. once the galaxy and/or jet contribution has been subtracted, the continuum radiation in the range $\log(\nu/\mathrm{Hz})$=14.8–15.5 (§4.3) is emitted directly from the accretion disk, i.e. it has not been reprocessed by intervening material, nor it is emitted by some other component;

3. the spatial extention of the disk is $R_{\rm in} = 6R_{\rm g}$, corresponding to a radiative efficiency $\eta \sim 0.1$. The outer radius of the disk $R_{\rm out} = 2 \times 10^3 R_{\rm g}$ is not critical, since at frequencies much smaller than $\nu_{\rm p}$ the AD spectrum will always be hidden by other emitting components. The assumption for $R_{\rm in}$, on the other hand, is more critical, since our SMBH mass estimates show a linear dependence on this value (case (v) of §6.2.1);

4. the relation between disk luminosity and its "isotropic equivalent" counterpart is $L_\nu^{\rm iso} = \langle 2\cos\theta \rangle L_\nu$ (Eq. 6.16). Since we are interested in Type 1 AGN the viewing angle is in the range 0–45 deg (i.e. the aperture of the obscuring torus, Calderone et al., 2012c). The averaged de–projection factor is thus $\langle 2\cos\theta \rangle \sim 1.7$ (Eq. 6.15, 6.16), corresponding to a viewing angle of ∼30 deg.

The AD model has four parameters: M, $\dot{M}$, $R_{\rm in}$ and $\cos\theta$ (§6.2.2). With the assumptions discussed above, the remaining unknown parameters are the SMBH mass M and the accretion rate $\dot{M}$.

6.3.2 Procedure

Usually the localization of the peak of the AD spectrum is not accessible by using a single instrument, requiring optical/UV multiwavelength observa-

tions. When these observations are available it is possible to constrain the AD model, and estimate the frequency $\nu_{\rm p}$ and luminosity $\nu_{\rm p}L^{\rm iso}_{\nu_{\rm p}}$ of the peak. The latter can then be used to infer the total disk luminosity $L^{\rm iso}_{\rm d}$ (Eq. 6.10). Finally, the SMBH mass and the accretion rate can be estimated as follows:

$$\begin{aligned}\frac{M}{10^9 M_\odot} &= 1.44 \left(\frac{\nu_{\rm p}}{10^{15}\ {\rm Hz}}\right)^{-2} \left(\frac{L^{\rm iso}_{\rm d}}{\langle 2\cos\theta\rangle \times 10^{45}\ {\rm erg\ s^{-1}}}\right)^{1/2} \\ \frac{\dot{M}}{M_\odot\ {\rm yr^{-1}}} &= 0.21 \left(\frac{L^{\rm iso}_{\rm d}}{\langle 2\cos\theta\rangle \times 10^{45}\ {\rm erg\ s^{-1}}}\right)\end{aligned} \tag{6.19}$$

The uncertainties on these results can be estimated by propagating the uncertainties in the $\nu_{\rm p}$ and $\nu_{\rm p}L^{\rm iso}_{\nu_{\rm p}}$ parameters in the above equations. Hence, whenever the data allow to constrain the location of the peak of the AD spectrum, the accuracy of the SMBH mass estimate is determined only by the accuracy of the data points (e.g. Sbarrato et al., 2012). When UV observation are not available (or not reliable) the location of the peak cannot be constrained, and we must resort to an alternative method.

The LINE procedure

Here I propose a new method for the AD modeling which relies on broad line luminosities to estimate the total disk luminosity. Fig. 6.3 illustrates the method. I use Eq. 4.7 to estimate $L^{\rm iso}_{\rm d}$. When both the Hβ and Mg II line luminosities were provided by our spectral fitting (§7.2) I considered the average of the resulting disk luminosities. This enables us to estimate a value for the luminosity of the peak $\nu_{\rm p}L^{\rm iso}_{\nu_{\rm p}}$ (Eq. 6.10), i.e. to fix a "ceiling" in the νL_ν representation (black dashed line in Fig. 6.3): the peak of the AD spectrum must lie on this line. Then I use observations from a single instrument (SDSS) to constrain the peak frequency $\nu_{\rm p}$, which is related to the SMBH mass. In particular, I shift the AD spectrum horizontally (green arrow), until the AD spectrum reproduces the AGN continuum identified in §7.2. Note that the model to be compared with data in Fig. 6.3 is an "isotropic equivalent" AD spectrum (Eq. 6.13). The resulting AD model (red solid line) provides an estimate for $\nu_{\rm p}$, to be used (along with $L^{\rm iso}_{\rm d}$) in Eq. 6.19 to infer the SMBH mass and accretion rate. Finally, I compute the Eddington ratio ℓ using the luminosity of the disk:[2] $\ell = L_{\rm d}/L_{\rm Edd}$.

[2] We are neglecting the contribution from the torus in computing the Eddington luminosity since it is reprocessed radiation from the disk. If we had used the bolometric luminosity $L_{\rm bol}$,

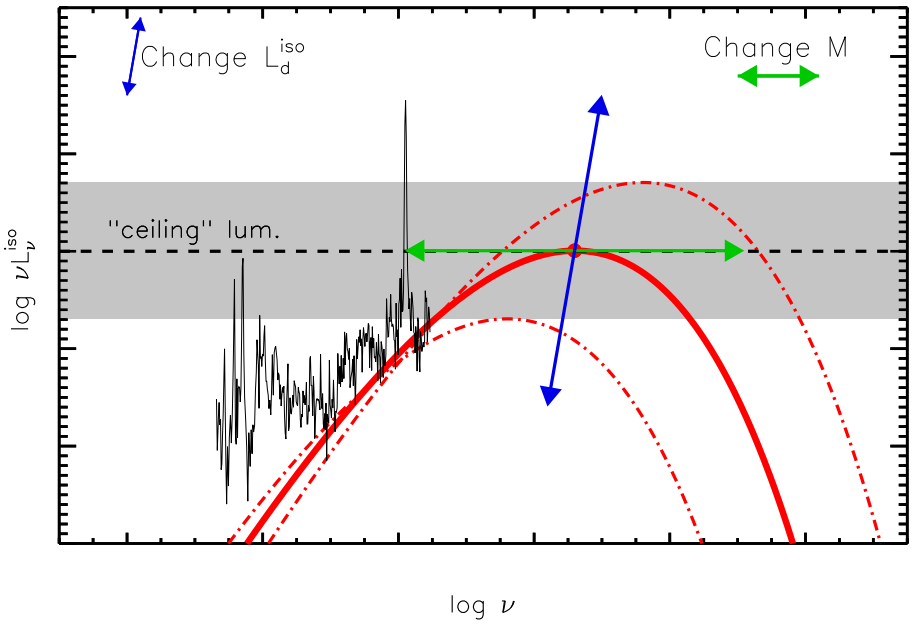

Fig. 6.3: The LINE SMBH mass estimation procedure: the SDSS source spectrum (black line) is analyzed with our fitting procedure (§7.2) in order to estimate the broad line luminosities. Then I use Eq. 4.7 to estimate $L_{\rm d}^{\rm iso}$. This is equivalent to estimate a value for the luminosity of the peak $\nu_{\rm p} L_{\nu_{\rm p}}^{\rm iso}$ (Eq. 6.10), i.e. to fix a "ceiling" in the νL_ν representation (black dashed line). Then I use the SDSS spectrum to constrain the peak frequency $\nu_{\rm p}$, which is related to the SMBH mass. In particular, I shift the AD spectrum horizontally (green arrow), until the AD spectrum reproduces the AGN continuum identified in §7.2. The resulting AD model (red solid line) provides an estimate for $\nu_{\rm p}$, to be used (along with $L_{\rm d}^{\rm iso}$) in Eq. 6.19 to infer the SMBH mass and accretion rate. The uncertainty in the disk luminosity $L_{\rm d}^{\rm iso}$ (a factor 2, §4.3.2) is shown as a grey shade. In order to evaluate a confidence interval for our estimate of M I repeat the whole process requiring the peak luminosity of the AD spectrum to lie respectively at the top and the bottom of the grey stripe. The resulting AD models (dot–dashed red lines) provide respectively the lower and upper limits of the confidence interval on the SMBH mass.

The main source of uncertainty in the process is the uncertainty in the disk luminosity $L_{\rm d}^{\rm iso}$ (a factor 2, §4.3.2). This uncertainty is shown as a grey shade in Fig. 6.3. In order to evaluate a confidence interval for our estimates of M I repeat the whole process requiring the peak luminosity of the AD

instead of $L_{\rm d}$, the resulting value would be overestimated by a factor 3.4 on average (Eq. 4.1 and 6.16).

spectrum to lie respectively at the top and the bottom of the grey stripe. The resulting AD models (dot–dashed red lines) provide respectively the lower and upper limits of the confidence interval on the SMBH mass, which typically is ± 0.5 dex. In some case these limiting AD models are too distant from the data to provide a meaningful description of the AGN continuum. This occurs typically for the low luminosity solution, corresponding to the upper limit in SMBH mass (e.g. §6.3.3). In these cases a visual inspection would reduce the thickness of the grey stripe, and hence the uncertainty on the SMBH mass.

Further sources of uncertainties are the assumption on the radiative efficiency $\eta \sim 0.1$ and on the viewing angle $\theta \sim 30$ deg (§6.3.1). The uncertainty due to the former can be estimated by considering that our SMBH mass estimate is $M \propto \eta$ (case (v) of §6.2.1), and that the actual value of η is expected to range from ∼6% (for non–rotating black hole) to at most ∼30% (for a spin parameter $a = Jc/GM^2 = 0.998$, Thorne, 1974). Therefore the uncertainty on the SMBH mass due to the uncertainty on η (and ultimately on the black hole spin) is +0.5/-0.2 dex. If we consider the possibility that the black hole can be maximally counter–rotating (with respect to the direction of accretion) then the uncertainty on the SMBH mass due to the uncertainty on η becomes ± 0.5 dex. The uncertainty due to the assumption on the viewing angle can be estimated by propagating the error in Eq. 6.19. Typically, this is negligible compared to the uncertainties discussed above, being at most 0.04 dex (a factor ∼1.1), provided $\theta_{\rm max}$ <45 deg. The uncertainties due to $L_{\rm d}^{\rm iso}$ and η are likely uncorrelated, therefore, the maximum expected uncertainty for the SMBH mass estimate is ± 0.7 dex.

The `LINE` procedure can be implemented without any fitting procedure, provided we have an estimate for the broad line luminosities and the AGN continuum (§7.2). The search for the peak frequency can be implemented by identifying a wavelength λ_0 and the corresponding luminosity of the AGN continuum $\lambda_0 L_{\lambda_0}$, and requiring the AD spectrum to match this luminosity at the same wavelength. A comparison between the resulting AD model and the AGN continuum can be performed "a posteriori" in order to assess the reliability of the SMBH mass estimate (§6.3.2). For SDSS spectra of sources with $z < 0.8$ the value of λ_0 has been chosen empirically as follows:

$$\lambda_0 = \lambda_{\rm min} \left(\frac{\lambda_{\rm max}}{\lambda_{\rm min}} \right)^{0.25}$$

where $\lambda_{\rm min}$ and $\lambda_{\rm max}$ are the minimum and maximum rest–frame wavelengths of the SDSS spectrum. This value is sufficiently close to the short wavelength edge in order to minimize the contamination from other continuum components (either galaxy or jet); λ_0 is also sufficiently far from the shortest available wavelength, at which the estimated luminosity may be unreliable due to noise and/or edge artifacts. Following these prescriptions the `LINE` method can be efficiently implemented as an automated procedure on large samples.

The `BEST` procedure

In order to assess the reliability of the `LINE` procedure I proceed with a visual localization of the AD spectrum peak using the SDSS and GALEX observations. Photometry from GALEX has been de–reddened following the same procedure as for the optical SDSS spectra (§7.2). In addition, when a jet component is considered in the spectral fitting, I compute the jet–subtracted GALEX photometry. I can not exclude that further absorption took place either in the AGN environment or the intervening medium, therefore I consider the photometry as lower limits to the actual rest–frame luminosity. Note that SDSS and GALEX data are not simultaneous, therefore it may happen that these data sets trace the source in two different state of emission, e.g. a disk or a jet dominated state (Calderone et al., 2012a).

For each source I require the slope of the AD spectrum to match as close as possible the slope in the AGN continuum (§7.2), and to lie above the (jet–subtracted) GALEX photometry. A few exceptions to these rules will be considered in §7.4. Since this is a manually tuned AD model I associate no error to the corresponding SMBH mass.

6.3.3 Example of application of the methods

As an example I discuss the case of SDSS J09531.7.09+283601.5 (#6), in Fig. 6.4. The WISE photometry is shown with black filled circles. The spectral fit (§7.2) is shown as a black line, while the AGN continuum component is shown as cyan line. The jet power law extrapolation from IR data is shown as a purple line. The GALEX photometry and their jet subtracted counterparts are shown as open circles and "+" symbols respectively. The disk luminosity $L_{\rm d}^{\rm iso}$ with its uncertainty of a factor 2 is shown as a grey stripe: the peak of

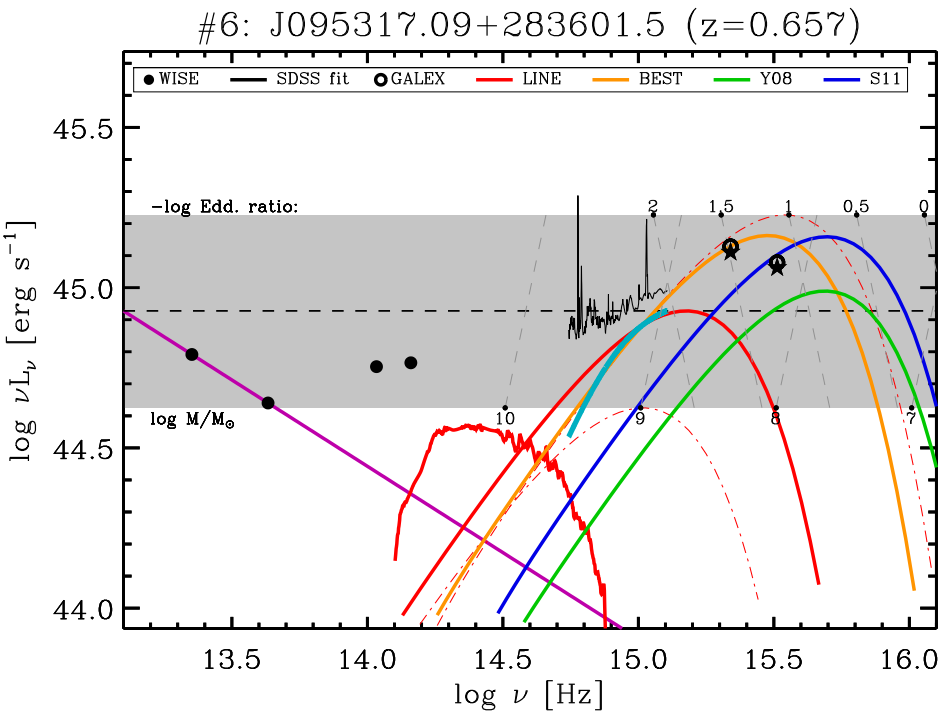

Fig. 6.4: Application of the SMBH mass estimation methods to the source SDSS J09531.7.09+283601.5 (#6). The WISE photometry is shown with black filled circles. The spectral fit (§7.2) is shown as a black line, while the AGN continuum component is shown as cyan line. The jet power law extrapolation from IR data is shown as a purple line. The GALEX photometry and their jet subtracted counterparts are shown as open circles and "+" symbols respectively. The disk luminosity $L_{\rm d}^{\rm iso}$ with its uncertainty of a factor 2 is shown as a grey stripe: the peak of the AD model must lie within this region. The grey dashed grid shows the location of peaks for AD models with values of SMBH mass and Eddington ratio shown respectively below and above the grey stripe. The `LINE` (§6.3.2) and `BEST` (§6.3.2) AD models are shown with a red and orange solid line respectively. In order to evaluate the uncertainty on the `LINE` SMBH mass I repeat the procedure by requiring the AD model to peak at the top and the bottom of the grey stripe. The resulting AD models are shown with dot–dashed red lines.

the AD model must lie within this region. The grey dashed grid shows the location of peaks for AD models with values of SMBH mass and Eddington ratio shown respectively below and above the grey stripe.

By applying our SMBH mass estimation methods I identify the `LINE` and `BEST` AD models, shown with a red and orange solid line respectively. Both AD models provide a rather good representation of the AGN continuum. The `BEST` AD model, however, needs a slightly higher luminosity than the `LINE`

model in order to lie above the (jet–subtracted) GALEX photometry. Note that the observed spectrum (black line) has a significantly lower spectral slope (i.e. it is "redder") than the AGN continuum, because of the host galaxy and jet contributions. Having considered these components in the spectral analysis allows us to reveal the real AGN continuum (cyan line) whose slope agrees with our AD spectrum.

In order to evaluate the uncertainty on the `LINE` SMBH mass we repeat the procedure by requiring the AD model to peak at the top and the bottom of the grey stripe. The resulting AD models (shown with dot–dashed red lines) are found to bracket the real case: the lower one cannot account for the AGN continuum, while the higher one is significantly above the GALEX photometry. This situation often occurred during the analysis of the sources (§7.4), therefore our SMBH mass uncertainties are rather conservative.

Our AD models can be compared with those corresponding to the SEV masses and bolometric luminosities reported in the Y08 and S11 catalogs (green and blue lines). I consider the disk luminosity as computed using Eq. 4.1. Note that our peak luminosities are very similar to those of Y08 and S11, since this is the condition I required (on average) to calibrate Eq. 4.7. However, these models do not provide a good description of the AGN continuum because their peak frequencies lie $\sim$0.25 dex above our estimates of $\nu_{\rm p}$, therefore our SMBH mass estimates are 0.5 dex (a factor $\sim$3, Eq. 6.8) greater than the SEV ones. The possible reasons to explain such differences will be discussed in §7.4.1.

Chapter 7

Mass estimates for a sample of 23 RL–NLS1

7.1 The sample

In this chapter I will apply the SMBH estimation method developed inn §6.3 on a sample of 23 Radio–Loud, Narrow–Line Seyfert 1 sources (RL–NLS1) given in Yuan et al. (2008, hereafter Y08). These results are discussed in Calderone et al. (2012b).

Each considered source will be identified by a sequential index (#1, #2, etc...), following the same order as in Tab. 1 of Y08. All sources have been spectroscopically observed in the SDSS, and 21 over 23 sources are also in the S11 catalog. The IR photometry at 3.4μm, 4.6μm, 11.6μm, 22.1μm from WISE (Wide–field Infrared Survey Explorer, Wright et al., 2010) is available for all sources. Finally, 21 over 23 sources have photometric measurements by GALEX (Martin et al., 2005), either in the Medium Imaging Survey (MIS), or the All sky Imaging Survey (AIS). When multiple GALEX observations were available, I find significant variability in a few cases (#3, #8, #18) possibly due to the jet component. In these cases I chose preferably the MIS photometry with lower luminosity.

The redshifts are in the range z =0.1–0.8, therefore the continuum in the SDSS spectra will likely trace the AD component (§4.3). The FWHM(Hβ) are less than 2200 km s^{-1}, as required by the definition of NLS1 given in Zhou et al. (2006). The SEV black hole masses are in the range $\log(M/M_{\odot})$ =6–8,

while the Eddington ratio are ℓ =0.5–3 (Yuan et al., 2008). The radio morphology is compact, unresolved on $5''$ scale, and the radio loudness (Kellermann et al., 1989) is >100 for all sources.

The overall observational properties are very similar to that of blazars (Yuan et al., 2008), and the γ–ray emission from these sources has been predicted, and later detected in 7 RL-NLS1 sources (Abdo et al., 2009c; Calderone et al., 2011; Foschini, 2011), 4 of which are in the Y08 sample. However, these sources show unusually small widths of broad emission lines, and consequently small SEV SMBH mass estimates, when compared to typical blazars.

In order to apply our SMBH mass estimation method (§6.3) to the sources in the sample I need to perform a spectroscopic analysis of the SDSS data. In particular I need to disentangle the host galaxy and/or jet contribution from the AGN continuum, and estimate the emission line luminosities. This procedure is described in the following section.

7.2 Spectral analysis

I used the spectra from the Sloan Digital Sky Survey (SDSS, York et al., 2000), data release 7 (DR7, Abazajian et al., 2009). I dropped spectral bins marked by at least one of the following mask flags:[1] `SP_MASK_FULLREJECT`, `SP_MASK_LOWFLAT`, `SP_MASK_SCATLIGHT`, `SP_MASK_BRIGHTSKY`, `SP_MASK_NODATA`, `SP_MASK_COMBINEREJ`, `SP_MASK_BADSKYCHI`. Also, I dropped 100 bins at the beginning and end of each spectrum, in order to eventually avoid artifacts from instrument or pipeline.

Each spectrum has been de–reddened using the Galactic extinction values estimated from dust IR emission maps in Schlegel et al. (1998), and the extinction law reported in Cardelli et al. (1989) and O'Donnell (1994). I am currently neglecting any intrinsic reddening in the rest–frame of the source. Then I transformed the spectra to the rest frame by assuming isotropic emission (i.e. multiplying the flux by $4\pi D_{\rm L}^2$). The redshift estimates are provided by the SDSS pipeline. Finally, I rebinned each spectrum by a factor of 3 in order to improve the signal to noise ratio, resulting in a spectral resolution of $\lambda/\delta\lambda$ ∼1450 (corresponding to ∼200 km s^{-1}).

The model used to fit the spectra consists of five components:

[1] See `http://www.sdss.org/dr7/dm/flatFiles/spSpec.html`.

- a smoothly broken power law to account for the AGN continuum ("AGN continuum" component) ;

- a spiral[2] host galaxy template spectrum from Mannucci et al. (2001) and a power law to (eventually) account for the synchrotron emission from the jet ("galaxy" and "jet" components respectively). The galaxy component has a single free parameter (the overall normalization). The parameters for the jet component are estimated using data from WISE (Wide–field Infrared Survey Explorer, Wright et al., 2010). In particular I use the photometry in the two bands at the longest wavelengths (11μm and 22μm) to estimate the luminosity and the slope of the power law.[3] If the resulting slope is greater than –1 I extrapolate the power law to optical wavelengths and subtract the contribution from the SDSS spectrum. Otherwise I do not consider any jet component. Parameter of the jet component are fixed during the fitting process;

- the iron templates from Vestergaard and Wilkes (2001) (at UV wavelengths) and from Véron-Cetty et al. (2004) (at optical wavelengths);

- a Gaussian profile for each emission line listed in Tab. 7.1. The FWHM of narrow lines are forced to be in the range 200–1000 km s^{-1}, while that of broad lines are forced in the range 1000–3000 km s^{-1}. Furthermore, the FWHM and velocity offset of the Hβ narrow component is tied to the width and offset of [O III] λ4959 and [O III] λ5007.

- a maximum of 10 additional Gaussian line profiles which are not "a priori" associated to any specific transition. These components are necessary to account for (e.g.) the iron blended emission lines in the range 3100–3500Å (not covered by the above–cited iron templates), or line asymmetries. The FWHM of the additional lines are forced to be in the range 1000–3000 km s^{-1}, except for lines in the range 3100–3500Å for which the upper limit is 10^4 km s^{-1}. A posteriori, I check whether the wavelength range identified by the full width at half maximum of these additional lines contains any of the transition lines listed in

[2]The results of the spectral fitting procedure do not change significantly by considering the elliptical galaxy template from Mannucci et al. (2001).

[3]In analyzing the source SDSS J094857.32+002225.5 (#5) I also applied an exponential cutoff at $\log[\nu/\mathrm{Hz}] = 14$ (Abdo et al., 2009b).

Table 7.1: List of emission lines used in modeling SDSS spectra. Third column (Type) indicates if a broad (B), a narrow (N) or both components are used in the fit.

Line	Wave [Å]	Type	Line	Wave [Å]	Type
C II	2326	B	N I	5199	N
Mg II	2798	BN	He I	5876	BN
Ne V	3426	N	Fe VII	6087	N
O II	3727	N	O I	6300	N
Ne III	3869	N	Fe X	6375	N
H δ	4101	B	N II	6548	N
H γ	4340	BN	H α	6563	BN
O III	4363	N	N II	6583	N
He II	4686	BN	S II	6716	N
H β	4861	BN	S II	6731	N
O III	4959	N	Ar III	7136	N
O III	5007	N			

Tab. 7.1. In this case I associate the two components, and numerically compute the line luminosity on the composite line profile.

The main feature of this spectroscopic analysis procedure is that it is able to fit a spectrum of a non–absorbed, Type 1 AGN with a single model covering the rest–frame wavelength range from 1200Å to ∼7000Å. The procedure is similar to the one used in Shen et al. (2011), although the approach is considerably different. The list of main differences are discussed below:

1. I use a single smoothly broken power–law to describe the AGN continuum over the entire rest–frame spectrum, while S11 uses power laws over a rather narrow wavelength range (<300Å) to describe the continuum below each considered emission line (see point (3) below). This component is to be compared with the AD spectrum §6.3.2;

2. I try to fit the host galaxy component using a template, while S11 does not consider host galaxy subtraction;

3. at optical wavelengths I use the iron template from Véron-Cetty et al. (2004), while S11 uses the one from Boroson and Green (1992). Furthermore I provide a width estimate for blended iron lines at both optical and UV wavelengths;

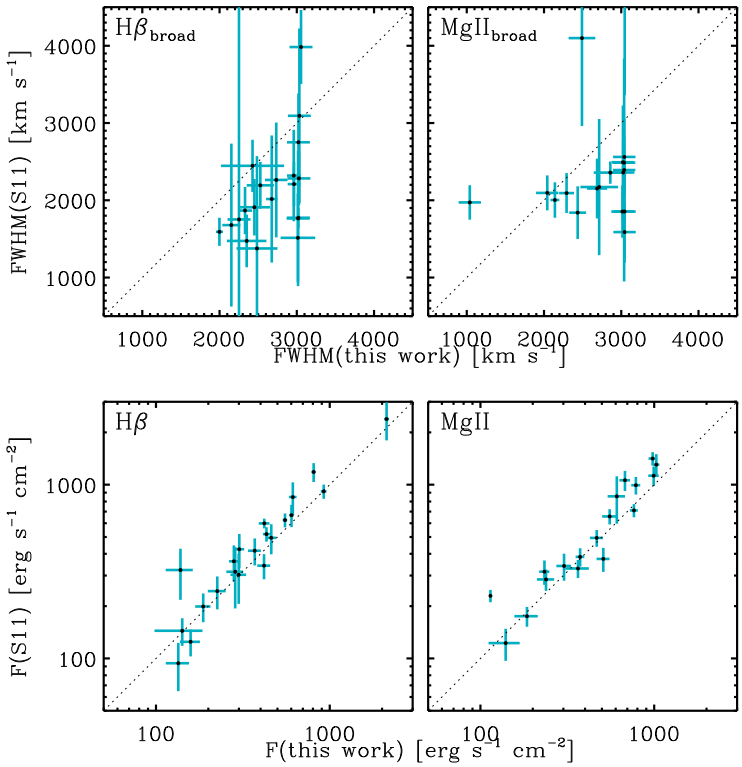

Fig. 7.1: Comparison of the Hβ and Mg II line widths and luminosities among the S11 catalog and this work. The S11 values of FWHM for Hβ are on average 20% smaller than our estimates, although with considerable scatter. The Mg II estimates show an even greater scatter and are not correlated. On the contrary, the luminosity estimates are in good agreement.

4. I fit all main lines supposed to be relevant in the considered wavelength range (Tab. 7.1), while S11 consider only Hα, Hβ, MgII, CIV and nearby narrow lines;

A comparison of between my estimates (FWHM and and line luminosities of Hβ and Mg II) and those from S11 is shown in Fig. 7.1. The S11 values of FWHM for Hβ are on average 20% smaller than our estimates, although with considerable scatter. The Mg II estimates show an even greater scatter and are not correlated. On the contrary, the luminosity estimates are in good agreement.

Results of the spectral fitting are shown in Tab. 7.2 and Fig. A.1.

Table 7.2: Results of the spectral fitting for the 23 RL–NLS1 sources in Yuan et al. (2008) catalog. Columns are: (1) source numeric identifier; (2) SDSS name of the source; (3) redshift; (4) luminosity and error of the Hβ emission line (both the broad and narrow components); (5) luminosity and error of the Mg II emission line (both the broad and narrow components); (6) wavelength λ_0 and (7) luminosity $\lambda_0 L_{\lambda_0}$ used to constrain the LINE model (see §6.3.2); (8) jet component (extrapolated from WISE data to wavelength λ_0) to AGN continuum luminosity ratio.

#	SDSS Name	z	$\log \frac{L(\mathrm{H}\beta)}{\mathrm{erg\ s^{-1}}}$	$\log \frac{L(\mathrm{Mg\ II})}{\mathrm{erg\ s^{-1}}}$	$\log \frac{\lambda_0}{\text{Å}}$	$\log \frac{\lambda_0 L_{\lambda_0}}{\mathrm{erg\ s^{-1}}}$	$\frac{L_{\mathrm{J},0}}{L_{\lambda_0}}$
1	J081432.11+560956.6	0.509	42.96 ±0.01	42.99 ±0.02	3170	45.11	—
2	J084957.98+510829.0	0.583	42.29 ±0.12	42.52 ±0.04	3039	43.58	5.67
3	J085001.17+462600.5	0.523	42.48 ±0.04	42.51 ±0.03	3157	44.61	0.13
4	J090227.16+044309.6	0.532	42.61 ±0.03	42.93 ±0.02	3127	44.67	0.07
5	J094857.32+002225.5	0.584	42.81 ±0.03	42.85 ±0.03	3039	45.15	0.00
6	J095317.09+283601.5	0.657	42.54 ±0.03	42.84 ±0.02	2893	44.88	0.10
7	J103123.73+423439.3	0.376	42.31 ±0.02	—	3486	44.12	—
8	J103727.45+003635.6	0.595	42.52 ±0.05	42.31 ±0.04	3020	44.73	—
9	J104732.68+472532.1	0.798	43.10 ±0.03	43.04 ±0.04	2674	45.15	0.12
10	J111005.03+365336.3	0.630	42.36 ±0.04	42.59 ±0.03	2944	44.26	0.01
11	J113824.54+365327.1	0.356	42.26 ±0.01	—	3547	43.87	0.64
12	J114654.28+323652.3	0.465	42.68 ±0.01	42.65 ±0.03	3285	44.75	—
13	J123852.12+394227.8	0.622	42.41 ±0.05	42.48 ±0.03	2961	44.59	0.02
14	J124634.65+023809.0	0.362	42.43 ±0.02	—	3525	44.66	0.05
15	J130522.75+511640.3	0.785	43.79 ±0.01	43.47 ±0.01	2692	45.74	0.47
16	J143509.49+313147.8	0.501	42.43 ±0.02	42.65 ±0.03	3203	44.46	0.72
17	J144318.56+472556.7	0.703	42.82 ±0.04	43.24 ±0.02	2826	45.42	0.15
18	J150506.48+032630.8	0.408	41.90 ±0.03	42.55 ±0.04	3407	44.39	0.14
19	J154817.92+351128.0	0.478	42.84 ±0.01	42.93 ±0.02	3249	45.05	0.06
20	J163323.58+471859.0	0.116	41.66 ±0.02	—	4303	43.74	0.43
21	J163401.94+480940.2	0.494	42.45 ±0.02	42.02 ±0.02	3213	44.56	0.14
22	J164442.53+261913.2	0.144	41.86 ±0.01	—	4200	43.95	0.25
23	J172206.03+565451.6	0.425	42.55 ±0.01	42.64 ±0.03	3370	44.68	0.04

7.3 Results

I analyzed the data from the 23 RL–NLS1 sources of the Y08 catalog. The spectral analysis (§7.2) of each individual source is shown in Fig. A.1. The results are summarized in Tab. 7.2. The fitting models are in good agreement with data (reduced χ^2 are in the range 1.16–2.91). Also, the jet contribution at optical/NUV wavelengths is typically negligible, except for the #2, #11, #15, #16, #20 and #22 sources.

The results of our SMBH mass estimation methods (§6.3) are shown graphically in Fig. A.2 (adopting the same notation as in Fig. 6.4). The results are summarized in Tab. 7.3. The AD models identified by the `LINE` procedure provide a rather good description of the AGN continuum in 17 over 23 cases (indicated with a blank in the second column of Tab. 7.3). The remaining 6 sources cannot be modeled with an AD spectrum, and are considered "bad cases" (indicated with a "*" symbol in the second column of Tab. 7.3, see §7.4 for a discussion of these sources). These sources will not be considered in the following analysis.

The comparison between the SMBH mass estimates for the `LINE` and `BEST` AD models are shown in Fig. 7.2. The mean value for the ratio of the two mass estimates is:

$$\left\langle \log \frac{M[\texttt{LINE}]}{M[\texttt{BEST}]} \right\rangle = 0.07 \pm 0.37 \tag{7.1}$$

The two SMBH mass estimates are therefore compatible, within the uncertainties associated to the `LINE` procedure (§6.3.2).

Fig. 7.3 shows the comparison between the black hole masses from the AD models (`LINE` in upper panels, `BEST` in lower panels) and the SMBH masses from the SEV method, as given in the Y08 (left panels) and S11 (right panels) catalogs. The uncertainty associated to SEV mass is assumed to be 0.5 dex. Fig. 7.4 shows the histogram of the ratio of our SMBH mass estimates to the SEV ones from the Y08 (left panel) and S11 (right panel) catalogs. The mean values for the ratio of the mass estimates are:

$$\begin{aligned} \left\langle \log \frac{M[\texttt{LINE}]}{M[\text{Y08}]} \right\rangle &= 1.2 \pm 0.5 \qquad \left\langle \log \frac{M[\texttt{LINE}]}{M[\text{S11}]} \right\rangle = 0.8 \pm 0.3 \\ \left\langle \log \frac{M[\texttt{BEST}]}{M[\text{Y08}]} \right\rangle &= 1.1 \pm 0.4 \qquad \left\langle \log \frac{M[\texttt{BEST}]}{M[\text{S11}]} \right\rangle = 0.8 \pm 0.3 \end{aligned} \tag{7.2}$$

Table 7.3: Results of our SMBH mass estimation method. Columns are: (1) source numeric identifier; (2) flag to indicate if the AD "signature" (i.e. the slope $\alpha_\nu > -1$ a t optical wavelengths, see §7.4) is missing. (3) peak frequency of the AD model, (4) SMBH mass estimate (with its uncertainties) and (5) Eddington ratio for the AD model identified by our automatic procedure (`LINE` model); (6), (7), (8) corresponding quantities for the `BEST` model; SEV mass estimate given in the (9) Y08 and (10) S11 catalogs.

		Method			**Best**			**Y08**	**S11**
#	Bad	$\log \frac{\nu_\mathrm{p}}{\mathrm{Hz}}$	$\log \frac{M}{M_\odot}$	ℓ	$\log \frac{\nu_\mathrm{p}}{\mathrm{Hz}}$	$\log \frac{M}{M_\odot}$	ℓ	$\log \frac{M}{M_\odot}$	$\log \frac{M}{M_\odot}$
1		15.2	8.8 (+0.4,−0.5)	0.022	15.5	8.4	0.084	8.0	8.1
2	*	—	—	—	—	—	—	7.4	8.0
3		15.3	8.5 (+0.4,−0.5)	0.014	15.1	8.8	0.006	7.2	7.5
4		15.5	8.2 (+0.6,−0.4)	0.059	15.3	8.5	0.019	7.7	8.0
5		15.0	9.2 (+0.0,−0.6)	0.006	15.1	9.1	0.010	7.5	7.8
6		15.2	8.8 (+0.2,−0.6)	0.012	15.5	8.3	0.062	7.8	7.9
7	*	—	—	—	—	—	—	7.3	7.6
8		15.0	9.0 (+0.0,−0.7)	0.004	15.0	9.1	0.004	7.3	8.5
9	*	—	—	—	—	—	—	8.1	8.2
10	*	—	—	—	—	—	—	7.1	9.0
11	*	—	—	—	—	—	—	7.1	7.6
12		15.3	8.6 (+0.5,−0.5)	0.020	15.1	8.8	0.008	7.8	7.9
13		15.2	8.5 (+0.3,−0.5)	0.012	15.4	8.2	0.037	6.8	7.5
14		15.2	8.7 (+0.3,−0.5)	0.009	15.2	8.7	0.011	7.3	7.7
15		15.4	8.8 (+0.6,−0.4)	0.110	15.2	9.2	0.049	8.5	8.5
16		15.5	8.1 (+0.7,−0.4)	0.037	15.1	8.8	0.008	7.5	7.6
17		15.0	9.3 (+0.0,−0.5)	0.009	15.6	8.4	0.193	7.8	8.3
18		15.2	8.5 (+0.4,−0.5)	0.009	15.4	8.3	0.021	6.6	7.6
19		15.2	8.9 (+0.2,−0.6)	0.014	15.3	8.7	0.027	7.9	8.0
20	*	—	—	—	—	—	—	6.3	—
21		15.0	9.0 (+0.0,−0.8)	0.003	15.0	8.9	0.004	7.4	7.9
22		15.3	8.3 (+0.6,−0.4)	0.007	15.3	8.2	0.008	6.9	—
23		15.3	8.6 (+0.5,−0.5)	0.016	15.5	8.1	0.079	7.4	7.6

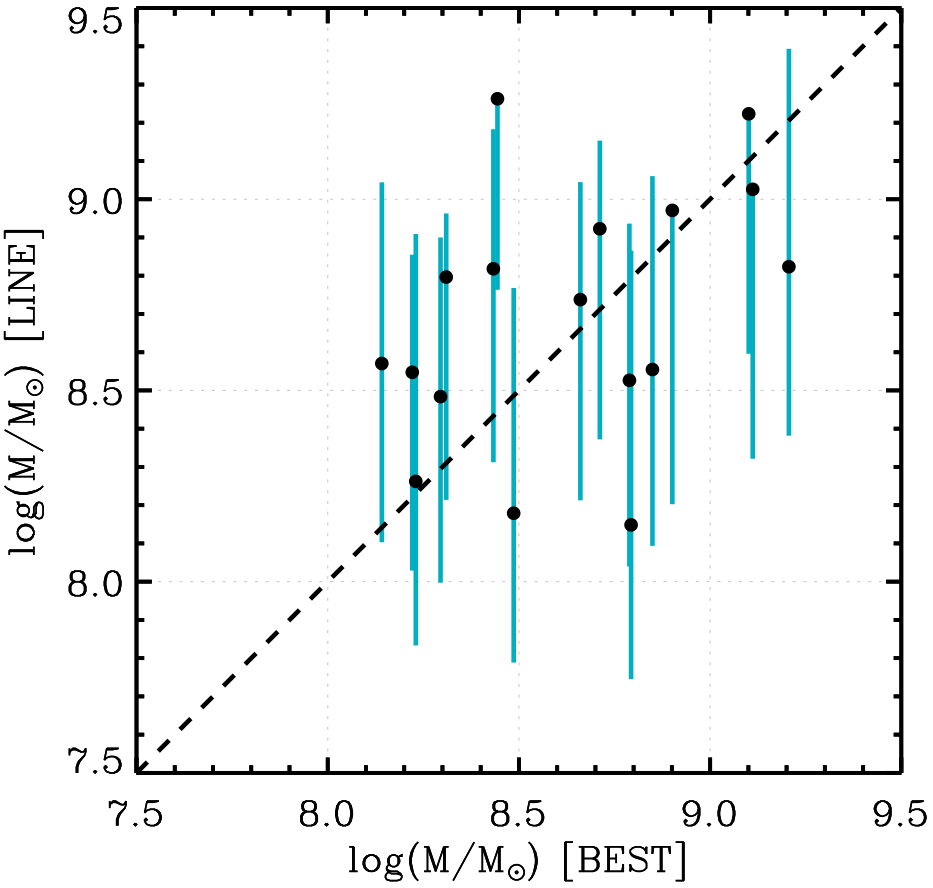

Fig. 7.2: Comparison between SMBH mass estimates obtained using the `LINE` and `BEST` procedures. Since the `BEST` estimate is a manually tuned AD model I associate no error to the corresponding SMBH mass.

The mean values are of the same order (or even greater) than the maximum uncertainty associated to the `LINE` SMBH mass estimate (0.7 dex, §6.3.2), therefore our SMBH mass estimates are not compatible with the SEV ones.

7.4 Discussion

As discussed in §4.3, the characteristic disk spectral slope $\alpha_\nu = 1/3$ cannot be directly observed in AGN SED. However for values of the SMBH mass $\log(M/M_\odot) \gtrsim 8$ and Eddington ratio $\ell \lesssim 1$, the peak of the AD spectrum is (in principle) observable. Indeed, for 17 over 23 sources considered here,

the SDSS continuum show an increasing trend in the νL_ν representation (slope $\alpha_\nu > -1$) at $\log(\nu/\mathrm{Hz}) \gtrsim 14.8$, where the accretion disk is expected to dominate over other emitting components. Assuming that the observed BBB is actually radiation emitted directly from the accretion disk, the slope $\alpha_\nu > -1$ at $\log(\nu/\mathrm{Hz}) \gtrsim 14.8$ becomes the "signature" of the presence of the AD component. In the considered sample (§7.1) 17 sources over 23 show such signature (the remaining six "bad" cases will be discussed below). Our spectral fitting procedure (§7.2) reveals an emission component that is well described by an AD model, although this has not been included "a priori" in our fitting model. Therefore, observational data are in agreement with hypothesis (i) discussed in §6.3.1. Furthermore, the absorption column densities N_H, as estimated from X–ray spectral fitting, are compatible with the Galactic values (Yuan et al., 2008; Grupe et al., 2010). Hence, we expect the radiation we observe not to be re–processed by any intervening medium, as assumed in hypothesis (ii) (§6.3.1). Furthermore, we expect the contribution from other emitting components, such as host galaxy or jet, to be negligible at frequencies where our AD models are constrained ($\log(\nu/\mathrm{Hz}) \gtrsim 14.8$). In particular, the slopes in the AGN continuum component ($\alpha_\nu > -1$) is incompatible with the ones inferred from the galaxy template of Mannucci et al. (2001). Also, the jet component is expected to decay at frequencies above a cutoff frequency of $\log(\nu/\mathrm{Hz}) \lesssim 15$, as in typical Flat Spectrum radio–quasars or powerful blazars (Ghisellini et al., 2010).

The AD models identified by the `LINE` procedure (§6.3.2) for the 17 "good" sources provide a rather good description of the AGN continuum (Fig. A.2). In particular, the AGN continuum slopes in the frequency range covered by SDSS are in good agreement with the ones from `LINE` AD models (red solid lines). Also, the two limiting solutions (dot–dashed red lines) likely bracket the real case, providing a robust estimate of our uncertainties. The average uncertainty on the SMBH mass estimates are of the order of ± 0.5 dex (Tab. 7.3). By taking into account the uncertainties due to hypotheses (iii) and (iv) (radiative efficiency $\eta \sim 0.1$ and viewing angle $\theta \sim 30$ deg) we obtain a maximum uncertainty of $\sim$0.7 dex (§6.3.2).

In order to further assess the reliability of the `LINE` SMBH mass estimates I considered the `BEST` AD models, identified by visually tuning the $L_\mathrm{d}^\mathrm{iso}$ and ν_p parameters in order to achieve the best possible match between the AGN continuum identified in §7.2 and the GALEX photometry. In a few cases I

had to relax these requirements, as discussed below:

- the assumption that we can reliably estimate the jet contribution at optical/UV wavelengths by extrapolating a power law from the WISE photometry (§7.2) may not be correct. For the #15 and #16 sources this assumption does not apply since the power law extrapolation (purple line) lies above the WISE photometry at shorter wavelengths (note that the error bars are smaller than the symbol in the plot). Source #5 would also falls in this class if the cutoff of synchrotron radiation at $\sim 10^{14}$ Hz (§7.2) is neglected, since jet extrapolation would intercept optical SDSS data. In order to identify the BEST AD model for the #15 and #16 sources I used the continuum observed in SDSS data (black solid lines in Fig. A.2) rather than the jet–subtracted one (cyan lines) as requirement at optical wavelengths. For #16 I obtained a good agreement between the BEST model and GALEX photometry. Lack of such agreement for #15 will be discussed below. A similar situation (jet component overestimated at optical/NUV wavelengths) possibly occurs also for source #22. In order to be conservative, for this source I retained the original constraints to identify the BEST model. For the other sources the jet extrapolation is marginal at optical/NUV wavelengths (Tab. 7.2), hence the assumption discussed here has a negligible effect.

- for the #5 and #15 sources the GALEX photometry does not follow the extrapolation from the SDSS slope. Therefore a single AD model is not compatible with both the SDSS and GALEX observations. This may be a consequence of source variability, since the SDSS and GALEX data are not simultaneous. Indeed, I found significant variability in GALEX photometry in a few sources (§7.2). In particular, source #5 is known to be a variable source (Abdo et al., 2009a,b; Foschini et al., 2011). In these cases the BEST model is computed relaxing the requirement of taking GALEX photometry into account, and using only the SDSS data as guidelines.

- for the #8 and #21 sources the SDSS and GALEX data appear to trace the peak of the AD spectrum. For these sources I neglected the jet component. Note that the BEST AD model for these sources provide a

robust estimate of the SMBH mass, since the peak of the AD spectrum has been directly observed.

The BEST AD models are in good agreement with the LINE ones. In particular, note that the peak in BEST AD spectra lie inside the grey stripes for all sources except #17. Hence, the Eq. 4.7 are well calibrated. The resulting BEST SMBH mass estimates are compatible the LINE ones (Eq. 7.1, Fig. 7.2). Also, the scatter in Fig. 7.2 (0.4 dex) is compatible with the uncertainty on the LINE estimates due to our ignorance on $L_{\rm d}^{\rm iso}$ (0.5 dex, §6.3.2). This provides further support for the reliability of the LINE SMBH mass estimates. I conclude that, under the assumptions discussed in §6.3.1 our LINE procedure provides a reliable estimate of the SMBH mass, within the quoted uncertainties.

In six cases the LINE method do not provide an acceptable description of data (sources marked with a "*" symbol in the second column of Tab. 7.3. For these sources the observed SDSS continuum does not show an increasing trend (in the νL_ν representation) at $\log(\nu/{\rm Hz}) \gtrsim 14.8$. In two cases the SDSS continuum are dominated by the jet and/or host galaxy emission (#2 and #11), and the AD spectrum is not directly visible. In four cases (#7, #9, #10 and #20) the observed SDSS continuum appears "flat" in the νL_ν representation, with no hints for a change of slope. Although the jet–subtracted continuum (cyan line) suggests the presence of an AD spectrum, this decomposition strongly depends on the assumption that the extrapolation of the jet component from IR data is also valid at optical wavelengths. In order to be conservative, I mark these sources as "bad", and neglect them in our analysis.

7.4.1 Comparison with SEV mass estimates

The comparison with the SEV mass reveals a systematic discrepancy between our mass estimate and those from the Y08 and S11 catalogs (Fig. 7.3 and 7.4). Although the discrepancy ($\gtrsim$0.7 dex, Eq. 7.2) is of the same order of the maximum uncertainty associated to the LINE procedure (§6.3.2), it appears systematic. Therefore our black hole mass estimates are not compatible with the SEV ones given in the Y08 and S11 catalogs. On average, our SMBH masses turn out to be a factor $\sim$6 (0.8 dex) greater than SEV ones. The peak luminosities, on the other hand, are rather similar to the ones from Y08 and S11 models, since this is the condition I required (on average) to calibrate

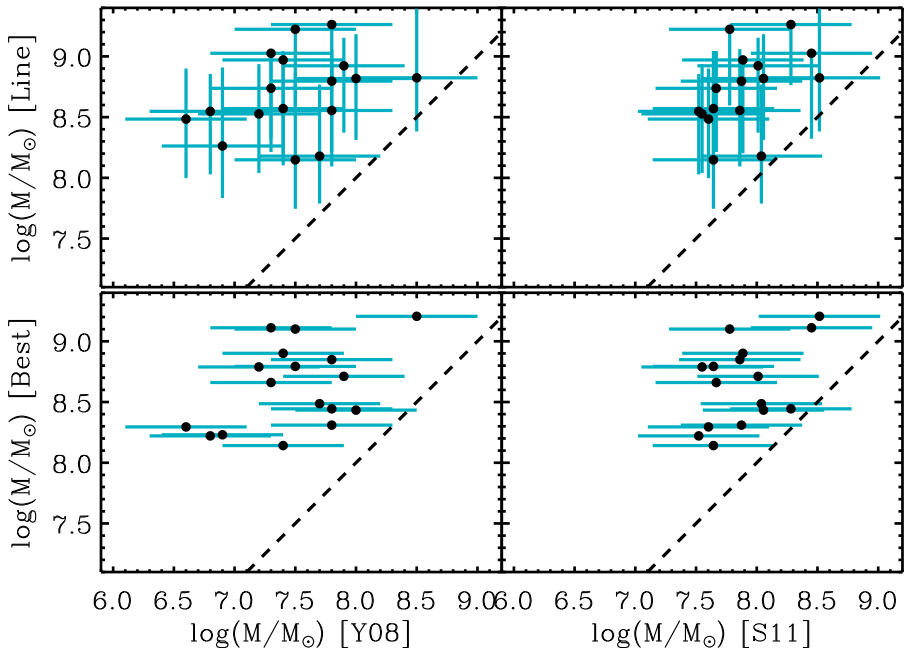

Fig. 7.3: Comparison between SMBH mass estimates of AD models identified by our procedures (`LINE` models, upper panels, `BEST` models lower panels) and SEV masses as given in the Y08 (left panels) and S11 (right panels) catalogs. The uncertainty associated to SEV mass is 0.5 dex.

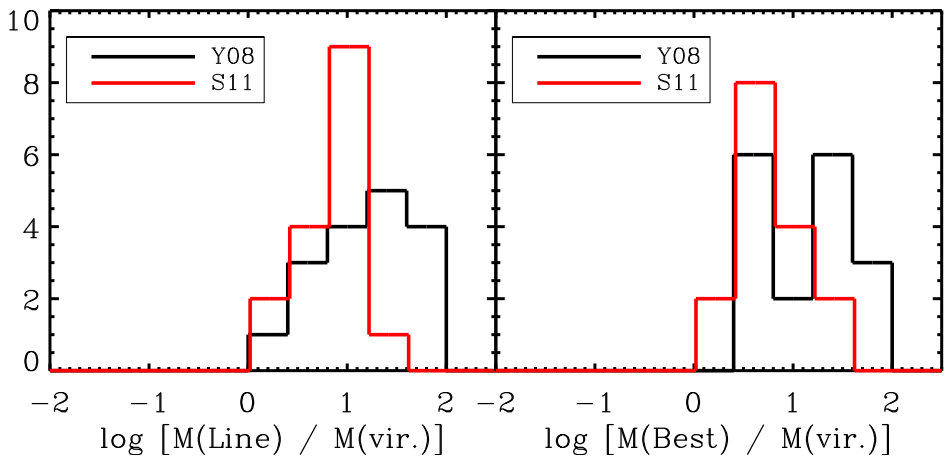

Fig. 7.4: Histogram of ratios of our SMBH mass estimates to the SEV ones from the Y08 (left panel) and S11 (right panel) catalogs. Our estimates are greater than SEV ones by ∼1 dex for Y08 and ∼0.8 for S11 (Eq. 7.2).

Eq. 4.7.

A possible explanation for the SMBH mass discrepancy between our estimates and the SEV ones may involve a radiative efficiency which is a factor ∼6 lower than assumed. However, a value of $\eta \sim 0.02$ is lower than the minimum efficiency expected for accretion onto a maximally counter–rotating black hole (~ 0.03). Notice that the AD spectrum suggests that the accretion disk is still in the "radiatively efficient" regime: half the gravitational energy gained by matter at each radius is locally emitted as radiation, i.e. it is not advected into the hole.

The mass discrepancy is not due to an inaccurate estimation of the jet contribution at optical/NUV wavelengths. If the actual jet contribution is lower than estimated, the corresponding AGN continuum luminosity ($\lambda_0 L_{\lambda_0}$ (Tab. 7.2) would correspondingly be higher. The "ceiling" luminosity level, on the other hand, are not affected by the presence of the jet, since it relies on line luminosities. In order to reproduce an higher $\lambda_0 L_{\lambda_0}$, retaining the same peak luminosity, the `LINE` AD model must shift to lower frequencies. Therefore, if the actual jet contribution is lower than estimated, I would have obtained greater `LINE` SMBH mass estimates, and greater discrepancy with SEV masses.

Also, the mass discrepancy is not due to having neglected the general relativistic corrections in the AD model. As discussed in §6.2.3, the AD model used throughout this work mimics the more sophisticated general relativistic one with $\eta_{\rm gr} \sim 0.1$, as long as frequencies below the peak are concerned.

Finally, the mass discrepancy is not a consequence of having neglected absorption in the AGN host galaxy, since the absorption column densities $N_{\rm H}$, as estimated from X–ray spectral fitting, are compatible with the Galactic values (a few times 10^{20} cm^{-2}, Yuan et al., 2008; Grupe et al., 2010). Furthermore, the amount of extinction needed to shift the peak frequency of an AD spectrum by ∼0.25 dex (corresponding to ∼0.5 dex in SMBH mass) is E(B-V) ∼ 0.2, which is a factor ∼4 higher than the average extinction for the sources in the sample. The drop in the peak luminosity for such extinction would be of a factor ∼3. Hence, by invoking absorption from the host galaxy to justify the mass discrepancy, we would find Eddington ratios a factor ∼3 above those listed in Y08, i.e. ℓ =1.5–9.

I speculate that a possible explanation for the mass discrepancy is a selection effect in calibrating the SEV method. The SEV method relies on the

calibration of both a BLR size–continuum luminosity relation and of the a virial f factor (Peterson et al., 2004; Park et al., 2012). However, the sample used to perform the calibration consists of a few dozens of sources: the ones that has been reverberation mapped. As a consequence, the calibration of the method may be biased by selection effects. In particular, the method may provide significantly underestimated SMBH masses if the BLR has a flat disk–like geometry, and it is seen almost face–on (Decarli et al., 2011). If these conditions apply, then the discrepancy between our mass estimates and the SEV ones would be greater (on average) for AGN showing the smallest widths of broad emission lines, i.e. the class of NLS1 sources (Decarli et al., 2008). The SMBH mass estimates provided by our method, on the other hand, are scarcely affected by the viewing angle and the geometry of the BLR (§6.3.2).

The Eddington ratios are in the range ℓ =0.04–0.2 (Tab. 7.3), significantly below the values reported in Y08 (0.5–3). The discrepancy is due both to our greater SMBH mass estimates (a factor ∼6) and to the fact that I used the disk luminosity $L_{\rm d}$ (instead of $L_{\rm bol}$) to compute the Eddington ratio (a factor ∼3.4, Eq. 4.1 and 6.16). Hence, our mass estimates solve the "super–Eddington" problem of RL–NLS1 sources (e.g. Komossa et al., 2006), with values of ℓ being a factor ~ 20 smaller than SEV ones (on average). With such small values of ℓ the role of radiation pressure in determining the SEV masses (Marconi et al., 2008; Chiaberge and Marconi, 2011) is expected to be small, not sufficient to explain the SMBH mass discrepancy.

The "super–Eddington" problem has been discussed also for broad–line (FWHM(Hβ)$>$ 2000 km s^{-1}) AGN in Collin et al. (2002). By using reverberation mapping mass estimates, and assuming that the observed optical luminosity is due to an AD spectrum, they found that a significant fraction of the sources in their sample is accreting at super–Eddington rates. Again, this problem can be solved by assuming that a single virial calibration does not hold for all AGN. Beyond the orientation issue discussed above, the assumption that all AGN follow the same scaling relations as quiescent galaxies may not apply. Furthermore, the scaling relations themselves (used to calibrate the virial f factor) may depend upon other parameter, such as the host morphology (§2.7). This hypothesis is supported by the recent findings by Graham et al. (2011): they show that the scatter of the M–σ_* relation may be significantly reduced when the sample selection is based on the host

morphology. As an example, the offsets of the M–σ_* relations for barred and elliptical galaxies differ by $\sim$0.45 dex, while their scatter is $\sim$0.37 dex.

7.4.2 The "temperature" argument

If the assumptions discussed in §6.3.1 apply, then all the independently estimated SMBH masses (even the SEV ones) should produce an AD spectrum compatible with the observed data. This provides a simple way to compare our results with those reported in Y08 and S11. The SMBH mass discrepancy arises because the peak frequencies of the `LINE` and `BEST` AD spectra are significantly lower then the peak frequencies of the Y08 and S11 ones, while the peak luminosities are compatible. If the Y08 and S11 AD models (blue and green lines in Fig. A.2) were the correct ones, there must be a physical process able to shift photon to lower frequencies (i.e. to lower "temperatures") in order to account for the observed data. However, such a process cannot exist on a thermodynamic basis, since black body spectra (which build up the AD model) already have the lowest temperature corresponding to a given luminosity and emitting surface. Since the luminosities are the same, the only way to reduce the temperature is to increase the emitting surface, that is by increasing the SMBH mass.

Throughout the paper I used the standard Shakura and Sunyaev (1973) model, which is expected to provide only a gross description of the disk emitted spectrum. More detailed models of the accretion disk spectrum (e.g. Hubeny et al., 2001; Done et al., 2012) would not solve the mass discrepancy, since they predict higher "color temperatures", i.e. even greater SMBH masses.

Recently, studies on microlensing variability of quasars (e.g. Morgan et al., 2010) claimed to have found similar discrepancies between accretion disk size as measured by variability and the ones expected from SEV masses. Again, these discrepancies would be reduced if the SEV masses were underestimated.

In order to solve the mass discrepancy problem, while retaining the reliability of the SEV masses, we must postulate that the radiation we observe is emitted from a surface greater than predicted by the AD model. A model following this prescription is discussed in Lawrence (2012): the radiation emergent from the disk would be entirely reprocessed by a population of

thick clouds lying at $\sim 60R_{\rm g}$. Radiation absorbed from the clouds would be mainly converted into emission lines, and observed as a false continuum because of Doppler shift due to high velocities (~ 75000 km s^{-1}). In this case the AD model would still apply, but the observed radiation would be emitted at $\sim 60R_{\rm g}$, and our SMBH masses would be overestimated. This model predicts a large X–ray absorption, since the X–ray emitting region (i.e. the corona) is co–spatial with the UV disk emission region, and well within 60 $R_{\rm g}$. Our sources, however, do not show evidence for such large absorption.

Chapter 8

Conclusions

In this work I analyzed the possible issues and systematic uncertainties related to the Single Epoch Virial method (SEV), currently the only one applicable to large samples of (spectroscopically observed) Type 1 AGNs (Chap. 2). The issues will not be settled until we reach a deeper understanding of the geometry and kinematics of the BLR, and we found a reliable indicator of the inclination of the (possibly thin) BLR with respect to the line of sight.

Given these issues the SEV mass estimates should be used carefully, especially when used as a base to infer additional results. In particular I have shown in §2.7.1 that when the SEV method is applied on large samples of Type1 AGN (selected according to a luminosity threshold, e.g. the Shen et al. 2011 catalog), the straightforward conclusion is that all considered SMBH share a single value of the mass. This is at odds with the expectation of a reasonably broad distribution of SMBH mass. In order to check whether this is true an independent mass estimation method is required.

Then I discussed the class of Narrow Line Seyfert 1 (NLS1) sources (Chap. 3). A possible interpretation of the "narrowness" of the broad Balmer emission line component for these sources is that we are observing their thin BLR almost pole–on ($\alpha < 15°$). This would introduce a systematic bias in the SEV mass estimates, and the NLS1 would appear under massive and accreting at higher Eddington ratios with respect to Broad Line AGNs (BLAGNs).

Recently it was discovered that a few radio–loud NLS1 are strong γ–ray emitters. In particular, the observed variability of γ–ray emission in these sources (§3.3.1) confirms the presence of a relativistic jet closely aligned to

the line of sight. Also, their broad band SED and jet powers are comparable to those of the most powerful blazars, suggesting that also the SMBH mass should be comparable ($M \gtrsim 10^8 M_\odot$).

I stressed that the class of NLS1 in general (both RQ and RL) is not a separate population of AGN. Rather there is a smooth transition between the observable properties of NLS1 and BLAGN.

I studied one such intermediate source (B2 0954+25A, §3.4) with particular emphasis on its SMBH mass estimation. I confirmed that B2 0954+25A indeed shares the properties of blazars and RL–NLS1 and found that the SMBH mass is in the range (1–3) $\times 10^8 M_\odot$ by using three independent methods.

In order to propose a new SMBH mass estimation method I analyzed the relationship between the broad band SED of Type 1 AGN and a Shakura and Sunyaev (1973) accretion disk model (AD model, Chap. 4). Furthermore, I analyzed the disk–torus connection (Chap. 4). By properly taking into account all necessary geometrical factors, I found an estimate for the covering factor which ($\sim$ 0.6, corresponding to an semiaperture angle of $\sim 50°$).

The characteristic disk spectral slope $\alpha_\nu = 1/3$ cannot be directly observed in the AGN SED because of the contributions from other emitting components such as the host galaxy, the torus or (for radio–loud sources) the jet (§4.3). Once these contributions are taken into account, the observations are compatible with the presence of an emitting component which is well described by an AD model. In particular, the peak of such component can be observed directly in the frequency range $\log(\nu/\mathrm{Hz}) = 14.8$–$15.5$. By comparing the average Type 1 AGN SED from Richards et al. (2006) with the AD model I calibrated the relations to estimate the total disk luminosity using the continuum line luminosities (at 1350Å, 3000Å and 5100Å) as a proxy (§4.3.1). Furthermore, by using the emission line templates from Francis et al. (1991), I calibrated analogous relations based on the line luminosities of Hβ, Mg II and C IV (§4.3.2). The latter provide more reliable disk luminosity estimates when the continuum is not dominated by the AD spectrum.

The interpretation of the Big Blue Bump (BBB) as being due to the thermal emission from an AD allows to estimate the SMBH mass and the accretion rate, once the peak luminosity and peak frequency of the AD spectrum

are identified (§6.3). This requires broad–band multiwavelength observations. However, large samples may comprise sources with poor observational coverage. Hence, I propose a new method which relies only on spectral observations at optical wavelengths. In particular, I constrain the luminosity of the peak by using the line luminosities. Then, I constrain the frequency of the peak by requiring the AD model continuum and slope to reproduce the observed AGN continuum beneath the emission lines (§6.3.2). The *maximum* uncertainty on our black hole mass estimates is ~ 0.7 dex. This uncertainty is greatly reduced if the disk luminosity can be accurately determined, namely when the peak of the AD spectrum is visible within the frequency range of the data.

I applied the method to the sample of 23 radio–loud NLS1 of Yuan et al. (2008). The method provides reliable black hole mass estimates for 17 sources over 23 (§7.3, 7.4). The remaining six sources are either dominated by synchrotron radiation from the jet, or do not show "hints" for the presence of an AD–like emitting component.

The resulting black hole mass estimates are at least a factor ~ 6 (on average) greater than the corresponding SEV mass estimates. The discrepancies are possibly due to the issues discussed in §2.7.

The SMBH masses estimated for this sample of RL–NLS1 are in the range $\log(M/M_{\odot}) =$ 8–9, while the Eddington ratios are $\ell =$0.04–0.2. Therefore, very radio–loud NLS1 appear not to be extreme in terms of black hole masses and Eddington ratios, being similar to those of powerful Flat Spectrum Radio Quasars. In particular I found no evidence for jetted sources with mass below $10^8 M_{\odot}$. By a simple physical argument (§7.4.2), I argue that our SMBH mass estimates has a greater reliability with respect to the SEV ones.

Appendix A

Figures: spectral fitting and black hole mass estimation

A.1 Figures: spectral fitting

This appendix is a collection of the figures related to the spectral fitting procedure discussed in §7.2. On the left panels we show the whole rest frame wavelength range, while on the right panels we show a detailed view on the Hβ, [O III] and Mg II regions. The SDSS data and associated uncertainties are shown with black squares and grey lines respectively. Also shown are the fitting models (red lines), as well as the individual components: the AGN continuum (black), the galaxy template (cyan), the jet component (as extrapolated from WISE photometry, purple), the iron templates (orange), the broad (blue) and narrow (green) emission lines, and the additional emission lines (grey). In lower part of left panels we show the residuals in units of data uncertainties. The red lines show the cumulative $\chi^2_{\rm red}$ (values on right axis).

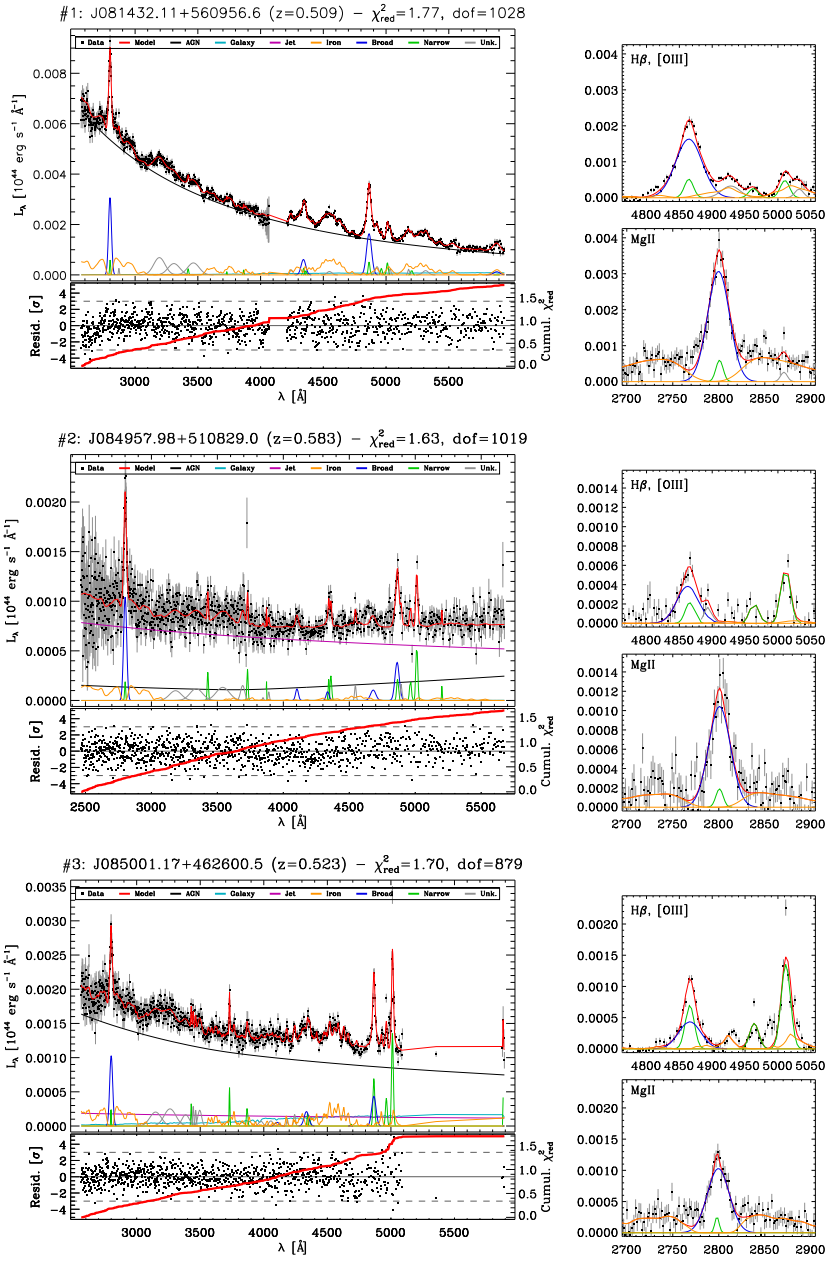

Fig. A.1: Results of the spectral fitting procedure (§7.2, App. A.1).

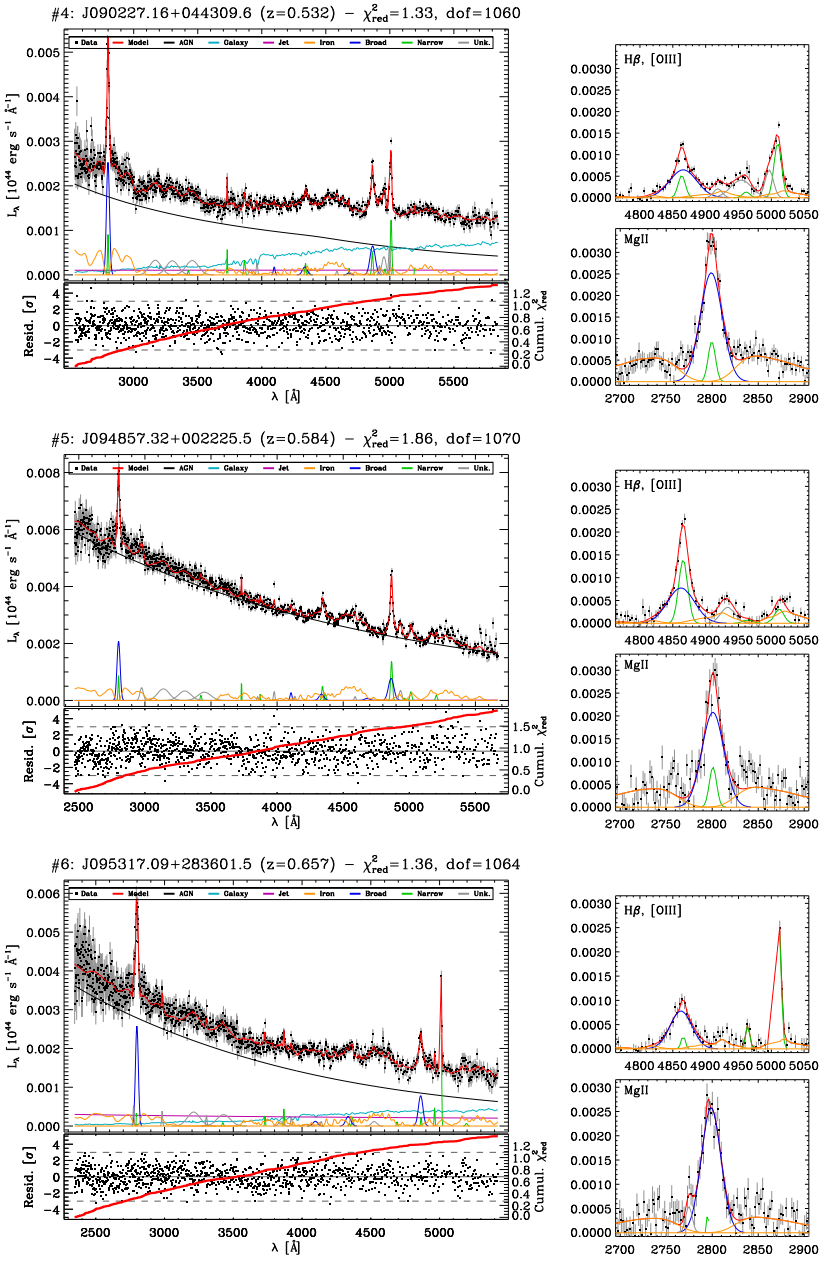

Fig. A.1: (continued)

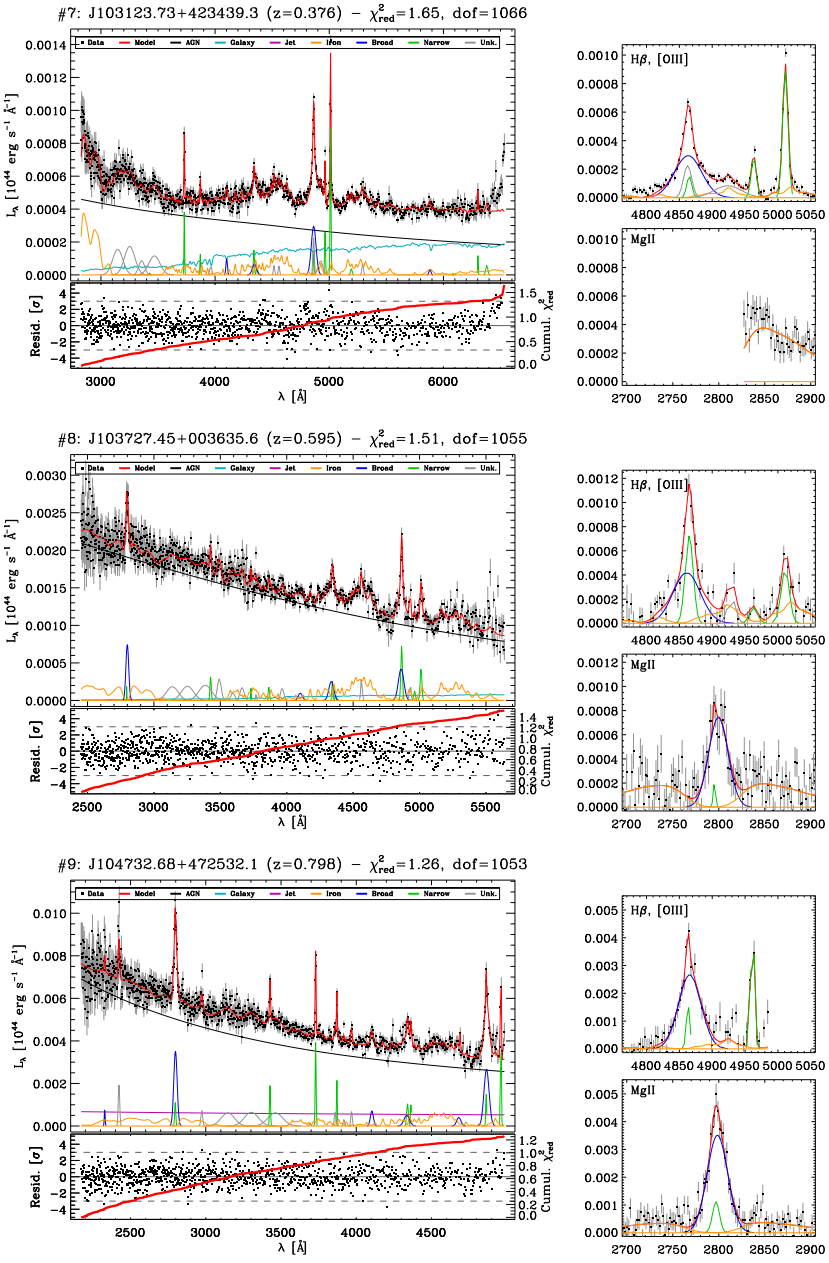

Fig. A.1: (continued)

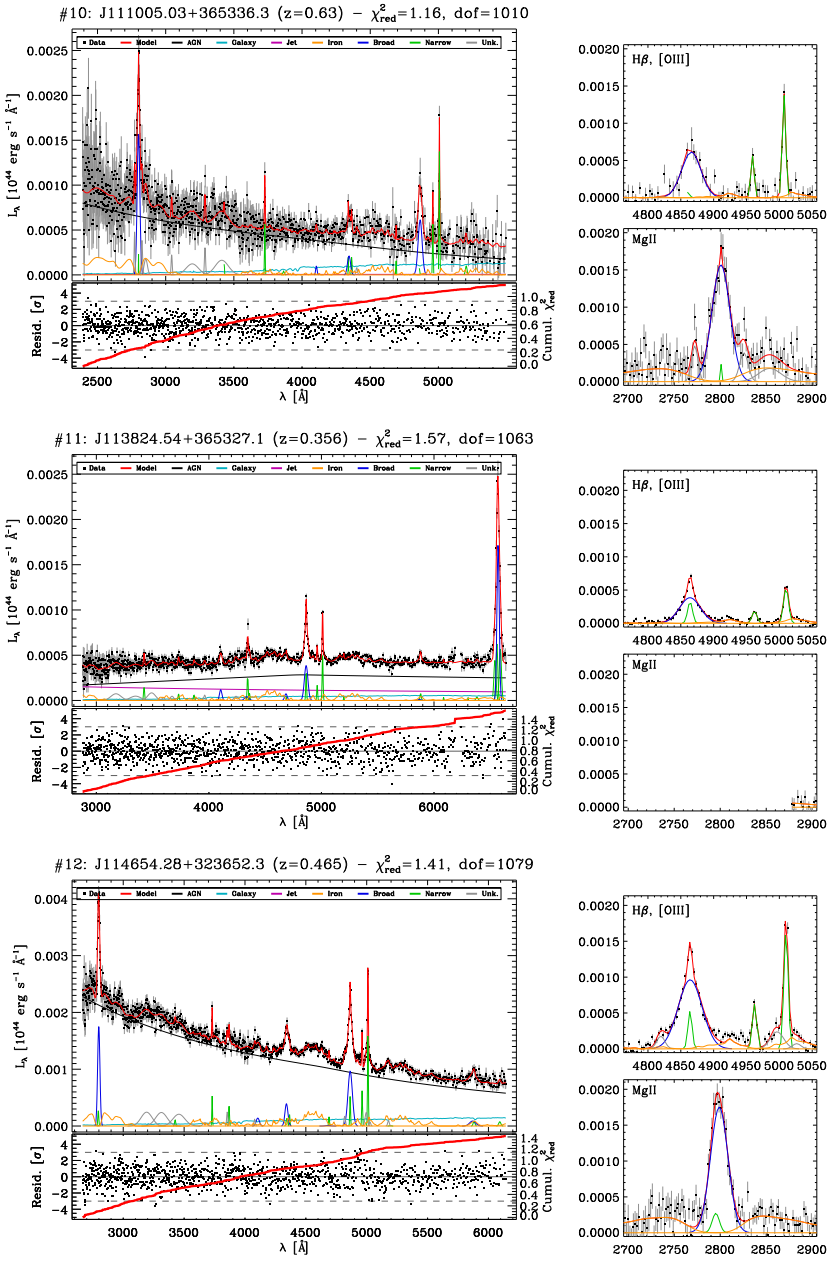

Fig. A.1: (continued)

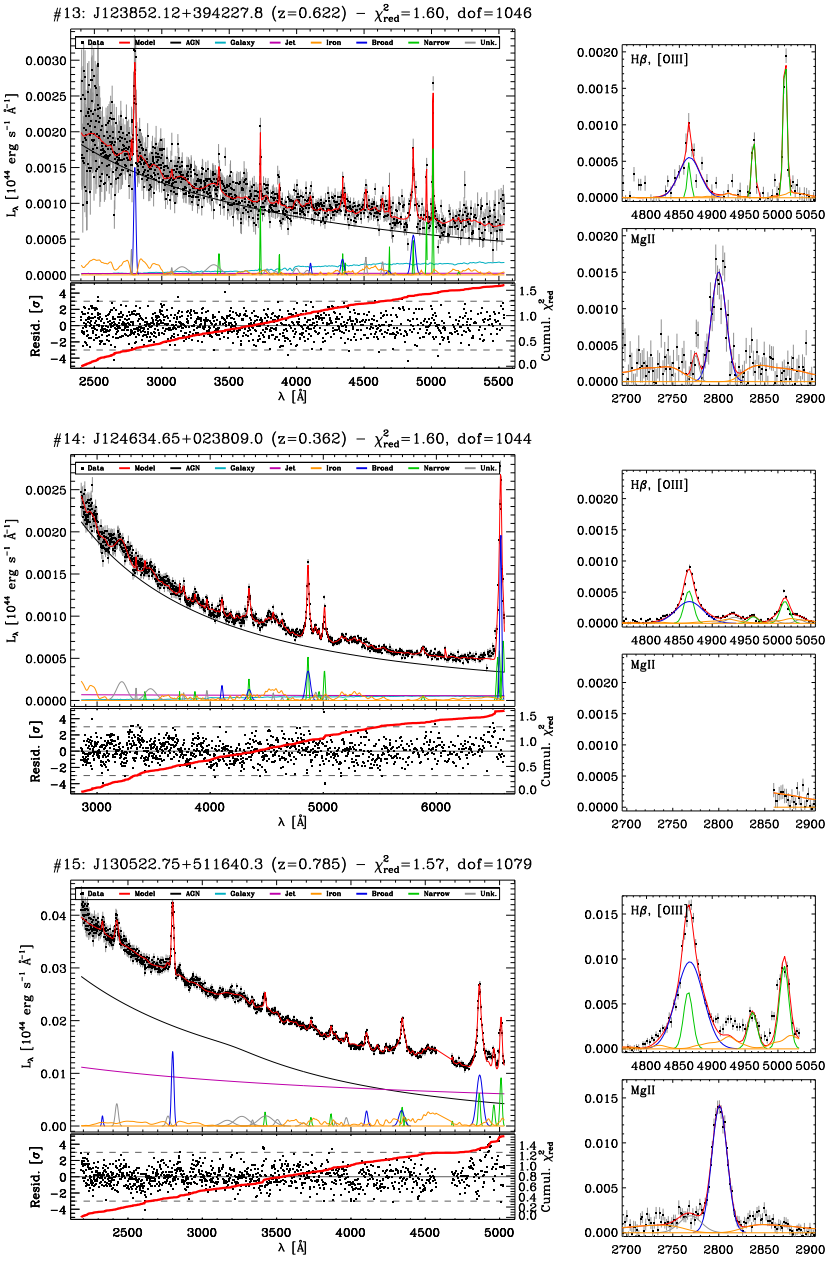

Fig. A.1: (continued)

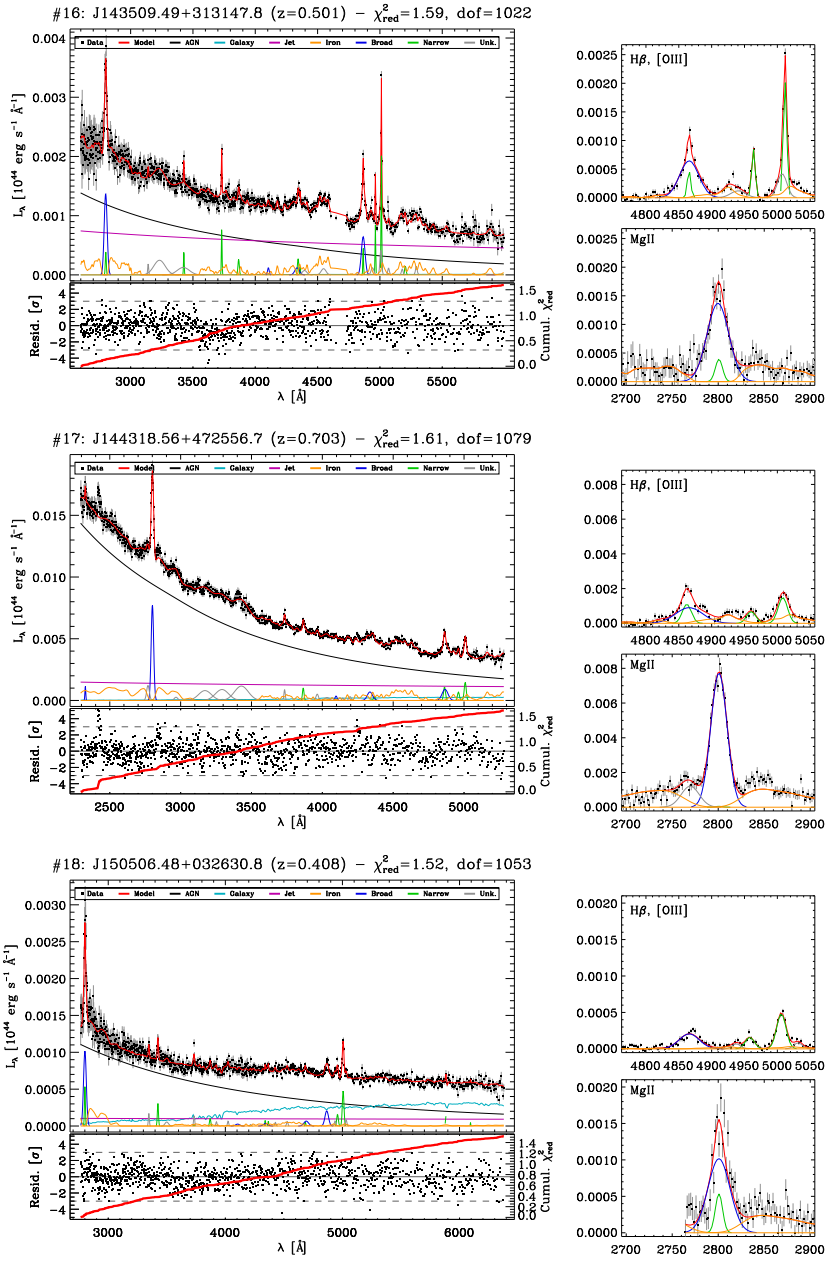

Fig. A.1: (continued)

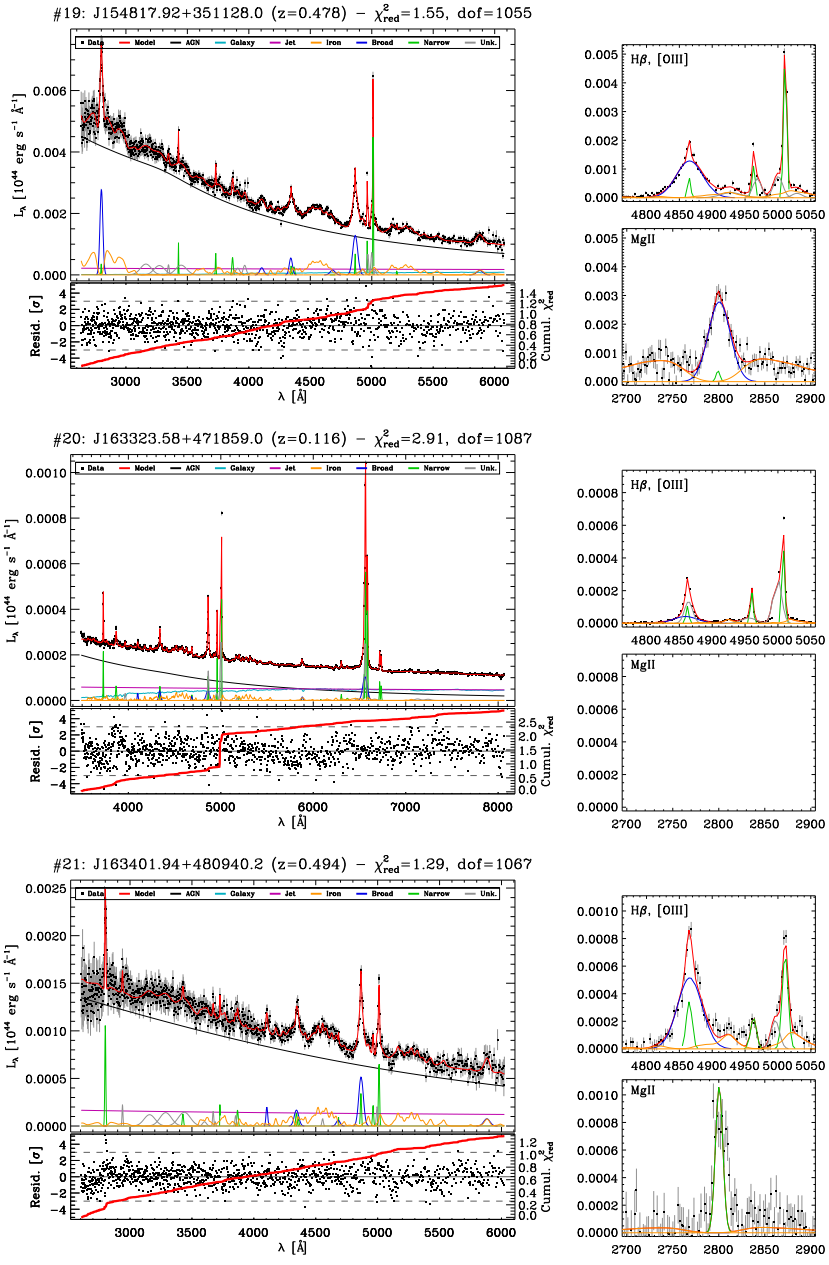

Fig. A.1: (continued)

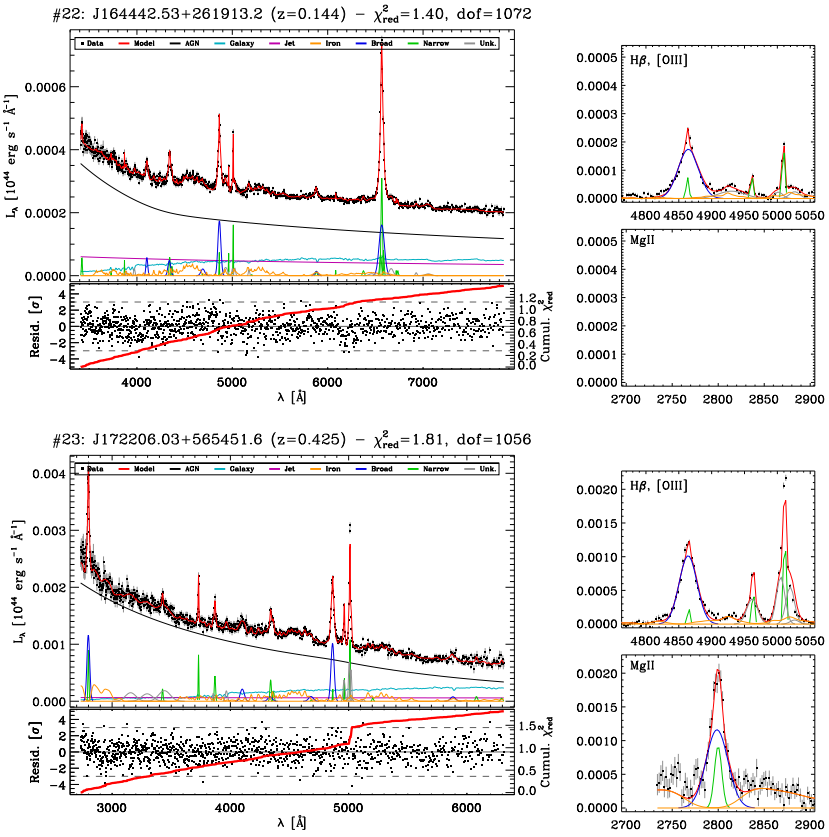

Fig. A.1: (continued)

A.2 Figures: black hole mass estimation

This appendix is a collection of the figures related to the black hole mass estimation procedures described in §6.3, adopting the same notation as in Fig. 6.4.

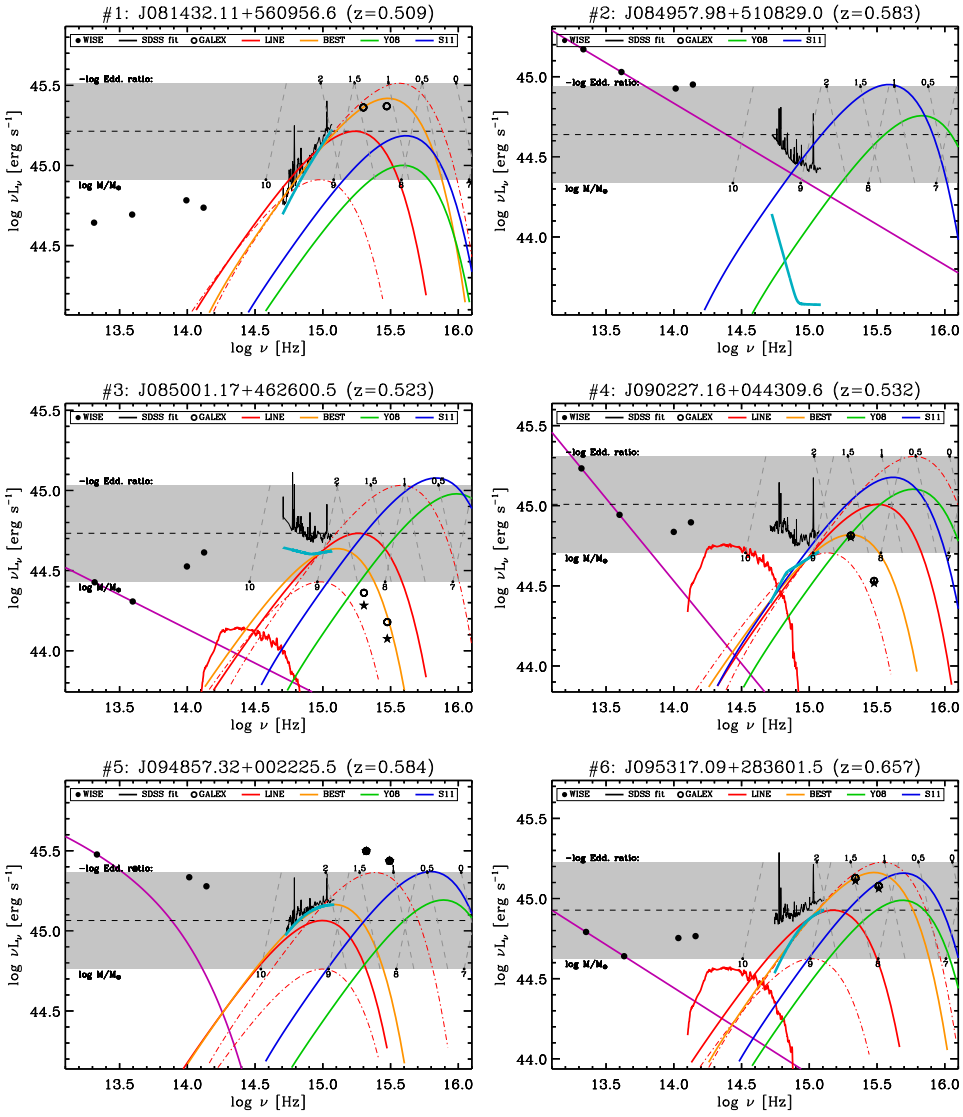

Fig. A.2: Results of the black hole mass estimation procedures (§6.3, App. A.2). Notation is the same as in Fig. 6.4.

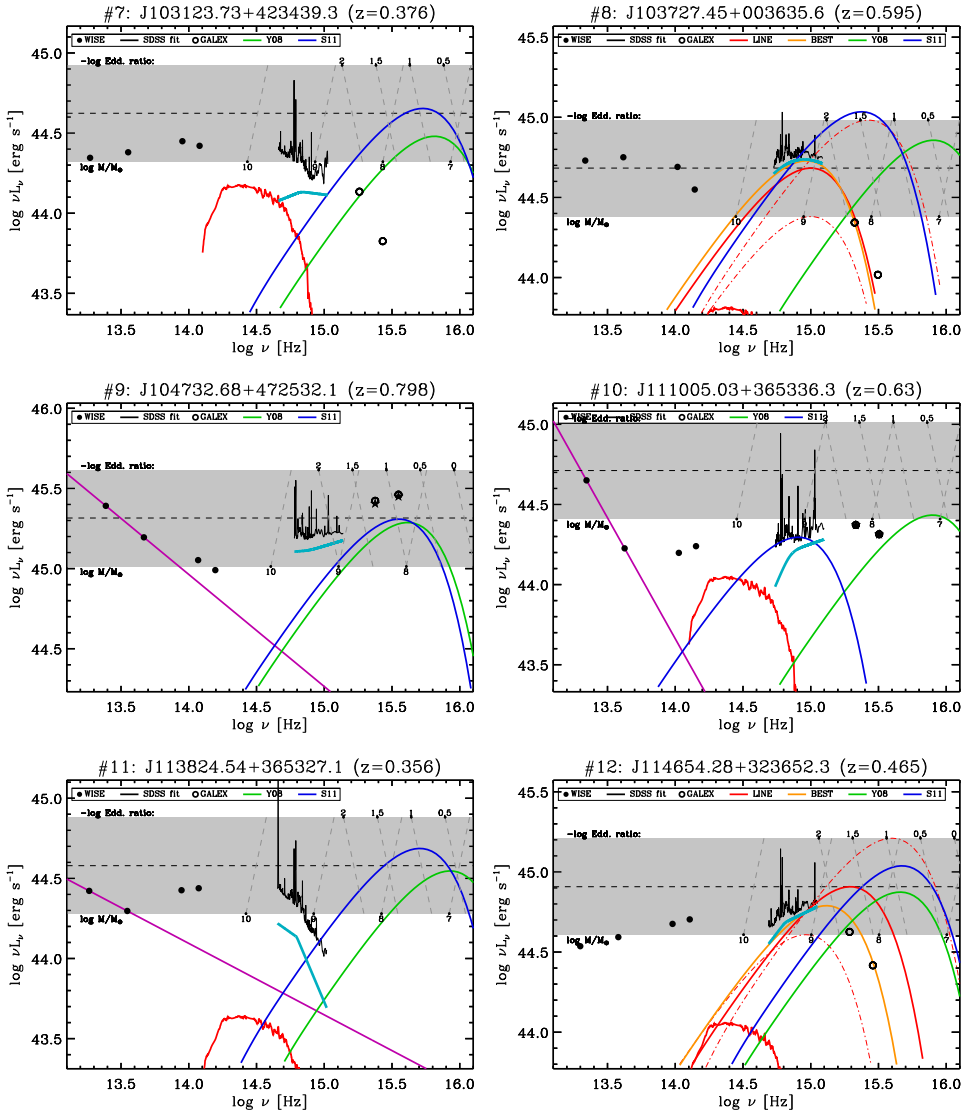

Fig. A.2: (continued)

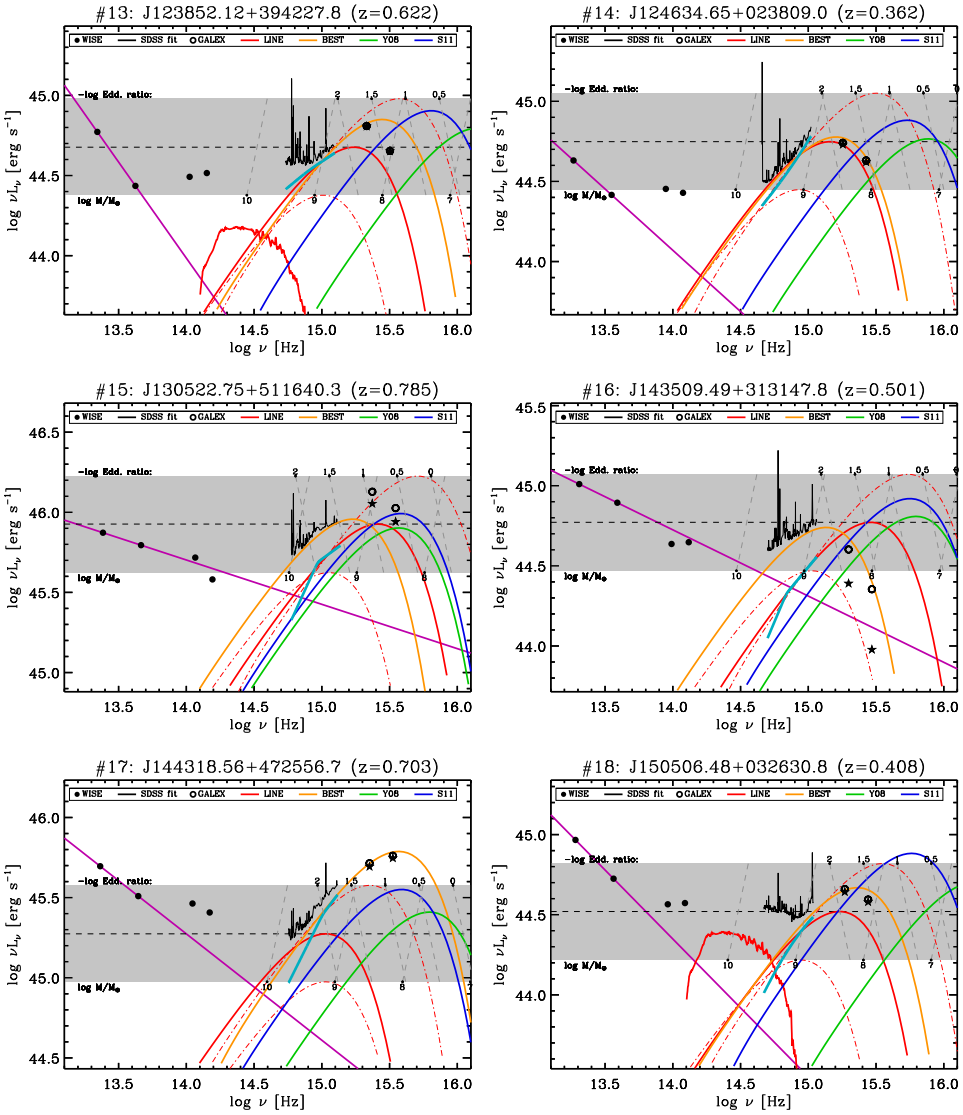

Fig. A.2: (continued)

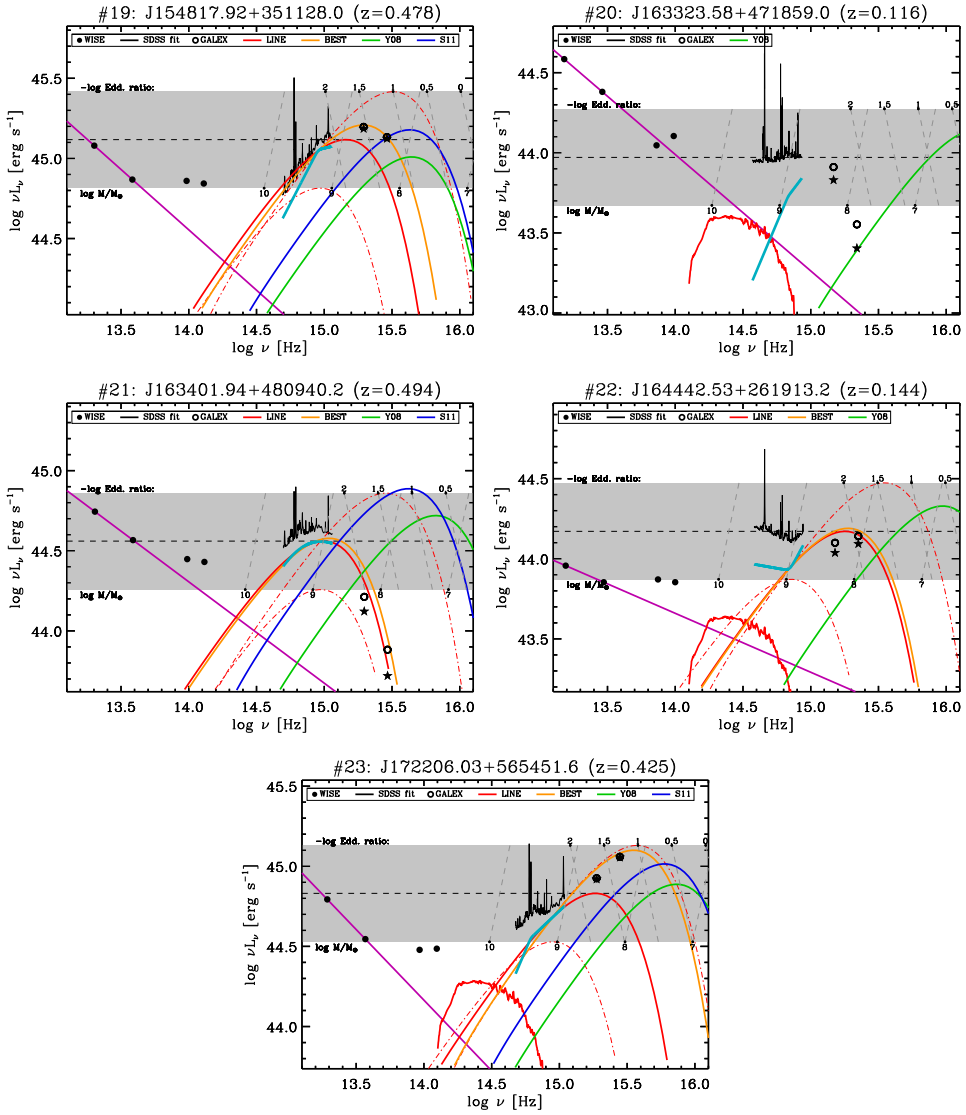

Fig. A.2: (continued)

Acknowledgements

... ovvero “Ringraziamenti”, poiché le persone che voglio ricordare in questa pagina sono italiane.

Sono in debito di gratitudine e riconoscenza verso i miei relatori, Monica Colpi e Gabriele Ghisellini, per la pazienza e amicizia dimostrata nei miei confronti, e sopratutto per la passione che hanno saputo trasmettermi. Le infinite discussioni su argomenti legati alla Scienza (e non solo!) resteranno uno dei più bei ricordi di questi tre anni.

Un grosso grazie va a Massimo Dotti e Roberto Decarli, per avermi svelato tanti misteri dell’astrofisica, ma sopratutto per avermi introdotto alla segreta arte della *Grande Scienza*, argomento da trattare solo dopo qualche bicchiere di buon rum.

Desidero poi ringraziare i miei *compagni di avventura* Ema e Carmen per le mille risate semiserie su argomenti della cui serietà dubito seriamente.

Un ringraziamento speciale lo dedico ai ragazzi delle scuole di astrofisica, in particolare Rossella, Ilaria, Anna, Elena, Mauro E Daniel. Cosa sarebbero state le scuole di astrofisica senza di voi????

Ringrazio poi i ragazzi dell’ Osservatorio di Merate per le simpaticissime pause pranzo.

Un abbraccio speciale lo devo alla mia colleguccia Tullia/7 per avermi sopportato in questi anni (tranquilla non hai ancora finito...).

Ringrazio poi i ragazzi del II piano: Ripa, Michela, Marco, Giorgio, Ale, Enzo, Franz e tutti gli altri. E fra questi meritano un bacione speciale le mie amiche Mery, Laura, Ross e Racq, per avermi dimostrato che anche da questa parte del tirreno è possibile passare interi pomeriggi a ridere.

Un carissimo abbraccio lo devo ai miei cari amici Fabio e Nik per le mitiche cene a base di cazzeggio e ricette speciali. Ad Anita per le volte che abbiamo visto le stelle e sognato mille avventure. E alla mia carissima amica Imane per le tante e illuminanti chiacchierate su ciò che accade sotto questo cielo.

Un pensiero affettuoso lo dedico alle mie care amiche sicule in terra lombarda Nadia, Marcella e Rossana con le quali ho condiviso tanti momenti speciali.

Infine desidero ringraziare tutti i miei amici *Tatucci* e le persone che mi sono state vicino in questi anni. I motivi li conosciamo bene ma è così difficile descriverli a parole. Forse dovrei provare a suonarli....

Fra le parole di questa tesi, oltre il mio lavoro, c'è il contributo inestimabile di coloro i quali mi sostengono oltre la loro stessa consapevolezza. Mamma, Papà, Nonna, Roberto, Giovanna, Totò e tutti gli altri... non ho parole per ringraziarvi.

Dedico questo lavoro di tesi ad una persona speciale: il piccolo Emanuele.

"Tra molto tempo - per esempio tra diecimila anni - non c'è dubbio che la scoperta delle equazioni di Maxwell sarà giudicato l'evento più significativo del XIX secolo. La guerra civile americana apparirà insignificante e provinciale se paragonata a questo importante evento scientifico della medesima decade."

R.P. Feynman

List of Figures

List of Tables

List of sources

Acronyms

$R_{\rm loud}$ Radio–loudness parameter

γ–NLS1 γ–ray active Narrow Line Seyfert 1

AD Shakura and Sunyaev (1973) Accretion Disk model

AGN Active Galactic Nucleus

BBB Big Blue Bump

BL Lac BL Lacertæ–like source

BLAGN Broad Line AGN

BLR Broad Line Region

BLRG Broad Line Radio galaxy

EW Equivalent width

FR–I Fanaroff Riley I radio galaxy

FR–II Fanaroff Riley II radio galaxy

FSRQ Flat Spectrum Radio Quasar

FWHM Full Width at Half Maximum

HST Hubble Space Telescope

ISCO Innermost Stable Circular Orbit

Jy 1 Jansky = 10^{-23} erg s^{-1} cm^{-2} Hz^{-1}

ld Light days (1 ld $\sim 2.6 \times 10^{15}$ cm $\sim 10^{-3}$ pc)

NED NASA/IPAC Extragalactic Database

NLR Narrow Line Region

NLRG Narrow Line Radio galaxy

NLS1 Narrow Line Seyfert 1

OVV Optically Violent Variable source

QSO Quasi–stellar object

Quasar Quasi–stellar radio source

RL Radio–loud source

RL–NLS1 Radio–Loud Narrow Line Seyfert 1

RM Reverberation Mapping

RQ Radio–quiet source

S11 Shen et al. (2011) catalog

SDSS Sloan Digital Sky Survey

SED Spectral Energy Distribution

SEV Single Epoch Virial method

SMBH Super Massive Black Hole

Sy1 Seyfert 1

Sy2 Seyfert 2

VLA Very Large Array

VLBI Very Long Baseline Interferometry

WFPC2 Wide Field and Planetary Camera 2

References

Abazajian K. N. et al. — **2009**, *ApJS* 182, 543, ADS pp. 112

Abdo A. A. et al. — **2009a**, *ApJ* 699, 976, ADS pp. 53, 121

Abdo A. A. et al. — **2009b**, *ApJ* 707, 727, ADS pp. 53, 54, 67, 113, 121

Abdo A. A. et al. — **2009c**, *ApJ* 707, L142, ADS pp. 53, 54, 67, 69, 112

Abdo A. A. et al. — **2010a**, *ApJ* 709, L152, ADS pp. 55

Abdo A. A. et al. — **2010b**, *ApJS* 188, 405, ADS pp. 59

Abdo A. A. et al. — **2011**, *(arXiv:1108.1435)* pp. 59

Aharonian F. et al. — **2007**, *ApJ* 664, L71, ADS pp. 2, 58

Alloin D. et al. — **1995**, *A&A* 293, 293, ADS pp. 3

Antón S., Browne I. W. A., and Marchã M. J. — **2008**, *A&A* 490, 583, ADS pp. 54

Antonucci R. — **1993**, *ARA&A* 31, 473, ADS pp. 12

Antonucci R. R. J. and Miller J. S. — **1985**, *ApJ* 297, 621, ADS pp. 14

Arnaud K. A. — **1996**, in G. H. Jacoby and J. Barnes (eds.), *Astronomical Data Analysis Software and Systems V*, Vol. 101 of *Astronomical Society of the Pacific Conference Series*, p. 17, ADS pp. 100

Arshakian T. G. — **2005**, *A&A* 436, 817, ADS pp. 86

Assef R. J., Frank S., Grier C. J., et al. — **2012**, *ApJ* 753, L2, ADS pp. 46

Barthel P. D. — **1989**, *ApJ* 336, 606, ADS pp. 16

Batcheldor D. — **2010**, *ApJ* 711, L108, ADS pp. 25

Becker R. H., White R. L., and Helfand D. J. — **1995**, *ApJ* 450, 559, ADS pp. 84

Bentz M. C., Peterson B. M., Netzer H., et al. — **2009**, *ApJ* 697, 160, ADS pp. 39, 67, 68, 74

Blandford R. D. and McKee C. F. — **1982**, *ApJ* 255, 419, ADS pp. 35

Blandford R. D. and Rees M. J. — **1978**, in A. M. Wolfe (ed.), *BL Lac Objects*, pp 328–341, ADS pp. 16

Blumenthal G. R. and Mathews W. G. — **1975**, *ApJ* 198, 517, ADS pp. 32, 63

Boller T., Brandt W. N., and Fink H. — **1996**, *A&A* 305, 53, ADS pp. 49, 67

Bonning E. W., Cheng L., Shields G. A., et al. — **2007**, *ApJ* 659, 211, ADS pp. 73

Bonning E. W., Shields G. A., Salviander S., et al. — **2005**, *ApJ* 626, 89, ADS pp. 26

Boroson T. A. — **2003**, *ApJ* 585, 647, ADS pp. 26

Boroson T. A. and Green R. F. — **1992**, *ApJS* 80, 109, ADS pp. 114

Burbidge E. M. and Strittmatter P. A. — **1972**, *ApJ* 174, L57+, ADS pp. 59

Calderone G., Foschini L., Ghisellini G., et al. — **2011**, *MNRAS* 413, 2365, ADS pp. 54, 69, 112

Calderone G., Ghisellini G., Colpi M., et al. — **2012a**, *MNRAS* 424, 3081, ADS pp. 59, 64, 107

Calderone G., Ghisellini G., Colpi M., et al. — **2012b**, *astro-ph/1212.1181m, MNRAS accepted*, ADS pp. 75, 93, 111

Calderone G., Sbarrato T., and Ghisellini G. — **2012c**, *MNRAS* 425, L41, ADS pp. 12, 84, 103

Capriotti E., Foltz C., and Byard P. — **1979**, *ApJ* 230, 681, ADS pp. 32, 63

Capriotti E., Foltz C., and Byard P. — **1980**, *ApJ* 241, 903, ADS pp. 32

Cardelli J. A., Clayton G. C., and Mathis J. S. — **1989**, *ApJ* 345, 245, ADS pp. 61, 112

Celotti A., Padovani P., and Ghisellini G. — **1997**, *MNRAS* 286, 415, ADS pp. 79

Chaudhary P., Brusa M., Hasinger G., et al. — **2010**, *A&A* 518, A58, ADS pp. 19

Chiaberge M. and Marconi A. — **2011**, *MNRAS* 416, 917, ADS pp. 41, 43, 44, 125

Cohen A. S., Lane W. M., Cotton W. D., et al. — **2007**, *AJ* 134, 1245, ADS pp. 59

Collin S., Boisson C., Mouchet M., et al. — **2002**, *A&A* 388, 771, ADS pp. 125

Croom S. M. — **2011**, *ApJ* 736, 161, ADS pp. 46, 47

Croom S. M., Richards G. T., Shanks T., et al. — **2009**, *MNRAS* 399, 1755, ADS pp. 19

Cunningham C. T. — **1975**, *ApJ* 202, 788, ADS pp. 100

Davis S. W. and Laor A. — **2011**, *ApJ* 728, 98, ADS pp. 74

Davis S. W., Woo J.-H., and Blaes O. M. — **2007**, *ApJ* 668, 682, ADS pp. 73

Decarli R., Dotti M., Fontana M., et al. — **2008**, *MNRAS* 386, L15, ADS pp. 37, 52, 74, 125

Decarli R., Dotti M., and Treves A. — **2011**, *MNRAS* 413, 39, ADS pp. 125

Donato D., Ghisellini G., Tagliaferri G., et al. — **2001**, *A&A* 375, 739, ADS pp. 11, 149

Done C., Davis S. W., Jin C., et al. — **2012**, *MNRAS* 420, 1848, ADS pp. 73, 126

Elitzur M. — **2012**, *ApJ* 747, L33, ADS pp. 90

Elitzur M. and Shlosman I. — **2006**, *ApJ* 648, L101, ADS pp. 83

Elvis M. — **2000**, *ApJ* 545, 63, ADS pp. 83

Elvis M. et al. — **1994**, *ApJS* 95, 1, ADS pp. 3, 8, 10, 71, 72

Fabian A. C. — **2012**, *ARA&A* 50, 455, ADS pp. 19

Fabian A. C. and Miniutti G. — **2005**, *astro-ph/0507409*, ADS pp. 19, 73

Fanaroff B. L. and Riley J. M. — **1974**, *MNRAS* 167, 31P, ADS pp. 6

Ferrarese L. and Ford H. — **2005**, *Space Sci. Rev.* 116, 523, ADS pp. 19, 20, 22, 73

Ferrarese L. and Merritt D. — **2000**, *ApJ* 539, L9, ADS pp. 23

Ferrarese L., Pogge R. W., Peterson B. M., et al. — **2001**, *ApJ* 555, L79, ADS pp. 37

Fiore F., Laor A., Elvis M., et al. — **1998**, *ApJ* 503, 607, ADS pp. 49

Foschini L. — **2011**, in Proc. of "Narrow-Line Seyfert 1 Galaxies and their Place in the Universe" eds. L. Foschini, M. Colpi, L. Gallo, D. Grupe, S. Komossa, K. Leighly, & S. Mathur, PoS (NLS1) 024, ADS pp. 112

Foschini L. et al. — **2008**, *ATel* 1784, ADS pp. 58

Foschini L. et al. — **2009a**, in Proceedings of "Accretion and ejection in AGN: a global view". L. Maraschi, G. Ghisellini, R. Della Ceca & F. Tavecchio eds, ASP Conference Series 427, San Francisco, in press (arXiv:0908.3313) pp. 53, 69

Foschini L. et al. — **2011**, *MNRAS* 413, 1671, ADS pp. 54, 66, 121

Foschini L., Maraschi L., Tavecchio F., et al. — **2009b**, *Advances in Space Research* 43, 889, ADS pp. 54

Foschini L., Tagliaferri G., Ghisellini G., et al. — **2010**, *MNRAS* 408, 448, ADS pp. 58

Francis P. J., Hewett P. C., Foltz C. B., et al. — **1991**, *ApJ* 373, 465, ADS pp. 30, 79, 130

Frank J., King A., and Raine D. J. — **2002**, *Accretion Power in Astrophysics: Third Edition*, ADS pp. 18, 94

Gaffney N. I., Lester D. F., and Telesco C. M. — **1993**, *ApJ* 407, L57, ADS pp. 55

Gebhardt K., Bender R., Bower G., et al. — **2000**, *ApJ* 539, L13, ADS pp. 23, 24

Genzel R., Eisenhauer F., and Gillessen S. — **2010**, *Reviews of Modern Physics* 82, 3121, ADS pp. 18

Ghisellini G. and Tavecchio F. — **2009**, *MNRAS* 397, 985, ADS pp. 54, 64

Ghisellini G., Tavecchio F., Foschini L., et al. — **2010**, *MNRAS* 402, 497, ADS pp. 10, 65, 72, 120

Gillessen S., Eisenhauer F., Trippe S., et al. — **2009**, *ApJ* 692, 1075, ADS pp. 18, 21

Gilli R., Comastri A., and Hasinger G. — **2007**, *A&A* 463, 79, ADS pp. 15

Goodrich R. W. — **1989**, *ApJ* 342, 224, ADS pp. 49, 50, 69

Graham A. W., Onken C. A., Athanassoula E., et al. — **2011**, *MNRAS* 412, 2211, ADS pp. 24, 25, 38, 41, 67, 125

Greene J. E. and Ho L. C. — **2005**, *ApJ* 627, 721, ADS pp. 26

Grupe D., Beuermann K., Thomas H.-C., et al. — **1998**, *A&A* 330, 25, ADS pp. 49

Grupe D., Komossa S., Leighly K. M., et al. — **2010**, *ApJS* 187, 64, ADS pp. 120, 124

Grupe D. and Mathur S. — **2004**, *ApJ* 606, L41, ADS pp. 51, 69

Gu M., Cao X., and Jiang D. R. — **2001**, *MNRAS* 327, 1111, ADS pp. 59

Gu M. and Chen Y. — **2010**, *AJ* 139, 2612, ADS pp. 54

Gültekin K., Richstone D. O., Gebhardt K., et al. — **2009**, *ApJ* 698, 198, ADS pp. 24, 37

Gültekin K., Tremaine S., Loeb A., et al. — **2011**, *ApJ* 738, 17, ADS pp. 25

Hopkins P. F., Richards G. T., and Hernquist L. — **2007**, *ApJ* 654, 731, ADS pp. 19

Hoyle F. and Fowler W. A. — **1963**, *MNRAS* 125, 169, ADS pp. 17

Hu J. — **2008**, *MNRAS* 386, 2242, ADS pp. 22, 24

Hubeny I., Blaes O., Krolik J. H., et al. — **2001**, *ApJ* 559, 680, ADS pp. 74, 126

Jackson N. and Browne I. W. A. — **1991**, *MNRAS* 250, 414, ADS pp. 59, 60, 61

Jaffe W., Ford H. C., Ferrarese L., et al. — **1993**, *Nature* 364, 213, ADS pp. 16

Jiang L., Fan X., Ivezić Ž., et al. — **2007**, *ApJ* 656, 680, ADS pp. 8

Juarez Y., Maiolino R., Mujica R., et al. — **2009**, *A&A* 494, L25, ADS pp. 19, 30

Kaspi S., Maoz D., Netzer H., et al. — **2005**, *ApJ* 629, 61, ADS pp. 38, 39

Kaspi S., Smith P. S., Netzer H., et al. — **2000**, *ApJ* 533, 631, ADS pp. 38

Keel W. C., White III R. E., Owen F. N., et al. — **2006**, *AJ* 132, 2233, ADS pp. 54

Kellermann K., Sramek R., Schmidt M., et al. — **1989**, *AJ* 98, 1195 pp. 8, 9, 81, 112, 149

Kellermann K. I. et al. — **2004**, *ApJ* 609, 539, ADS pp. 59

Khachikian E. Y. and Weedman D. W. — **1974**, *ApJ* 192, 581, ADS pp. 4

Kishimoto M., Antonucci R., Blaes O., et al. — **2008**, *Nature* 454, 492, ADS pp. 77

Komossa S. — **2008**, in *Revista Mexicana de Astronomia y Astrofisica Conference Series*, Vol. 32 of *Revista Mexicana de Astronomia y Astrofisica Conference Series*, pp 86–92, ADS pp. 51

Komossa S., Voges W., Xu D., et al. — **2006**, *AJ* 132, 531, ADS pp. 51, 53, 125

Komossa S. and Xu D. — **2007**, *ApJ* 667, L33, ADS pp. 52

Koratkar A. and Blaes O. — **1999**, *PASP* 111, 1, ADS pp. 73

Kormendy J. and Richstone D. — **1995**, *ARA&A* 33, 581, ADS pp. 18, 19, 20, 23

Kovalev Y. Y. et al. — **2005**, *AJ* 130, 2473, ADS pp. 59

Krolik J. H. — **2001**, *ApJ* 551, 72, ADS pp. 41

Krolik J. H. and Begelman M. C. — **1988**, *ApJ* 329, 702, ADS pp. 12

Kuo C. Y., Braatz J. A., Condon J. J., et al. — **2011**, *ApJ* 727, 20, ADS pp. 22

Landt H., Elvis M., Ward M. J., et al. — **2011**, *MNRAS* 414, 218, ADS pp. 84

Laor A. — **2000**, *New A Rev.* 44, 503, ADS pp. 50

Laor A. and Davis S. — **2011a**, *astro-ph:1110.0653*, ADS pp. 73, 74

Laor A. and Davis S. W. — **2011b**, *MNRAS* 417, 681, ADS pp. 74

Lawrence A. — **2012**, *MNRAS* 423, 451, ADS pp. 126

Li L.-X., Zimmerman E. R., Narayan R., et al. — **2005**, *ApJS* 157, 335, ADS pp. 100, 101, 150

Lister M. L. and Smith P. S. — **2000**, *ApJ* 541, 66, ADS pp. 59

Liu F. K. and Zhang Y. H. — **2002**, *A&A* 381, 757, ADS pp. 59

Liu Y., Jiang D. R., and Gu M. F. — **2006**, *ApJ* 637, 669, ADS pp. 59

Longair M. S. — **2010**, *High Energy Astrophysics*, ADS pp. 94

Lynden-Bell D. — **1969**, *Nature* 223, 690, ADS pp. 18

Magorrian J., Tremaine S., Richstone D., et al. — **1998**, *AJ* 115, 2285, ADS pp. 23

Malkan M. A. — **1983**, *ApJ* 268, 582, ADS pp. 72

Malkan M. A. and Sargent W. L. W. — **1982**, *ApJ* 254, 22, ADS pp. 72

Mannucci F., Basile F., Poggianti B. M., et al. — **2001**, *MNRAS* 326, 745, ADS pp. 76, 91, 92, 113, 120

Marconi A., Axon D. J., Maiolino R., et al. — **2008**, *ApJ* 678, 693, ADS pp. 41, 53, 74, 125

Marscher A. P. — **2009**, *astro-ph:0909.2576*, ADS pp. 54

Martin D. C. et al. — **2005**, *ApJ* 619, L1, ADS pp. 111

Mathur S. and Grupe D. — **2005**, *ApJ* 633, 688, ADS pp. 51, 52

Mathur S., Kuraszkiewicz J., and Czerny B. — **2001**, *New A* 6, 321, ADS pp. 52

Mattox J. R. et al. — **1996**, *ApJ* 461, 396, ADS pp. 55

McConnell N. J., Ma C.-P., Gebhardt K., et al. — **2011**, *Nature* 480, 215, ADS pp. 25

McConnell N. J., Ma C.-P., Murphy J. D., et al. — **2012**, *ApJ* 756, 179, ADS pp. 22

McLure R. J. and Dunlop J. S. — **2004**, *MNRAS* 352, 1390, ADS pp. 40

Merloni A. and Heinz S. — **2012**, *astro-ph:1204.4265*, ADS pp. 19

Merritt D. and Ferrarese L. — **2001**, *MNRAS* 320, L30, ADS pp. 18

Miller J. S., Goodrich R. W., and Mathews W. G. — **1991**, *ApJ* 378, 47, ADS pp. 14

Miyoshi M., Moran J., Herrnstein J., et al. — **1995**, *Nature* 373, 127, ADS pp. 22

Morgan C. W., Kochanek C. S., Morgan N. D., et al. — **2010**, *ApJ* 712, 1129, ADS pp. 126

Mortlock D. J., Warren S. J., Venemans B. P., et al. — **2011**, *Nature* 474, 616, ADS pp. 1, 19

Murphy D. W., Browne I. W. A., and Perley R. A. — **1993**, *MNRAS* 264, 298, ADS pp. 59

Nandra K. and Pounds K. A. — **1994**, *MNRAS* 268, 405, ADS pp. 73

Nelson C. H., Green R. F., Bower G., et al. — **2004**, *ApJ* 615, 652, ADS pp. 37

Nelson C. H. and Whittle M. — **1995**, *ApJS* 99, 67, ADS pp. 26

Nelson C. H. and Whittle M. — **1996**, *ApJ* 465, 96, ADS pp. 26

Nenkova M., Sirocky M. M., Nikutta R., et al. — **2008**, *ApJ* 685, 160, ADS pp. 83

Netzer H. — **1990**, in R. D. Blandford, H. Netzer, L. Woltjer, T. J.-L. Courvoisier, and M. Mayor (eds.), *Active Galactic Nuclei*, pp 57–160, ADS pp. 37

Netzer H. and Trakhtenbrot B. — **2007**, *ApJ* 654, 754, ADS pp. 69

Neugebauer G., Oke J. B., Becklin E. E., et al. — **1979**, *ApJ* 230, 79, ADS pp. 73

Novikov I. D. and Thorne K. S. — **1973**, in C. Dewitt and B. S. Dewitt (eds.), *Black Holes (Les Astres Occlus), Gordon and Breach, New York*, pp 343–450, ADS pp. 100

O'Donnell J. E. — **1994**, *ApJ* 422, 158, ADS pp. 112

Onken C. A., Ferrarese L., Merritt D., et al. — **2004**, *ApJ* 615, 645, ADS pp. 37, 74

Onken C. A., Valluri M., Peterson B. M., et al. — **2007**, *ApJ* 670, 105, ADS pp. 22

Osterbrock D. E. and Ferland G. J. — **2006**, *Astrophysics of gaseous nebulae and active galactic nuclei*, ADS pp. 3, 30

Osterbrock D. E. and Phillips M. M. — **1977**, *PASP* 89, 251, ADS pp. 32

Osterbrock D. E. and Pogge R. W. — **1985**, *ApJ* 297, 166, ADS pp. 49, 69

Owen F. N. and White R. A. — **1991**, *MNRAS* 249, 164, ADS pp. 7

Padovani P. and Urry C. M. — **1992**, *ApJ* 387, 449, ADS pp. 16

Page D. N. and Thorne K. S. — **1974**, *ApJ* 191, 499, ADS pp. 100

Park D., Woo J.-H., Treu T., et al. — **2012**, *ApJ* 747, 30, ADS pp. 38, 125

Pearson T. J., Unwin S. C., Cohen M. H., et al. — **1981**, *Nature* 290, 365, ADS pp. 10

Pei Y. C. — **1992**, *ApJ* 395, 130, ADS pp. 92

Peterson B. M. — **1987**, *ApJ* 312, 79, ADS pp. 32, 33, 69

Peterson B. M. — **1993**, *PASP* 105, 247, ADS pp. 3, 32, 35, 74

Peterson B. M. — **1997**, *An Introduction to Active Galactic Nuclei*, ADS pp. 30, 31

Peterson B. M. — **2010**, in B. M. Peterson, R. S. Somerville, and T. Storchi-Bergmann (eds.), *IAU Symposium*, Vol. 267 of *IAU Symposium*, pp 151–160, ADS pp. 39

Peterson B. M. — **2011**, *astro-ph:1109.4181*, ADS pp. 40, 42, 74

Peterson B. M. et al. — **2004**, *ApJ* 613, 682, ADS pp. 36, 37, 41, 42, 53, 74, 125

Peterson B. M., Korista K. T., and Cota S. A. — **1987**, *ApJ* 312, L1, ADS pp. 32

Peterson B. M. and Wandel A. — **2000**, *ApJ* 540, L13, ADS pp. 35, 36, 40, 41

Pica A. J., Smith A. G., Webb J. R., et al. — **1988**, *AJ* 96, 1215, ADS pp. 59

Pogge R. W. — **1989**, *ApJ* 345, 730, ADS pp. 12

Pogge R. W. — **2000**, *New Astronomy Review* 44, 381, ADS pp. 5, 51

Popović L. Č., Mediavilla E., Bon E., et al. — **2004**, *A&A* 423, 909, ADS pp. 33

Pounds K. A., Warwick R. S., Culhane J. L., et al. — **1986**, *MNRAS* 218, 685, ADS pp. 49, 73

Prieto A. — **2012**, *Journal of Physics Conference Series* 372(1), 012012, ADS pp. 15

Pringle J. E. — **1981**, *ARA&A* 19, 137, ADS pp. 18, 94

Puchnarewicz E. M., Mason K. O., Cordova F. A., et al. — **1992**, *MNRAS* 256, 589, ADS pp. 49

Raimundo S. I., Fabian A. C., Vasudevan R. V., et al. — **2012**, *MNRAS* 419, 2529, ADS pp. 74

Rees M. J. — **1984**, *ARA&A* 22, 471, ADS pp. 17, 18

Richards G. T. et al. — **2006**, *ApJS* 166, 470, ADS pp. 8, 71, 75, 76, 78, 130, 150

Risaliti G., Elvis M., and Nicastro F. — **2002**, *ApJ* 571, 234, ADS pp. 83

Romano P., Zwitter T., Calvani M., et al. — **1996**, *MNRAS* 279, 165, ADS pp. 32, 33

Salpeter E. E. — **1964**, *ApJ* 140, 796, ADS pp. 17

Sanders D. B., Phinney E. S., Neugebauer G., et al. — **1989**, *ApJ* 347, 29, ADS pp. 8, 14, 71, 73

Sbarrato T., Ghisellini G., Nardini M., et al. — **2012**, *MNRAS* 426, L91, ADS pp. 104

Schlegel D. J., Finkbeiner D. P., and Davis M. — **1998**, *ApJ* 500, 525, ADS pp. 92, 112

Schmidt M. and Green R. F. — **1983**, *ApJ* 269, 352, ADS pp. 8

Schneider D. P. et al. — **2010**, *AJ* 139, 2360, ADS pp. 43

Shakura N. I. and Sunyaev R. A. — **1973**, *A&A* 24, 337, ADS pp. 18, 27, 65, 72, 73, 74, 75, 91, 92, 93, 94, 101, 102, 103, 126, 130, 150, 157

Shen Y. et al. — **2011**, *ApJS* 194, 45, ADS pp. 40, 43, 44, 63, 67, 68, 78, 84, 114, 129, 149, 153, 158

Shields G. A. — **1978**, *Nature* 272, 706, ADS pp. 72

Simpson C. — **2005**, *MNRAS* 360, 565, ADS pp. 86

Soltan A. — **1982**, *MNRAS* 200, 115, ADS pp. 18

Steffen A. T., Strateva I., Brandt W. N., et al. — **2006**, *AJ* 131, 2826, ADS pp. 19

Stirpe G. M. — **1990**, *A&AS* 85, 1049, ADS pp. 32

Stirpe G. M., de Bruyn A. G., and van Groningen E. — **1988**, *A&A* 200, 9, ADS pp. 32

Su M., Slatyer T. R., and Finkbeiner D. P. — **2010**, *ApJ* 724, 1044, ADS pp. 18

Sulentic J. W., Zwitter T., Marziani P., et al. — **2000**, *ApJ* 536, L5, ADS pp. 69

Sun W.-H. and Malkan M. A. — **1989**, *ApJ* 346, 68, ADS pp. 72

Tadhunter C. and Tsvetanov Z. — **1989**, *Nature* 341, 422, ADS pp. 12

Tavecchio F., Ghisellini G., Bonnoli G., et al. — **2010**, *MNRAS* 405, L94, ADS pp. 58

Telfer R. C., Zheng W., Kriss G. A., et al. — **2002**, *ApJ* 565, 773, ADS pp. 19, 76, 77

Thorne K. S. — **1974**, *ApJ* 191, 507, ADS pp. 17, 100, 102, 106

Torniainen I., Tornikoski M., Teräsranta H., et al. — **2005**, *A&A* 435, 839, ADS pp. 59

Tremaine S. et al. — **2002**, *ApJ* 574, 740, ADS pp. 23, 24, 67, 68

Urry C. M. and Padovani P. — **1995**, *PASP* 107, 803, ADS pp. 12

Urry C. M., Padovani P., and Stickel M. — **1991**, *ApJ* 382, 501, ADS pp. 16

van den Bosch R. C. E., Gebhardt K., Gültekin K., et al. — **2012**, *Nature* 491, 729, ADS pp. 25

Vanden Berk D. E. et al. — **2001**, *AJ* 122, 549, ADS pp. 4, 30, 71, 73, 76, 77, 79, 91, 92

Véron-Cetty M.-P., Joly M., and Véron P. — **2004**, *A&A* 417, 515, ADS pp. 113, 114

Véron-Cetty M.-P., Véron P., and Gonçalves A. C. — **2001**, *A&A* 372, 730, ADS pp. 32, 50, 69

Vestergaard M., Denney K., Fan X., et al. — **2011**, in *Narrow-Line Seyfert 1 Galaxies and their Place in the Universe*, ADS pp. 42

Vestergaard M. and Osmer P. S. — **2009**, *ApJ* 699, 800, ADS pp. 40, 67, 68

Vestergaard M. and Peterson B. M. — **2006**, *ApJ* 641, 689, ADS pp. 40, 43, 44, 67, 68, 74

Vestergaard M. and Wilkes B. J. — **2001**, *ApJS* 134, 1, ADS pp. 113

Volonteri M. — **2010**, *A&A Rev.* 18, 279, ADS pp. 19

Walter R. and Fink H. H. — **1993**, *A&A* 274, 105, ADS pp. 73

Wandel A. and Boller T. — **1998**, *A&A* 331, 884, ADS pp. 50

Williams R. J., Pogge R. W., and Mathur S. — **2002**, *AJ* 124, 3042, ADS pp. 49, 52

Wills B. J., Netzer H., and Wills D. — **1985**, *ApJ* 288, 94, ADS pp. 71, 76

Wills B. J., Wills D., Breger M., et al. — **1992**, *ApJ* 398, 454, ADS pp. 59

Woo J.-H., Treu T., Barth A. J., et al. — **2010**, *ApJ* 716, 269, ADS pp. 37

Woo J.-H. and Urry C. M. — **2002**, *ApJ* 579, 530, ADS pp. 59

Wright E. L. et al. — **2010**, *AJ* 140, 1868, ADS pp. 83, 111, 113

York D. G. et al. — **2000**, *AJ* 120, 1579, ADS pp. 83, 112

Young M., Elvis M., and Risaliti G. — **2009**, *ApJS* 183, 17, ADS pp. 19

Yuan W., Zhou H. Y., Komossa S., et al. — **2008**, *ApJ* 685, 801, ADS pp. 51, 53, 111, 112, 116, 120, 124, 131

Zhang S. N., Cui W., and Chen W. — **1997**, *ApJ* 482, L155, ADS pp. 73, 100

Zheng W. et al. — **1995**, *ApJ* 444, 632, ADS pp. 72

Zhou H. et al. — **2007**, *ApJ* 658, L13, ADS pp. 53, 54

Zhou H., Wang T., Dong X., et al. — **2003**, *ApJ* 584, 147, ADS pp. 53

Zhou H., Wang T., Yuan W., et al. — **2006**, *ApJS* 166, 128, ADS pp. 49, 50, 51, 54, 69, 80, 81, 111

Zhu L., Zhang S. N., and Tang S. — **2009**, *ApJ* 700, 1173, ADS pp. 33